Table of contents

Abstract

The knowledge of the microstructural properties of cement-based materials plays a fundamental role in predicting their macroscopic behaviour in terms of performance and durability. However, due to the intrinsic microstructural and chemical complexity of such materials, a multi-disciplinary approach is often required. Most classical experimental techniques such as XRD, XRF or mercury porosimetry (MIP) only provide overall information about selected properties (phase and chemical composition, porosity, etc.) but give no indications about their real spatial distribution within the investigated sample. Over the past decades, modern experimental methods for microstructural analysis such as SEM imaging have lead to great advances in our understanding of the complex mechanisms occurring during cement hydration. However, the lack of access to three-dimensional (3D) information represents the main limitation of SEM and other 2D imaging techniques. Furthermore, as sample preparation is often quite invasive, the microstructure of cement may result completely altered. For such reasons, the development of non-destructive techniques for the 3D microstructural investigation of materials has become necessary. Nowadays X-ray computed micro-tomography (X-μCT) provides a totally non-invasive tool to investigate in a three-dimensional way the inner structure of materials, with a spatial resolution reaching the sub-μm level when the most advanced systems are employed. X-μCT allows to reconstruct 3D maps of the variations of the X-ray linear attenuation coefficient (μ) within a sample without perturbing its structure.

The aim of this research project is to assess the potential of X-μCT for the microstructural study of several features of interest in cementitious materials. The evolution of the microstructure during setting and hardening, the effects of water-cement ratio (w/c), the role of superplasticizers and the pore space properties are among the major topics that have been investigated. The results obtained from X-μCT at the microscopic scale can then be correlated with the corresponding macroscopic properties observed in real applications.

In order to compare the capabilities of the two most common types of X-μCT setups, experiments were carried out using both conventional laboratory instruments and synchrotron-based systems. A synchrotron study of cement evolution during the early hydration stages was successfully performed, focusing the attention on the effect of superplasticizers (chapter 4). The high spatial resolution achievable allowed to follow the evolution of porosity and anhydrous cement fraction as a function of hydration time. In

chapter 5, conventional laboratory X-μCT was applied to the study of cement paste samples prepared at different w/c ratios in order to get insights on the microstructural features that determine the variations of strengths in macroscopic samples with varying water contents (chapter 5).

In addition, the capabilities of a novel experimental technique (diffraction tomography, XRD-CT) were tested for the first time on cementitious samples (chapter 6). By combining the principles of X-ray micro-diffraction with those of tomographic reconstruction, XRD-CT allows to map the distribution of selected crystalline or amorphous phases within a sample in a totally non invasive manner. In this way, one of the main limitations of X-μCT, related to the poor sensitivity to small absorption variations between different phases can be overcome. Despite the fact that data analysis is not straightforward and requires further developments, the preliminary results presented in this thesis show that crystalline and amorphous phases growing during cement hydration such as ettringite and C-S-H can be successfully mapped without perturbing the system.

In the last part of the thesis (chapter 7), a practical application example of X-μCT is reported. The tomographic technique was employed to characterize the pore space properties and the microstructure of cementitious granular materials produced from the solidification and stabilization process (S/S) of soils contaminated by heavy metals. The results of X-μCT analyses were then combined with those obtained using other established experimental methods (e.g. MIP, physico-mechanical and leaching tests) in order to evaluate the performances and environmental compatibility of an innovative method of contaminated grounds remediation.

Riassunto

La conoscenza delle proprietà microstrutturali dei materiali cementizi gioca un ruolo fondamentale nel predire il loro comportamento macroscopico in termini di prestazioni e durabilità. Tuttavia, a causa dell'intrinseca complessità microstrutturale e chimica di tali materiali, un approccio multi disciplinare è spesso richiesto. La maggior parte delle tecniche sperimentali classiche come XRD, XRF o la porosimetria a mercurio (MIP) forniscono solamente informazioni complessive riguardo determinate proprietà (composizione mineralogica e chimica, porosità, etc.) ma non danno alcuna indicazione sulla loro reale distribuzione spaziale all'interno del campione studiato. Nel corso degli ultimi decenni, i moderni metodi sperimentali per l'analisi microstrutturale come la microscopia elettronica a scansione (SEM) hanno portato ad importanti avanzamenti delle nostre conoscenze sui complessi meccanismi che avvengono nel corso dell'idratazione del cemento. Tuttavia, l'impossibilità di accedere ad informazioni tridimensionali (3D) rappresenta la principale limitazione della tecnica SEM e degli altri metodi di imaging 2D. Inoltre, poiché la preparazione del campione è spesso piuttosto invasiva, la microstruttura del cemento può risultare completamente alterata. Per tali ragioni, si è reso necessario lo sviluppo di tecniche non distruttive per lo studio microstrutturale in 3D dei materiali. Oggigiorno, la micro-tomografia computerizzata a raggi X (X-μCT) fornisce uno strumento totalmente non invasivo per studiare in modo tridimensionale la struttura interna dei materiali, con una risoluzione spaziale che può raggiungere il livello sub-micrometrico quando vengono utilizzati i sistemi più avanzati. La X-μCT consente di ricostruire mappe in 3D delle variazioni del coefficiente di attenuazione lineare dei raggi X (μ) all'interno di un campione senza perturbarne la struttura.

Lo scopo di questo progetto di ricerca è quello di verificare le potenzialità della X-μCT per lo studio microstrutturale di diversi aspetti di interesse nei materiali cementizi. Tra le principali tematiche che sono state affrontate vi sono l'evoluzione della microstruttura durante la presa e l'indurimento, gli effetti del rapporto acqua-cemento, il ruolo degli additivi superfluidificanti e le proprietà dello spazio poroso. I risultati ottenuti dalla X-μCT alla scala microscopica possono essere correlati con le corrispondenti proprietà microscopiche osservate nelle applicazioni reali.

Al fine di confrontare le potenzialità delle due principali tipologie di strumenti per X-μCT, sono stati effettuati esperimenti utilizzando sia sistemi convenzionali da laboratorio sia

sistemi da sincrotrone. Uno studio al sincrotrone sull'evoluzione del cemento nel corso degli stadi iniziali dell'idratazione è stato portato a termine con successo, ponendo l'attenzione sull'effetto dei superfluidificanti (cap. 4). L'elevata risoluzione spaziale ottenibile ha consentito di seguire l'evoluzione della porosità e della frazione di cemento anidro in funzione del tempo di idratazione. Nel capitolo 5, la X-μCT convenzionale da laboratorio è stata applicata allo studio di campioni di paste di cemento preparati a diverso rapporto acqua-cemento al fine di ottenere indicazioni sui parametri microstrutturali che determinano le variazioni delle resistenze meccaniche in campioni macroscopici al variare del contenuto d'acqua.

Inoltre, le potenzialità di una tecnica sperimentale recentemente sviluppata (diffraction tomography, XRD-CT) sono state testate per la prima volta su campioni cementizi (cap. 6). La tecnica della XRD-CT, combinando i principi della micro-diffrazione a raggi X con quelli della ricostruzione tomografica, consente di mappare la distribuzione di determinate fasi cristalline o amorfe all'interno di un campione in una maniera del tutto non invasiva. In questo modo, una delle principali limitazioni della X-μCT legata alla scarsa sensibilità nei confronti di ridotte variazioni di assorbimento tra diverse fasi può essere superata. Nonostante l'analisi dei dati non sia semplice e richieda ulteriori sviluppi, i risultati preliminari presentati in questa tesi mostrano che alcune fasi, sia cristalline sia amorfe, che si sviluppano nel corso dell'idratazione del cemento (come ad esempio l'ettringite o il C-S-H), possono essere mappate con successo senza perturbare il sistema.

Nell'ultima parte del lavoro è riportato un esempio pratico di applicazione della X-μCT. La tecnica tomografica è stata utilizzata per caratterizzare la porosità e la microstruttura di materiali cementizi granulari prodotti dal processo di solidificazione e stabilizzazione (S/S) di suoli contaminati da metalli pesanti. I risultati delle analisi di X-μCT sono stati poi combinati con quelli ottenuti usando altri metodi sperimentali classici (ad esempio MIP, test fisico-meccanici e di cessione) al fine di valutare le prestazioni e la compatibilità ambientale di un metodo innovativo di bonifica dei terreni inquinati.

1 - Portland cement: basics concepts

1.1 Portland cement manufacture

Portland cement (often referred to as OPC, Ordinary Portland Cement) is an inorganic hydraulic binder produced by finely grinding Portland cement clinker plus a limited amount of calcium sulphates and other minor constituents (Taylor, 1990, Hewlett, 2007). It is by far the most widely used binding agent in construction industry for the production of concretes, mortars and grouts. When Portland cement is mixed with water, a paste is formed which sets and hardens as a consequence of hydration reactions. The growth of new hydrated phases leads to the development of mechanical strengths in the paste, which are preserved even if it is stored under water. According to the EN 197-1 norm, Portland cement clinker (i.e. the main constituent of Portland cement) shall consist of at least two-thirds by mass of Ca-silicates ($3CaO \cdot SiO_2$ and $2CaO \cdot SiO_2$), the remainder being constituted of Al- and Fe-containing phases and other compounds. The ratio of CaO to SiO_2 shall not be less than 2 and the MgO content shall not exceed 5% by mass.

The raw mix for the production of Portland cement clinker is generally obtained by blending a calcareous material, typically a limestone, with a smaller amount of an argillaceous one, as for example clay or shale. In order to correct the bulk composition, it may be necessary to include minor proportions of one or more corrective constituents such as iron ore, bauxite or siliceous sand. However, some argillaceous limestones and marls may show compositions very close to the one required and can be directly employed.

In a first stage, the raw materials undergo a series of dying, crushing, milling and blending stages, which yield an intimately mixed powder whose grain size is typically about 160 μm. Then the raw meal passes through a pre-heater (with temperatures up to 800 °C) and typically also through a pre-calciner before entering a rotary kiln, typically 50-100 m long, sloping at 3-4% from the horizontal and rotating at a few revolutions per minute. The raw material enters at the upper end and then moves in the opposite direction to the hot gases produced by a flame at the lower end where a maximum temperature of 1450 °C is reached. The principal reactions taking place in a cement kiln are roughly subdivided as follows:

- *Reactions below ~ 1300 °C*: These are basically the calcination of carbonates (calcite and dolomite) and the decomposition of clay minerals (mainly de-hydroxilation). Above 900 °C, clays begin to form new phases such as Al-Si spinel,

cristobalite and, at 1100 °C, mullite ($Al_6Si_2O_{13}$). The reactions of the lime (CaO) formed from calcite with high-temperature polymorphs of SiO_2 and clay mineral decomposition products lead to the formation of belite (Ca_2SiO_4), aluminate ($Ca_3Al_2O_6$) and aluminoferrite (or simply ferrite, $Ca_4Al_2Fe_2O_{10}$). A liquid phase is formed only to a minor extent but may have a promoting effect on the reactions. At the end of this first stage, the major phases are high-temperature polymorphs of belite, aluminate and ferrite as well as a considerable amount of free lime.

- *Reactions between 1300 and 1450 °C (clinkering).* A considerable amount of melt is formed (up to 20-30% of the mix at 1450 °C), mainly from aluminate and ferrite. Much of the belite and nearly all the lime react to give alite (Ca_3SiO_5). The material starts to nodulize and form the clinker.
- *Reactions during cooling*. The liquid phase crystallizes giving mainly aluminate and ferrite while polymorphic transitions of the two Ca-silicates (alite and belite) occur. During this stage, clinker nodules (typically 3-20 mm in diameter) solidify completely, starting in a short cooling zone within the kiln and continuing in a cooler. As soon as the clinker leaves the burning zone, it is fundamental to achieve a rapid cooling from the clinkering temperature down to 1100 °C in order to avoid the decomposition of alite and obtain a high quality product.

At this point the clinker is mixed with a few percent of calcium sulphates (gypsum, bassanite, anhydrite) and finely ground (typically below 100 μm) thus obtaining the final product, i.e. Portland cement. Ca-sulphates control the process of setting and influence the rate of strength development. Other inorganic materials (generally referred to as mineral additions or supplementary cementitious materials, SCMs) may be ground together with the clinker and Ca-sulphates or mixed with Portland cement when this latter is used; in such cases the so-called composite or blended cements are produced. Mineral additions (often waste materials or by-products of industrial processes) can take part in the hydration reactions giving a substantial contribution to the formation of hydration products. Among the most important mineral additions are fly ash, blast furnace slag, natural pozzolanas, silica fume and limestone. Besides a re-use of waste materials with a consequent reduction of the manufacturing costs, the addition of SCMs allows to produce cements characterized by specific properties that are desirable for particular purposes such as slower and decreased heat evolution, improved durability or very high strength.

A typical chemical composition of an ordinary clinker appears as follows: 67% CaO, 22% SiO_2, 5% Al_2O_3, 3% Fe_2O_3 and 3% of other components (mainly SO_3, MgO, Na_2O and K_2O). Besides the four major clinker phases (alite, belite, aluminate and ferrite), several other phases such as alkali sulphates, CaO and MgO are commonly present in minor amounts. The setting and hardening of cement result from hydration reactions between the major phases and water (see par. 1.4).

1.2 Cement nomenclature and abbreviations

Chemical formulae in cement chemistry are often expressed as sums of oxides thus, for instance, tricalcium silicate (Ca_3SiO_5) can be written as $3CaO \cdot SiO_2$ even though this does not imply any presence of separate oxides within its structure. A specific cement chemistry notation is commonly used to abbreviate the formulae of oxides to simple letters; the abbreviations for the main oxides, clinker phases and hydration phases are reported in Tables 1.1 and 1.2.

CaO = C	Fe_2O_3 = F	K_2O = K	CO_2 = Č
SiO_2 = S	MgO = M	Na_2O = N	TiO_2 = T
Al_2O_3 = A	SO_3 = Š	H_2O = H	P_2O_5 = P

Table 1.1 - Abbreviations of common oxides following the classical cement chemistry notation.

Phase	**Chemical formula**	**Cement notation**
Alite	Ca_3SiO_5	C_3S
Belite	Ca_2SiO_4	C_2S
Aluminate	$Ca_3Al_2O_6$	C_3A
Aluminoferrite	$Ca_4Al_2Fe_2O_{10}$	C_4AF
Gypsum	$CaSO_4 \cdot 2H_2O$	$C\check{S}H_2$
Bassanite	$CaSO_4 \cdot 0.5H_2O$	$C\check{S}H_{0.5}$
Anhydrite	$CaSO_4$	$C\check{S}$
Portlandite	$Ca(OH)_2$	CH
Calcium silicate hydrate	$(CaO)_x(SiO_2)_y \cdot z(H_2O)$	C-S-H
Ettringite	$Ca_6Al_2(SO_4)_3(OH)_{12} \cdot 26H_2O$	$C_6A\check{S}_3H_{32}$
Monosulfoaluminate	$Ca_4Al_2(SO_4)(OH)_{12} \cdot 6H_2O$	$C_4A\check{S}H_{12}$
Hydrogarnet	$Ca_3[AI(OH)_6]_2$	C_3AH_6

Table 1.2 - Chemical formulae and cement chemistry abbreviated notations of the most important phases that can be found in cementitious materials.

1.3 The main clinker phases

Tricalcium silicate (C_3S) is the most important constituent of all normal Portland cement clinkers, ranging from 50 to 70 % by mass. The term alite refers to C_3S with ionic substitution as it is commonly found in clinkers. However, in the literature this rule is often not followed and C_3S and alite are commonly used as synonyms. In a typical alite, approximately 3-4% of substituting oxides is commonly observed. The most significant substituting ions in alite are Na^+, K^+, Mg^{2+}, Fe^{3+} for Ca^{2+} and Al^{3+}, P^{5+}, S^{6+} for Si^{4+}. The presence of substitutions in the structure contributes to the stabilization at ambient temperature of the high-temperature polymorphs. In particular, the M_3 and M_1 polymorphs (monoclinic) and in some cases the T_2 polymorph (triclinic) are the most commonly present in clinkers. Alite reacts relatively quickly with water and in normal Portland cements is the main responsible for strength development, especially at short-term hydration times. About 70 % of alite hydrates in the first 28 days while the remaining fraction completely reacts within one year.

Dicalcium silicate (C_2S) or belite when ionic substitutions occur, constitutes about 15-30 % of Portland clinker. As for C_3S, the higher temperature polymorphs cannot normally be preserved on cooling to room temperature unless stabilized by substituting ions (e.g. Fe^{3+}, Al^{3+}, K^+, Mg^{2+}, S^{6+}). In particular, the transformation upon cooling from the monoclinic β-C_2S to the much less dense orthorhombic γ-C_2S has to be avoided as it causes crystals of belite to crack and convert into a powder, a phenomenon known as dusting. However, belite generally contains enough stabilizing ions to prevent this destructive transformation. Belite reacts slowly with water, thus giving a small contribution to the strength during the first 28 days but its importance increases at later ages. After one year, the contributions to strengths from pure C_2S and C_3S are approximately equivalent under comparable conditions.

Tricalcium aluminate or simply aluminate (C_3A) is present in Portland cement clinker in proportions from 5 to 10 %. It is substantially modified in composition and also in structure by ionic substitutions. Pure C_3A has a cubic symmetry and does not exhibit polymorphism. In aluminate structure, Ca^{2+} can be substituted by $2Na^+$ (with consequent occupation of an otherwise vacant site) leading to a solid solution of general formula $Na_{2x}Ca_{3-x}Al_2O_6$. The substitution occurs without changes in structure up to about 1 % Na_2O. For increasing levels of substitution (up to 5.7 %), a series of structural re-

organizations are observed that lead to orthorhombic and monoclinic polymorphs. In addition, substantial proportions of aluminum can be replaced by other ions, mainly iron and silicon. Aluminate is commonly found in clinkers in the cubic or orthorhombic form. C_3A reacts very rapidly with water and can cause an undesired rapid setting but this effect is controlled by adding to the raw clinker an adequate amount of Ca-sulphates (mainly gypsum) acting as set-retarders.

Tetra-calcium aluminoferrite or simply ferrite (C_4AF) makes up 5-15% of normal Portland cement clinkers. C_4AF, which shows orthorhombic structure, is substantially modified in composition by variations in the Al/Fe ratio and ionic substitutions. Ferrite has small effects on the mechanical properties of cement and its rate of reaction with water appears to be variable but, in general, it is high at early stages and low or very low at later ages. At ordinary pressures, the composition of ferrite is expressed by the solid solution series $Ca_2(Al_xFe_{1-x})_2O_5$, where $0 < x < 0.7$. When $x = 0.5$, the C_4AF standard composition is obtained. However, the typical composition differs markedly from C_4AF due to the incorporation of about 10% of other oxides and is much lower in Fe_2O_3 as Fe^{3+} is often replaced by Mg^{2+}, Si^{4+}, Ti^{4+} or Mn^{3+}. Ferrite is also the main responsible for the typical dark colour of ordinary Portland clinkers. When a clinker grain is observed using an optical or electronic microscope, alite appears in the form of polygonal euhedral-subhedral crystals (typically 20-60 μm in size) while belite forms rounded crystals as it is partially consumed by its reaction with CaO to form alite. The interstitial fine-grained phases surrounding alite and belite grains are mainly aluminate and ferrite (Fig. 1.1)

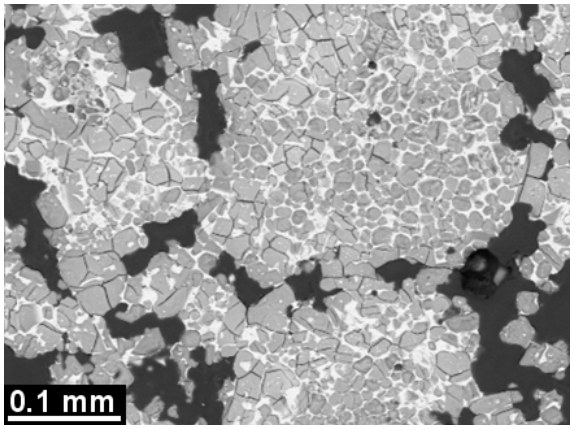

Figure 1.1 - SEM-BSE (back-scattered electrons) micrograph of a portion of a clinker nodule (polished section embedded in epoxy resin). Largest subhedral crystals correspond to alite while belite appears as well-rounded grains, slightly darker than alite. The interstitial fine-grained brightest phase is constituted by aluminate and ferrite. Darker areas are pores filled by epoxy resin.

1.4 The hydration of Portland cement

The hydration of Portland cement is a sequence of complex chemical reactions between clinker phases, water and Ca-sulphates, leading to setting and hardening (Gartner et al. 2002). As the analysis of reactions and kinetics becomes increasingly complex when increasing the number of component and phases, the investigation of simplified subsystems represents a valuable approach to the study of Portland cement hydration. This latter is far more complicated than the hydration of individual clinker phases because the different reactions proceed simultaneously and at different rates, thus influencing each other. However, the general principles are basically the same, with the dissolution of anhydrous phases that leads to the precipitation of much less soluble products forming the hardened paste. The setting process is the result of a change from a concentrated suspension of flocculated particles to a viscoelastic skeletal solid capable of supporting an applied stress and this can be monitored by rheological measurements. The continuous development of the solid framework by means of physico-chemical processes is called hardening and leads to the development of the ultimate mechanical properties of cement. The hydration reactions can proceed for years, until either one of the reactants (cement, water) is completely consumed or the space to deposit new hydration products is totally filled. It has to be pointed out that the hydration behaviour of clinker phases can be affected by several factors, the most important being w/c ratio, temperature, particle size distribution, mixing procedure, size of the hydrating sample and presence of admixtures.

The hydration of clinker silicates (alite and belite) produces two main phases, calcium silicate hydrate (C-S-H) and calcium hydroxide (also known as Portlandite, CH). Calcium silicate hydrate is a low-crystallinity (or nearly amorphous) phase of variable stoichiometry; for these reasons it is sometimes also referred to as C-S-H gel. C-S-H gives by far the most important contribution to the development of mechanical strengths in cements, forming in general highly intergrown fibres that lead to the hardening of the system. Portlandite has a layered hexagonal structure showing good (0001) cleavage. Under ideal conditions of formation, CH forms hexagonal plates but as hydration proceeds it tends to become massive with a not well defined shape. The hydration of C_3S and C_2S under ambient conditions can be described by the following reactions:

$$C_3S + (3\text{-}x+n)H \rightarrow C_xSH_n + (3\text{-}x)CH \quad (\Delta H = -121 \text{ kJ/mol}) \quad (1.1)$$

$$C_2S + (2\text{-}x+n)H \rightarrow C_xSH_n + (2\text{-}x)CH \quad (\Delta H = -43\ kJ/mol) \quad (1.2)$$

When the solution is saturated with respect to CH, x = 1.7 and n = 4, thus eq. 1.1 and 1.2 become:

$$3C_3S + 16H \rightarrow 3C_{1.7}SH_4 + 4CH \quad (1.3)$$

$$3C_2S + 13H \rightarrow 3C_{1.7}SH_4 + CH \quad (1.4)$$

An initial stoichiometric water to cement ratio (w/c) of 0.42 is necessary for a complete reaction. As C_3S constitutes about 50 to 70% by mass of normal clinkers, its hydration is the dominant process in Portland cement hydration, especially during the early stages of strength development. For this reason, the great majority of studies aiming at understanding the mechanisms and kinetics of cement hydration concentrated on C_3S (e.g. Bullard et al., 2010).

The generally accepted interpretation of the process implies that from the hydration of aluminate and ferrite, completely different phases are formed. As already observed, C_3A is the most reactive clinker phase and is known to have a significant influence on the setting process and rheology of cementitious systems. In the absence of sulphates, aluminate reacts with water to produce initially a gel-type material whose crystallinity increases with time. This leads to the growth of the so-called hexagonal hydrates, with compositions C_2AH_8 and C_4AH_{19} (eq. 1.5). Such phases are metastable and are converted to more stable cubic forms as for example C_3AH_6 (hydrogarnet, eq. 1.6) leading to an increase in porosity and disruption of microstructure with consequent loss of strength. C_4AH_{19} easily loses part of its interlayer water to form C_4AH_{13}.

$$2C_3A + 27H \rightarrow C_4AH_{19} + C_2AH_8 \quad (1.5)$$

$$C_4AH_{19} + C_2AH_8 \rightarrow 2C_3AH_6 \quad (1.6)$$

In general, such phases do not contribute significantly to early strength development and, due to their fast reactions, cause an undesired rapid setting of cement. For this reasons in normal systems, gypsum or other Ca-sulphates are added to retard setting. The first stable hydration product under these conditions is ettringite (eq. 1.7), a fibrous phase that grows in the first tens of minutes on the surface of C_3A and gives a fundamental contribution to the development of early strengths. Ettringite is part of a group known as Aft phases with limited variations in composition.

$$C_3A + 3C\check{S}H_2 + 26H \rightarrow C_6A\check{S}_3H_{32} \text{ (ettringite)} \quad (1.7)$$

With increasing hydration times, monosulphoaluminate (or simply monosulphate, eq. 1.8) gradually replaces ettringite that becomes unstable because the ratio of available alumina to sulphate increases with continued cement hydration. On first contact with water, most of the sulphate is readily available to dissolve, but much of the C_3A is contained inside cement grains with no initial access to water. Continued hydration gradually releases alumina and the proportion of ettringite decreases as that of monosulphate increases:

$$C_6A\check{S}_3H_{32} + 2C_3A + 4H \rightarrow 3C_4A\check{S}H_{12} \quad (1.8)$$

$$C_3A + CH + 12H \rightarrow C_4AH_{13} \quad (1.9)$$

Monosulphate can form a solid solution with the isostructural compound C_4AH_{13} (eq. 1.9). However, besides OH^-, also CO_3^{2-} can partially substitute SO_4^{2-} in the interlayer positions; in addition, also Fe^{3+} may substitute Al^{3+}, resulting in wide compositional variations. Therefore, such compounds are collectively grouped within the so-called AFm phases, where m stands for “mono”, indicating the presence of a single sulphate group in the formula. In a similar way in Aft phases, t stands for “tri“ as they contain three sulphate groups.

The hydration of the ferrite phase is very similar to that of aluminate and leads to the formation of iron-substituted Aft and AFm phases. Ferrite reaction also starts quickly as water is added but then slows down, probably because a layer of iron hydroxide gel forms, coating the ferrite and acting as a barrier, preventing further reaction.

The early stages of hydration, both for total cement and single phases, are commonly followed by monitoring the rate of heat evolution by means of an isothermal calorimeter or by measuring the rate of release of Ca^{2+} into solution. In particular, on the basis of calorimetric curves, the overall progress of hydration has been historically divided into four or five stages as illustrated in Fig. 1.2. Even though the limits of each stage are still difficult to define, this classification represents a good starting point for the understanding of cement hydration. Following a scheme proposed by Gartner et al. (2002), the mechanisms of cement hydration can be summarized as follows:

1- *Initial reaction* (first minutes, corresponding to wetting and mixing). A rapid dissolution of free lime, sulphates and aluminates occurs with an immediate

formation of Aft phases (initially as a gel layer); C_3S starts to hydrate on its surface. A large initial burst of heat is observed, mainly due to the dissolution of C_3A and C_4AF and secondarily to C_3S and CaO.

2- *Period of slow reaction* (also known as dormant or induction period). A gel made of C-S-H nucleates and the concentrations of Si and Al in the pore solution decrease to very low levels; the nucleation of portlandite also occurs. During this stage a low heat evolution rate is measured. Slow formation of early C-S-H and more Aft phases leads to an increase of viscosity.

3- *Acceleration period* (corresponding to setting and early hardening). The hydration of C_3S to form C-S-H and CH accelerates and reaches a maximum, with an increasingly high heat flow. The rapid growth of hydrates leads to a reduction of porosity and to the solidification of the paste (early strength development).

4- *Deceleration period*. The rate of formation of C-S-H and CH from both C_3S and C_2S decreases. A renewed hydration of aluminates produces mainly AFm phases; AFt may dissolve or re-crystallize. The continuous decrease in porosity due to the growth of hydration phases leads to a continuous increase of strengths. The rate of reactions decreases with time but hydration continues for years, as long as water is available. Shrinking of the paste is observed due to drying.

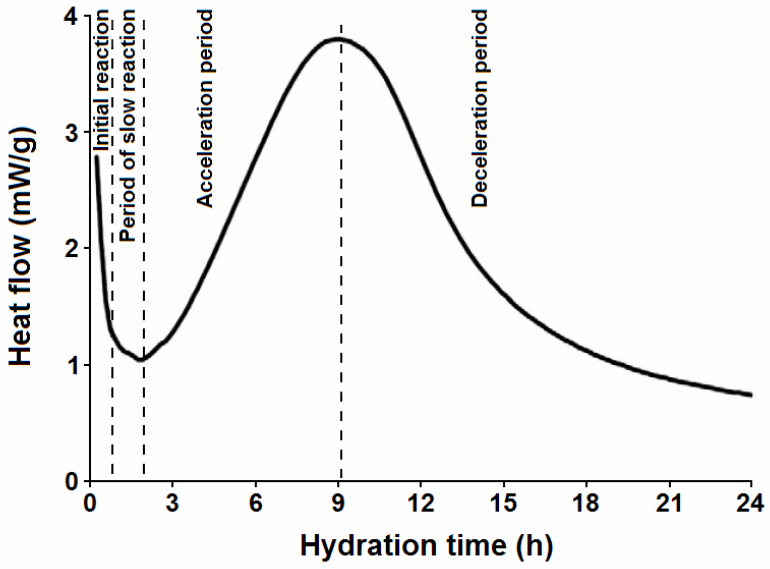

Figure 1.2 - Calorimetric curve showing the rate of hydration as a function of time for an alite paste. A similar shape of the graph is obtained also for normal Portland cements (image modified from Bullard et al., 2010).

In concretes and mortars, i.e. when aggregates (sand and/or gravel) are added to the mix, the development of bonds at the interface between the paste and the aggregates is another crucial aspect that contributes to final strengths. If specific properties have to be achieved, the reactions and kinetics of the hydration process can be significantly modified by the addition of supplementary cementitious materials or chemical admixtures as discussed in the next paragraph.

1.5 Chemical admixtures: superplasticizers

1.5.1 Water reducers and superplasticizers

All the materials other than hydraulic cements, water or aggregates that are added to a cementitious system immediately before or during mixing are defined as admixtures. Other materials such as grinding aids that are added to cement during manufacture are not included in this classification (Taylor, 1990). A large variety of admixtures, both organic and inorganic, may be employed in order to achieve specific properties as for example an acceleration or delay of setting and hardening, a decrease of the amount of water needed to obtain a given level of workability or an increase of the entrained air content.

It is well known that a reduction of the water to cement ratio in cements, mortars and concretes leads to an improvement of the mechanical strengths and durability of the final products, as a consequence of the higher degree of packing of cement particles and the development of stronger inter-particle bonds. However, these beneficial effects are in general achieved at the expenses of workability, making the mix more difficult to place. On the other hand, too much water will result in segregation of the aggregate components from the cement paste. Moreover, water that is not consumed by the hydration reactions may leave the concrete as it hardens, resulting in microscopic pores that will reduce the final strength of the concrete/mortar. A mix with too much water will also experience more shrinkage as the excess water leaves, resulting in internal cracks and visible fractures which again will reduce the final strength.

Water-reducing agents, also called plasticizers, allow to reduce the w/c ratio of a cement mixture (typically in the range of 5-15 %) maintaining at the same time high levels of workability. The main limitation of conventional plasticizers is related to the fact that many of them also have retarding, accelerating or air entraining properties. For this reason, in order to avoid undesired effects, they cannot be used at high dosages and are typically added as solutions in concentrations of up to 0.2 % on the weight of cement. Nowadays,

conventional plasticizers have been almost completely replaced by a novel generation of admixtures called superplasticizers (SPs) or high-range water reducers, which allows to partially or completely overcome the limitations of common water reducers. Superplasticizers allow to produce high-strength and high-durability concretes by reducing the w/c ratio up to about 30% and are widely used, both in ordinary and special applications, to improve the workability of mortar and concrete systems.

Among the most common conventional plasticizer are Ca- and Na-lignosulphonates which are also widely employed as set retarders. In fact, a large overlap of properties exists between plasticizers and set-retarding admixtures as they both act by similar mechanisms of adsorption at the solid-liquid interface. Water reducers are also known to enhance the slump loss effect (i.e. the decrease in workability of cement and concrete mixtures with time after mixing); nonetheless, the slump remains significantly higher if compared to normal systems. Such increased slump loss is probably due to the gradual absorption of the admixture by the growing cement hydration products (Taylor, 1990) and may be minimized by delaying the addition of the admixture until a few minutes after mixing.

Unlike conventional water reducers, superplasticizers can be used in higher concentrations (over 1% on the weight of cement) without causing an excessive retardation or air entrainment. In addition, SPs may be also employed at normal w/c ratios in order to produce "flowing" concretes with self-levelling capabilities that can be readily placed by methods such as pumping or continuous gravity feed. Superplasticizers are anionic poly-electrolytes with molecular weights approximately in the range of 10^3-10^5 u. The so-called "first generation" SPs are roughly classified into three principal types, namely sulphonated melamine formaldehyde poly-condensates (SMF), sulphonated naphthalene formaldehyde poly-condensates (SNF) and modified lignosulphonate compounds.

1.5.2 PCE superplasticizers

In the middle of the 1980s, a new class of superplasticizers, based on polycarboxylate ethers (PCE) and characterized by improved performances and higher environmental compatibility has found increasing applications. Such molecules typically consist of an adsorptive backbone unit and a hydrophilic polyethylene-oxide (PEO) side chain. Though being in general less robust or tolerant to different cement compositions or other admixtures than SMF and SNF polycondensates, much lower w/c ratios can be achieved using PCE SPs, especially in pre-cast concretes. Generally, the performance of PCE

superplasticizers is strictly related to their architecture (Plank et al., 2008, Zingg et al., 2009) and is determined by parameters that can be conveniently modified such as backbone and side chain length and side chain density. Due to their advantages, these superplasticizers are increasingly replacing conventional poly-condensates, especially in high-performance demanding applications such as self-compacting concretes (SCCs) or high performance concretes (HPCs).

The most commonly used PCE superplasticizers are manufactured from the radical copolymerization of methacrylic acid and the methoxy-terminated ester MPEG-MA (methoxy polyethylene glycol methacrylate). By means of this process, "comb-like" structured polymers are obtained in which the PEO side chains allow for the steric stabilization of dispersed particles. The admixtures employed for the preparation of some of the samples studied in this work belong to this class, as shown in Fig. 1.3. An alternative formulation involving the use of the hydroxyl-terminated HPEG-MA macro-monomer instead of MPEG-MA has been recently developed by Plank et al. (2008).

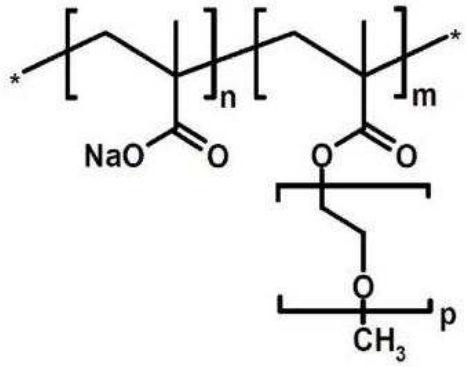

Figure 1.3 - General structural formula of the PCE-based superplasticizers employed in the present work. The subscript *n* denotes the number of repeat units of methacrylic acid (which bears the negative charge in the polymer) while *m* represents the number of repeat units of the molecule bearing the PEO chain. The number of oxyethylene units, which determine the molecular weight of the side chain is indicated with *p*. For the superplasticizers used in this work, the ratio *n/m* may vary between 3 and 7 while the molecular weight of the MPEG chain is approximately comprised between 750 and 5000 u. Image from Zingg et al. (2009).

1.5.3 Mechanisms of cement-SP interaction

The addition of superplasticizers causes modifications at the interface between particle surface and pore solution and influences the physical properties of the paste such as

viscosity and yield stress. However, despite the significant efforts of the scientific community, many questions remain unsolved about the mechanisms that govern the interaction between cement and SPs. Here, we will briefly report the generally adopted theory used to explain their behaviour though the actual performance can be rather different for various cement-SP combinations. It is widely agreed that the reduction of mixing water is achieved through improved dispersion of the cement grains which causes a strong decrease of flocculation. In this way, a significant amount of water, otherwise immobilized within particle clusters, becomes available allowing an increased fluidity of the paste. According to Daimon & Roy (1978), adsorption of the admixture on the hydrating cement grains could decrease flocculation in at least three ways, namely an increase of the zeta-potential, an increase of the solid-liquid affinity and a steric hindrance. Besides being adsorbed on particle surfaces (both clinker and hydrate phases), SP molecules can also be intercalated by co-precipitation with early hydration products or remain dispersed in the pore solution (Fig. 1.4).

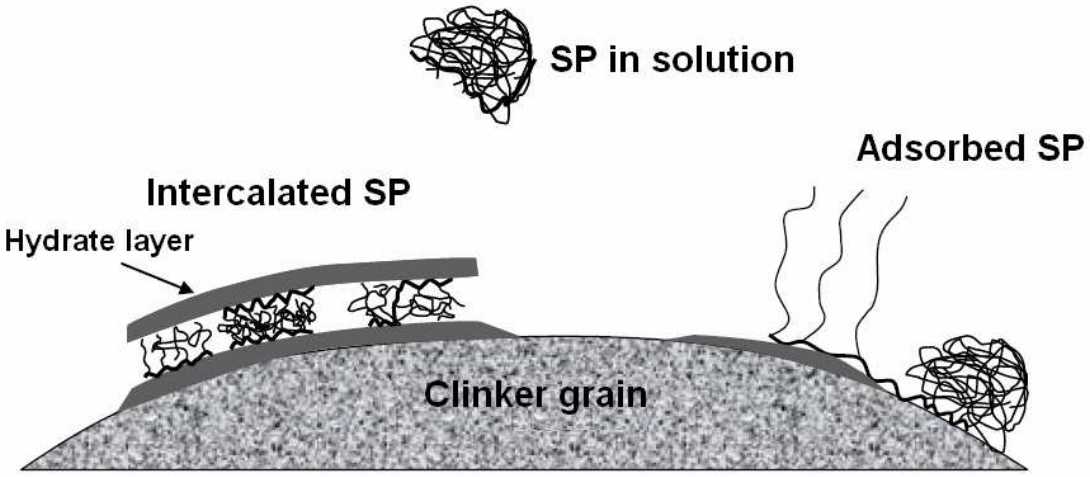

Figure 1.4 - Different mechanisms of cement-superplasticizer interaction (image modified from Zingg, 2008).

SP intercalation in layered cement hydration phases reduces the amount of SP available for adsorption with negative effects on the stability of cement suspensions as an increased slump loss. As already observed for plasticizers (whose mechanisms of action are quite similar to those of SPs), the delayed addition of admixtures (i.e. after the initial hydration) seems to limit or prevent the formation of intercalates. This is confirmed by the lower demand of superplasticizer in those systems where SP is added after a few minutes instead of directly with the mixing water. SP intercalation is generally observed in aluminate

hydrates as monosulphate (Plank et al., 2006) but it has been described also in C-S-H (Matsuyama & Young, 1999). The presence of SPs in the pore solution is known to influence the nucleation of hydration phases as well as their growth and crystal shape, as confirmed by SEM and AFM (atomic force microscopy) investigations. Such microstructural modifications of course have relevant effects on the inter-particle forces and rheological properties of cement suspensions.

2 - X-ray computed micro-tomography

2.1 Non-destructive investigation of cements

Monitoring the microstructural evolution and the chemical reactions taking place in cement-based materials during their setting and hardening is one of the most challenging goals of modern materials science. It is widely acknowledged that the performances and durability of cements, mortars and concretes are controlled by their microstructural features such as the pore network and the spatial relationships between different phases. Among the most widely used experimental techniques for the investigation of microstructural features in cements, scanning electron microscopy (SEM) has played a major role in the past and still remains a fundamental tool in this research field. The combination of backscattered electron (BSE) imaging with X-ray EDS (energy dispersive spectroscopy) point analyses and chemical maps allows to easily identify and quantify both clinker phases and hydration products. Moreover, morphological information on the hydrated phases and the pore space may also be obtained by using secondary electron (SE) imaging on fresh surfaces. However, such analyses are limited to the investigation of surfaces and this lack of access to the third dimension represents one of the major limitations of SEM-based techniques when trying to extract quantitative information, e.g. on connectivity or other pore space properties. Another critical aspect is related to sample preparation (i.e. cutting, polishing and drying) and to the exposure to high vacuum conditions inside the SEM chamber that may induce some modifications in the microstructure of hydration phases. Even though these limitations have been partially overcome by the advent of the environmental SEM technology (ESEM) which allows to analyze hydrated specimens with no prior drying, the problems related to sample cutting and polishing still remain unsolved.

In the materials and Earth science research fields, the most popular traditional approach to overcoming the limitations of bi-dimensional (2D) imaging techniques has been to cut serial thin sections or to perform serial grinding and polishing, coupled with optical or SEM imaging. These methods are of course highly destructive and time-consuming; moreover, sections can only be cut/grinded in one orientation. In addition, the achievable resolution is quite limited, in particular for what concerns serial thin sectioning where a minimum interval of ~ 1-2 mm is lost between one section and the other during sample preparation. Under these conditions, the correlation between features observed on different

planes may represent a very difficult task. For these reasons, the development of non-invasive experimental techniques which allow the detailed investigation of the inner structure of materials has become necessary. Nowadays, X-ray computed micro-tomography (X-μCT) enables the internal microstructure of totally undisturbed samples to be visualized in a three-dimensional (3D) manner at the sub-micrometric scale. In general, X-ray tomographic methods allow to produce, by means of a mathematical reconstruction process, cross-sectional images of an object based on how it attenuates X-rays; if stacked together, such images, also called *slices*, can provide a 3D representation of the investigated sample in a totally non-invasive manner. The resulting data can be virtually cut into an infinite number of sections in any desired orientation or visualized with various 3D techniques.

2.2 History

Modern X-ray computed micro-tomography (X-μCT), as applied in this work, represents the high-resolution evolution of the X-ray computed tomography technique (XCT), originally developed for medical purposes (CT scan or CAT, computed axial tomography) in the late 1960s and early 1970s, in order to overcome the limitations of conventional 2D X-ray radiography. The invention of medical CT is generally attributed to Godfrey N. Hounsfield (1919-2004) (Hounsfield, 1973). His revolutionary idea consisted in the acquisition of a large number of radiographs of an object (the body of the patient or a part of it) from different angular positions around a rotation axis, followed by the application of a mathematical reconstruction algorithm to calculate a map of the X-ray attenuation coefficient (μ) of any volume within the body. In this way, the variations in density and composition of bones and internal organs could be visualized with improved detail if compared to classic X-ray radiography. At that time, the problem of obtaining a section of an object using an infinite set of rays passing through it, had been already solved theoretically in 1917 by the Austrian mathematician Johann Radon (Radon, 1917). He demonstrated the existence of an inverse transform (the inverse Radon transform) which can be used to provide a map of the variations of μ within a slice of an object, once a set of radiographic projections is available. However, the contribution of Allan M. Cormack who many years later, in 1963, formulated some of the mathematical principles for tomographic reconstruction, is considered equally fundamental to the development of medical CT. For their invention, Hounsfield and Cormack were awarded the 1979 Nobel Prize in

Physiology or Medicine. Soon after its first appearance in the medical field, computed tomography started to be used for the investigation of non-living structures in industry, where all the issues related to radiation dose limits are in practice almost irrelevant. However, the use of XCT in this field was initially limited due to its low spatial resolution (in the order of 1 mm). In the last fifteen years, the technological innovations in the fields of X-ray sources and detectors, pushed the resolution limit below 50 μm, leading to the development of a novel, high resolution version of XCT and extending its use to the material research field, where the size of the features to be observed is typically several orders of magnitude lower than in human body. This technique is commonly referred to as X-ray computed micro-tomography (X-μCT). Nowadays, with the most recent X-μCT systems, the micrometric or even sub-μm resolution range has become accessible, opening new perspectives for the non-destructive analysis of materials. In the last decade, X-μCT has found an increasing number of applications both in industry (e.g. reverse engineering, metrology or quality control) and in a great variety of research fields as for example material science (foams, cements), geology, archaeology, palaeontology, civil and mechanical engineering, biology, biomedicine and many others.

For the sake of completeness, it has to be pointed out that X-ray computed tomography is not the only non-invasive 3D imaging technique available, though it is the most widely employed. Other experimental methods as for example magnetic resonance imaging (MRI) and neutron computed tomography (NCT) can be used for the detailed visualization of the internal structure of materials. In particular, NCT works on the same basic principles of XCT, with the main differences being the nature of the probe used (thermal or cold neutrons instead of X-rays) and the lower spatial resolution achievable. XCT and NCT can be considered as two complementary techniques because the fundamental mechanisms of neutrons interaction with matter largely differ from those of X-rays, thus implying very different attenuation properties of the various elements for the two kinds of radiation. Neutrons interact with the core of the atom, while X-rays interact with the charge distribution of the electron shells. Therefore, the X-ray attenuation coefficient increases with the atomic number of the elements (i.e. with the number of electrons). On the other hand, the interaction probability of neutrons with the nuclei is described by the total microscopic cross-section (σ_{tot}), which does not systematically vary as a function of the atomic number and, consequently, the attenuation properties of the elements for neutrons show an irregular behaviour. For instance, neutrons are very sensitive to some light

elements such as H, Li, and B, which absorb X-rays only weakly and therefore do not provide a good X-ray imaging contrast but they do for neutrons. For this reason, NCT is particularly useful for the detection of hydrated compounds. Moreover, neutrons easily penetrate thick layers of metals such as Fe, Cu and Pb which are known to cause a very high absorption of X-rays.

2.3 Basic principles

X-ray absorption imaging (which includes both conventional radiography and tomography) is based on the irradiation of a sample with X-rays and on the detection of photons transmitted through it. The change in intensity of X-rays after passing through an object is described by the well-known Beer-Lambert law which relates the incident intensity (i.e. number of photons, I_0) and the transmitted intensity (I) to the X-ray linear attenuation coefficient (μ or L.A.C.) according to the following equation:

$$I = I_0 \exp\left[-\sum_i (\mu_i x_i)\right] \qquad (2.1)$$

where each increment i represents a single material with an attenuation coefficient μ_i and x_i is the length travelled by X-rays through that material. For each single material, μ is related to the density of the phase (ρ), its mean atomic number (Z) and the energy of the radiation used (E). In general, the values of μ decreases as X-ray energy increases. In many practical cases, it may result convenient to use the mass attenuation coefficient (defined as μ/ρ) instead of μ.

As previously noticed, X-rays interact mainly with the electrons of the atomic shells. In the energy interval commonly used in X-ray imaging, the amount of attenuation is mainly determined by two physical processes, photoelectric absorption and Compton (inelastic) scattering. For X-ray energies up to 50-100 keV (i.e. the most widely used) the first one is the dominant process and μ/ρ is strongly dependent on E and Z. This is commonly described by the following equation:

$$\frac{\mu}{\rho} = K\frac{Z^4}{E^3} \qquad (2.2)$$

where K is a constant. At higher energies, the role of Compton scattering progressively increases its importance and the dependence of μ from Z and E can be considered significantly weaker. For these reasons, compositional variations have a major impact on

image contrast at low energies whereas at higher values, contrast mainly depends on density differences. Although lower energy X-rays provide greater sensitivity, the selected energy for each experiment cannot be too weak, in order to ensure adequate penetration and signal-to-noise ratio.

The main limitation of conventional radiographic techniques is related to their lack of depth resolution. In fact, radiographs only record a 2D absorption representation of a 3D object, therefore small details are not readily identified due to the overlapping of different features along the X-ray path (Fig. 2.1). The development of X-ray computed tomographic techniques allowed to overcome this limitation.

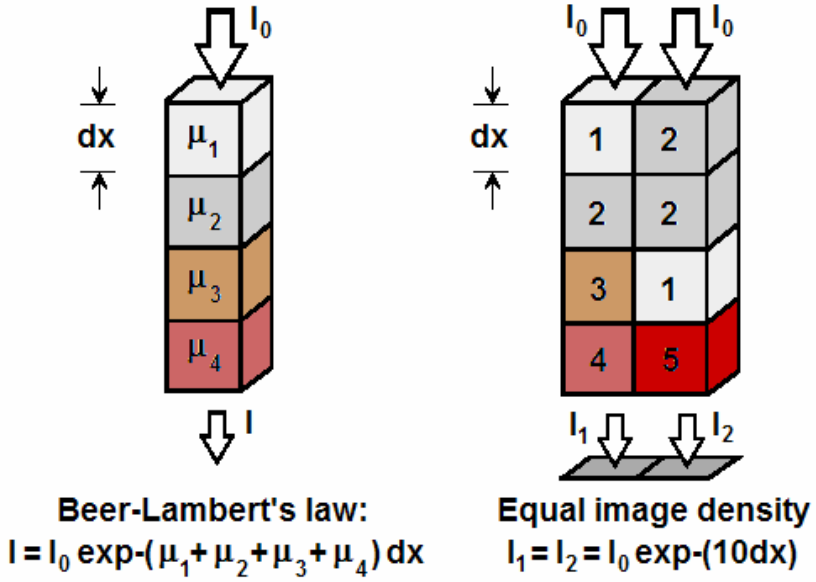

Figure 2.1 - Schematic representation showing the mechanism of image formation in conventional 2D radiography. Even though the two columns on the right contain volume elements with different linear attenuation coefficients, the same transmitted intensity is measured along both paths. In other words, what is detected is the integrated contribution of the linear attenuation coefficients without any information about the contribution from any individual volume element.

In general, a typical experimental setup for X-ray computed tomography consists of three parts, namely an X-ray source, a rotating sample holder and a detector, whose synchronization is controlled by a computer. A large number of co-planar radiographic projections (up to several thousands) is acquired with the sample being rotated relative to the source-detector pair by small angular steps (in medical CT systems, the source and the detector rotate around the patient's body which remains fixed). Once all the projections are available, a reconstruction algorithm can be applied to produce a stack of cross-sectional

images called *slices*, each one representing what would be seen if the investigated object was cut along a plane perpendicular to its rotation axis. Each reconstructed slice is actually a matrix of *voxels* (volume elements) whose grey values (GVs) are proportional to the mean X-ray attenuation coefficient within the corresponding volume of material (i.e. dark for low- and bright for high-attenuating features). Conversely, the grey scale traditionally adopted in radiographs is inverted and higher absorption values correspond to darker GVs. It has to be pointed out that a voxel differs from a pixel, as it is a 3D element, whose thickness corresponds to the thickness of one slice; therefore, if all the reconstructed slices are stacked together, a 3D digital representation of the investigated object is obtained. The reconstructed volume data can be visualized and processed using adequate imaging techniques, allowing the extraction of several features of interest.

According to the size and the composition of the object to be investigated, the experimental setup may show a high degree of variability, especially in terms of scanning geometry and energy of the source. The resolution of the technique (i.e. the capability to separate two distinct objects that are located close to each other) largely depends on the size of the sample; in general, the smaller the sample to be investigated, the higher the spatial resolution achievable. In medical and industrial XCT scanners, where the size of the objects typically ranges from several tens of centimetres to a few meters, the spatial resolution is in the order of ~ 1 mm. On the other hand, modern X-μCT systems employed in materials research allow to study samples with much smaller sizes (from a few cm to a fraction of mm) with an extremely high resolution (from ~ 20 μm to less than 1 μm).

According to the scanning geometry, XCT systems have been traditionally classified, following their evolution through time, from the simplest to the most complex. In the so-called *first generation* CT systems, a collimated, monochromatic beam is used to scan the sample and the transmitted photons are collected by a single point-detector. A translation of the source-detector pair relative to the sample (or vice versa) by small lateral steps, allows the incident beam to cross the object through a high number of different, parallel paths. By rotating the object (or the source-detector pair) by small angular intervals around its vertical axis and repeating at each time the translation, it is possible to investigate an entire slice of the sample. By vertically moving the object and repeating the described procedure, other slices can be reconstructed. This technique is of course very time-consuming but on the other hand, due to the parallel geometry of the beam, a higher precision in image reconstruction is obtained and only a 180° rotation is required.

In order to reduce acquisition times, in *second generation* systems a horizontal linear detector is used in combination with a fan-shaped divergent beam. This is roughly equivalent to performing several measurements at the same time, thus reducing the number of lateral steps. On the other hand, due to the non-parallel beam, the sample needs to be rotated through 360°. This geometry is commonly used in industry for scanning very large objects (e.g. engines), often coupled with high-energy sources.

A linear detector is used also in *third generation* instruments but in this case it is wide enough for the whole sample to be projected over it, hence lateral translation of the sample is no more necessary. A larger fan beam is used and, as for second generation systems, a 360° rotation is needed and vertical translation of the sample is still required for imaging different slices of the sample. If rotation and vertical translation are performed simultaneously, the so-called *spiral CT* is produced, which represents the most widely used geometry in modern medical CT systems. In this kind of instruments, the source and the detectors are located on a circumference surrounding the patient's body (which remains fixed) and are continuously rotated and translated in a direction perpendicular to the slice plane. In modern medical CT scanners, several rings of detectors are present, allowing the imaging of multiple slices at the same time.

Nowadays, in modern X-μCT applications (i.e. for small samples where high resolution is required), the most widely used approach consists in adopting a geometry where the entire sample is totally immersed in the X-ray beam at any time of the rotation. The transmitted photons are collected by a planar detector (typically a CCD), allowing considerably faster acquisitions. As the X-μCT systems used for all the experiments presented in this work belong to this latter group, they will be described in more detail in the next paragraph.

2.4 Microfocus and synchrotron-based X-μCT systems

In general, modern X-μCT systems are classified into two main groups on the basis of the X-ray source employed. In conventional laboratory apparatuses, the X-ray source is a microfocus tube (i.e. a tube with a micrometric focal spot) which produces a conical and polychromatic beam. On the other hand, synchrotron-based systems allow the user to work with a practically parallel and highly brilliant beam, whose energy can also be accurately selected using monochromators. A scheme of a typical laboratory CT-system with cone-beam geometry is illustrated in Fig. 2.2.

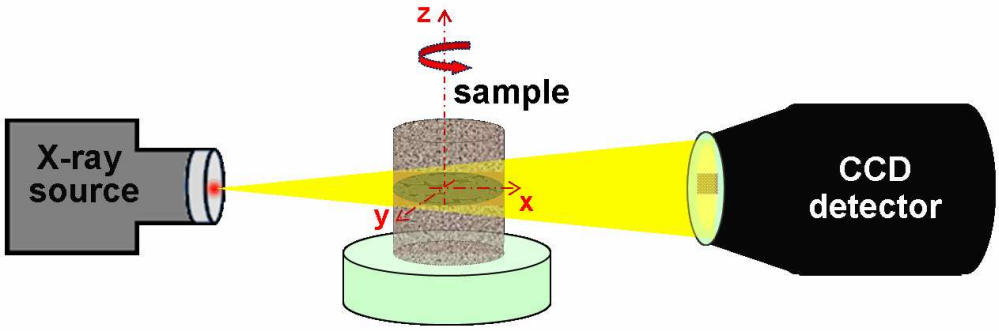

Figure 2.2 - Schematic representation of a typical experimental setup for laboratory X-μCT using a cone-beam geometry. The synchronization of all the components is controlled by a dedicated computer (not shown in figure).

In microfocus systems, due to the cone-beam geometry, a complete 360° rotation is needed and the image of the sample which is projected on the detector is typically enlarged. The level of magnification can be selected by changing the mutual distances between source, object and detector. If the source-detector and source-object distances are indicated respectively with D_{SD} and D_{SO}, the geometrical magnification factor (M) is given by:

$$M = \frac{D_{SD}}{D_{SO}} \qquad (2.3)$$

Of course, the correct value of M should be chosen considering the maximum sample diameter, in order to not exceed the field of view of the CCD. An experimental configuration with the sample positioned as close as possible to the source window is generally preferable. However, due to the strong decrease of photon flux with distance, the detector should not be placed too far from the source in order to keep the exposure times at reasonable values during data collection. The magnification factor, the detector pixel size and the focal spot size of the source are the main parameters which determine the spatial resolution. In particular, at large magnifications with high resolution detectors, the maximum resolution achievable is limited by the geometrical unsharpness effects which arise because the radiation does not originate from a single point source, but rather from a small area, as illustrated in the schematic representation of Fig. 2.3. Nowadays, spatial resolutions in the range of 5-10 μm are easily achieved with many commercial laboratory instruments even though the best results are obtained using synchrotron-based systems which enable to reach the sub-micrometric scale.

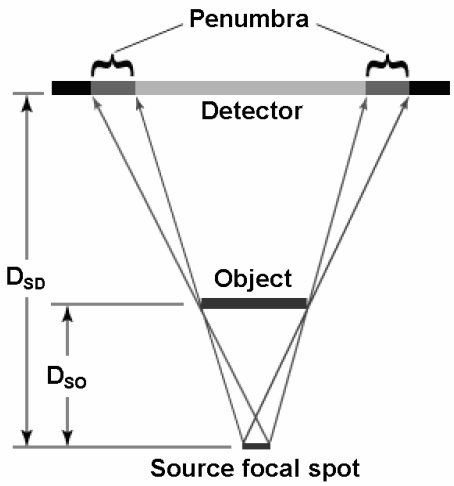

Figure 2.3 - Mechanism of geometrical unsharpness generation in X-ray imaging due to the finite size of the focal spot of the source. A penumbra region appears which causes the edges of the object to be less defined.

When the radiation produced at synchrotron facilities is used, the beam can be considered as practically parallel because the source is very far from the sample (typically in the order of 30-100 m). This implies that no geometrical magnification is obtained and the spatial resolution mainly results from the effective pixel size of the detector. For this reason, additional optics have to be included in the detection system in order to improve the image resolution. Nonetheless, the parallel geometry has the great advantage that, in all the projections obtained by rotating the sample around its axis, each slice at a given height does not depend on other slices, whereas in conical beam geometry this is not true. The 3D reconstruction problem thus reduces to a large number of 2D problems, with each row of the detector corresponding to a single slice within the sample volume, allowing the use of simplified and more exact reconstruction algorithms. In addition, due to the parallel beam, the acquisition of projections over a 180° angular range is sufficient. Another advantage of synchrotron-based systems is related to the extremely high photon flux available at these facilities which is approximately six orders of magnitude higher than in conventional laboratory X-ray tubes. This allows the users to obtain an excellent signal-to-noise ratio (hence faster acquisition times) even when a single X-ray energy is selected from the polychromatic synchrotron light (the so-called white beam) by using monochromators. The use of a single-energy radiation is usually preferred because it allows to avoid one of the most annoying artefacts observed when using polychromatic sources, the beam hardening effect (see par. 2.7.2), which is related to the preferential attenuation of the lower energy

photons while they travel through the sample. This represents a crucial point for a more accurate and quantitative determination of the variations of μ within the sample. In addition, it is possible to adjust the X-ray energy to the absorption edge of one of the elements present in the sample, thus allowing for contrast enhancement by calculating the difference of the images taken below and above the absorption edge of a selected element. This method is known as *absorption-edge tomography* (Bonse et al., 1989, Thurner et al., 2004).

2.5 Basic principles of tomographic reconstruction

The main purpose of an XCT system is to build a 2D or 3D representation of the inner structure of an object from a set of projection data acquired from a large number of points of view. Several reconstruction algorithms, specifically developed for the different geometries are nowadays available, as for example filtered back-projection (FBP), and algebraic reconstruction techniques (ART). A mathematical description of these methods is beyond the aim of the present work but can be found in several specific texts, e.g. Natterer (1986), Kak and Slaney (1988) and Kuba & Herman (2008). Only a brief, schematic description of the basic principles of filtered back-projection, which is the most widely used algorithm, will be given here.

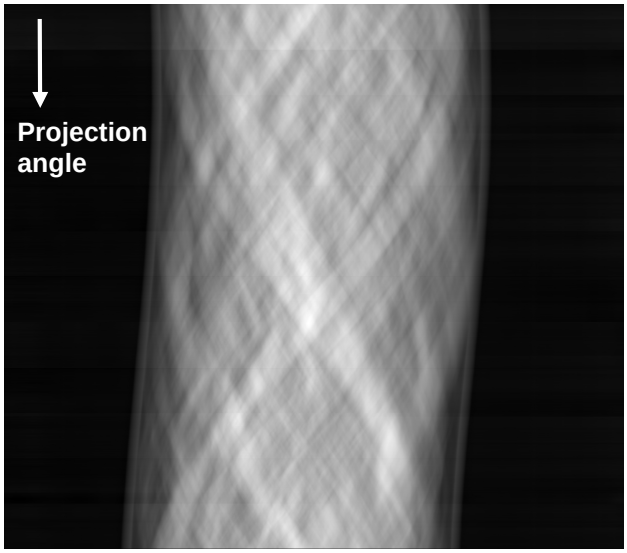

Figure 2.4 – Set of projections (or sinogram) over a 180° rotation (synchrotron parallel geometry) for a single slice of a cement sample contained in a glass capillary tube (Ø ~ 400 μm). The image is a matrix of 2048x1800 pixels, corresponding respectively to the number of elements in a line of the detector and to the total number of angular projections acquired.

The popularity of filtered back-projection is due to the fact that this reconstruction method ensures a very good balance between spatial accuracy, noise reduction and computational expense. In order to describe how reconstruction is carried out using FBP, it may be useful to refer for simplicity to the parallel-beam geometry. Initially, for a single slice (i.e. for a single row of the detector), the 1D projections recorded at each angular position can be ordered one below the other and displayed as a single image which is called *sinogram* (Fig. 2.4) because with this representation a point of the object describes a sinusoidal trajectory. In practice, each sinogram corresponds to the Radon transform of one bi-dimensional slice. Once a set of projections from different angular positions is obtained, the first intuitive operation which can be implemented for slice reconstruction is back-projection (Fig. 2.5 & 2.6). It consists in assigning to each point of the object, the average value of all the projections at the corresponding position for each rotation. Nonetheless, the back-projected image which is obtained using this procedure is highly blurred. In fact, as a result of the projection/back-projection process, each element of the image contains information about what the object really contains at that location, but this information is added to a blurred version of the rest of the object. An exact mathematical correction of this effect can be done by an appropriate pre-filtering of the projections, as in the filtered back-projection algorithm.

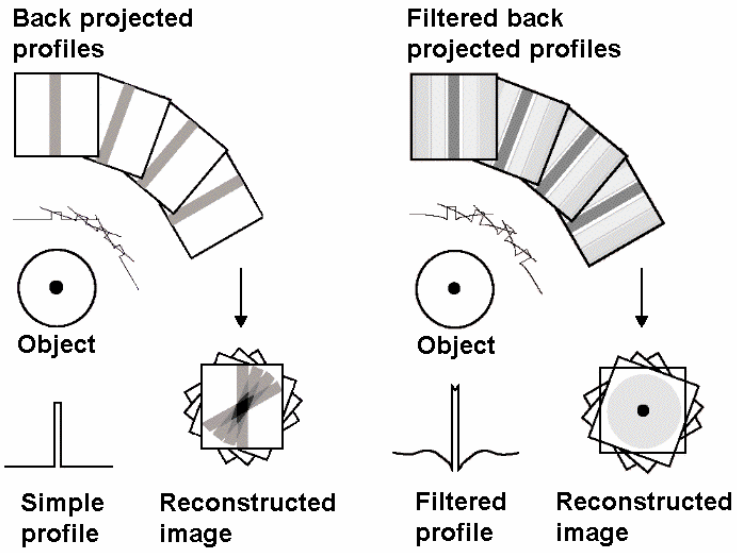

Figure 2.5 – Schematic comparison between the simple back-projection procedure and filtered back-projection. Blurring of the object in the reconstructed image is significantly reduced when an adequate filter is applied to the raw absorption profiles prior to the reconstruction process.

The filtering operation (typically a ramp filter is applied) is performed in the spatial frequency domain and has the effect of creating negative components on the filtered projection which compensate for the contribution of other projections in the subsequent back-projection step. In practice, the filtered data from each angular view are smeared back across the image to be reconstructed. As the number of back-projected profiles increases, the real shape of the investigated object appears increasingly defined. The operation is then repeated for all the slices thus obtaining the final 3D reconstructed dataset.

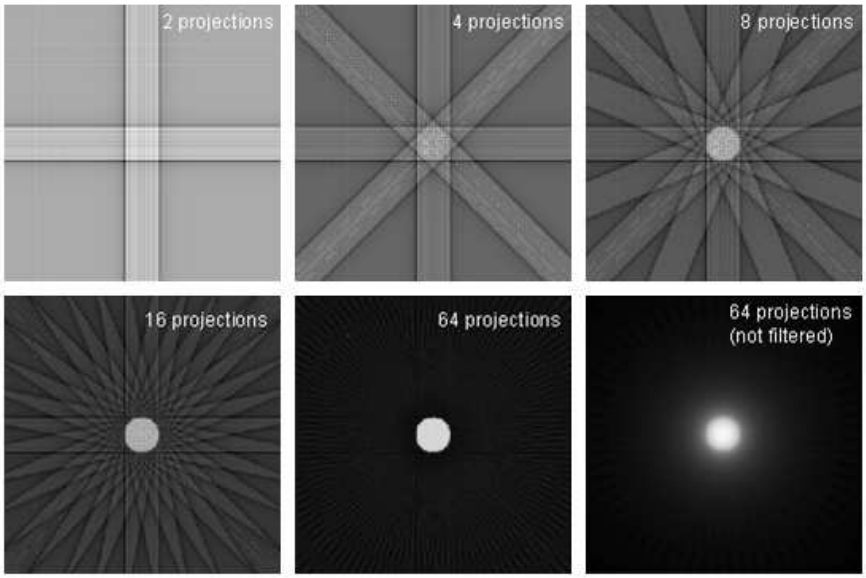

Figure 2.6 – Series of images showing the filtered back-projection process for a single slice of a virtual phantom made of a single, attenuating circular object. The last image, which appears to be highly blurred, shows the same object reconstructed without the preliminary filtering step.

2.6 Projection normalization

Before starting the reconstruction process, all the projections have to be normalized in order to compensate for the non-uniformity of the incoming beam and the sensitivity of the detector, which is typically a CCD. For this purpose, one or more flat-field images are acquired before, during and after the data collection. A flat-field image is simply a radiograph acquired using the same experimental conditions of all the other projections (same energy and exposure time) when the sample is placed out of the field of view of the detector. One or more dark-field images, (i.e. images acquired when the X-ray source is switched off) are also collected. These are employed to compensate for the so-called dark current of the detector and for defects or anomalous responses of some pixels. The dark-

field image (also referred to as offset image) is subtracted to the measured signal as it represents a measure of the current generated within the CCD when no radiation is impinging on it. The dark current effect is common to all CCDs and other photosensitive devices and can be minimized by lowering the operating temperature of the detector, generally using Peltier coolers. The normalization of the acquired projections (Fig. 2.7) is carried out pixel by pixel according to the following formula:

$$IM_{NORM} = \frac{IM_{SAMPLE} - IM_{DARK}}{IM_{FLAT} - IM_{DARK}} \qquad (2.4)$$

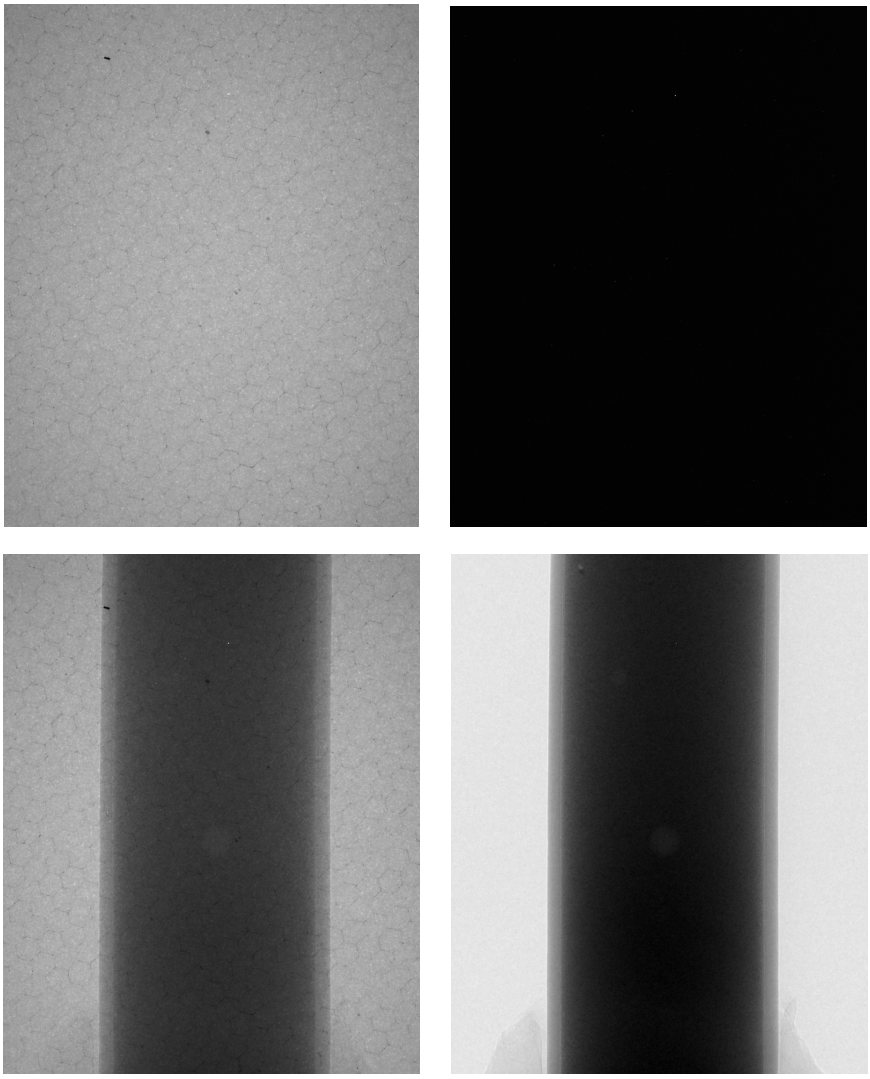

Figure 2.7 - Upper: flat-field (left) and dark-field (right) images employed for radiograph normalization. The honeycomb pattern in the flat-field is generated by the fibre-optic bundle that connects the scintillator screen of the detector to the CCD chip. Lower: The original projection (left) and the final image (right) which has been normalized using the flat and dark fields. The sample is a capillary glass tube (external diameter ~ 3 mm) filled with a cement paste.

2.7 Image artefacts in X-ray micro-tomography

2.7.1 Ring artefacts

The quality of tomographic images are often degraded by the occurrence of several artefacts that may hamper image processing and even prevent the extraction of quantitative information from the reconstructed datasets. One of the most problematic issues is related to the so-called *ring artefacts* which appear as concentric rings superimposed on the reconstructed slices and centred around the rotation axis of the sample. As the true grey values are completely altered by the presence of such features, the image segmentation by simple grey values thresholding may represent a complicated task. Ring artefacts are common in both microfocus and synchrotron-based X-μCT as they are related to the detector and not to the experimental geometry. They are caused by anomalous responses from some elements of the CCD as well as by defects or impurities on the scintillator. By using a flat-field correction (see par. 2.6), i.e. by dividing the acquired projections by a background image, the presence of ring artefacts can be significantly reduced but not completely removed. This is due to the non linear response functions of some pixels of the detector, whose effects cannot be compensated by a simple flat-field correction. Davis & Elliot (1997) suggested a method to compensate for such non uniform behaviour, consisting in wobbling the sample (or the detector) during acquisition in defined horizontal and vertical steps. In this way, the inhomogeneities due to the individual detector pixels are averaged out, leading to an overall reduction of ring artefacts. Alternatively, several image processing algorithms for an effective reduction of ring artefacts (e.g. size and shape filtering or sinogram processing) have been proposed (e.g. Raven, 1998, Sijbers & Postnov, 2004, Boin & Haibel, 2006). In the present work, the filter developed by Brun et al. (2009) starting from the algorithm of Sijbers & Postnov (2004) was successfully employed for ring artefacts correction on tomographic data acquired using the microfocus system in use at the *Tomolab* (see par. 3.1) facility (Trieste, Italy). The method is based on the observation that ring artefacts become straight vertical lines when the input reconstructed images are transformed into polar coordinates, where the centre of the ring artefacts is assumed as the centre of the polar transformation. Within a sliding window, a set of homogeneous rows in the polar image is detected; then an artefact template is generated and used for the correction of the image. At the end of the process, the image is transformed back into cartesian coordinates. An example of ring artefacts correction is

reported in Fig. 2.8; a remarkable improvement in image quality (without any loss of information) can be observed after the filtering process, allowing an easier post-processing of the data.

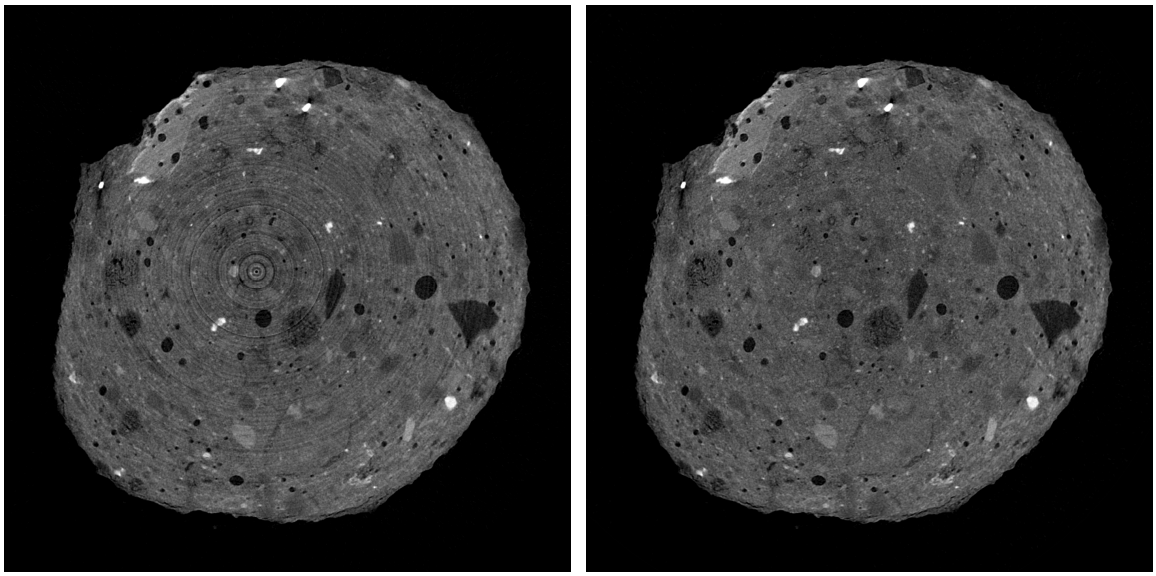

Figure 2.8 - A cross-sectional slice of a cementitious pellet imaged before (left) and after (right) the application of the ring removal filter developed by Brun et al. (2009). Sample diameter: ~ 6 mm.

2.7.2 Beam hardening

The algorithms employed for reconstruction of tomographic data are based on the assumption that the attenuation at a certain position within the sample is independent on the path travelled by X-rays before reaching that position (Haibel, 2008). This is true for monochromatic synchrotron radiation but it is no more valid for polychromatic sources such as common microfocus systems or "white" synchrotron beams. In this latter case, in the beam propagating through the sample, the low energy portion of the spectrum is preferentially attenuated. This phenomenon is commonly referred to as *beam hardening effect* because the X-ray beam becomes "harder" (i.e. its average energy is shifted towards higher values) while it passes through the sample. In the final reconstructed slices, beam hardening is seen as a non-realistic "cupping" of the image, with the inner part of an homogeneous sample appearing to be less attenuating (i.e. showing lower grey values) than the outer region (Fig. 2.9). This of course may hamper an accurate classification of the different materials present in the image because the same material can be represented with different grey values according to its position within the sample.

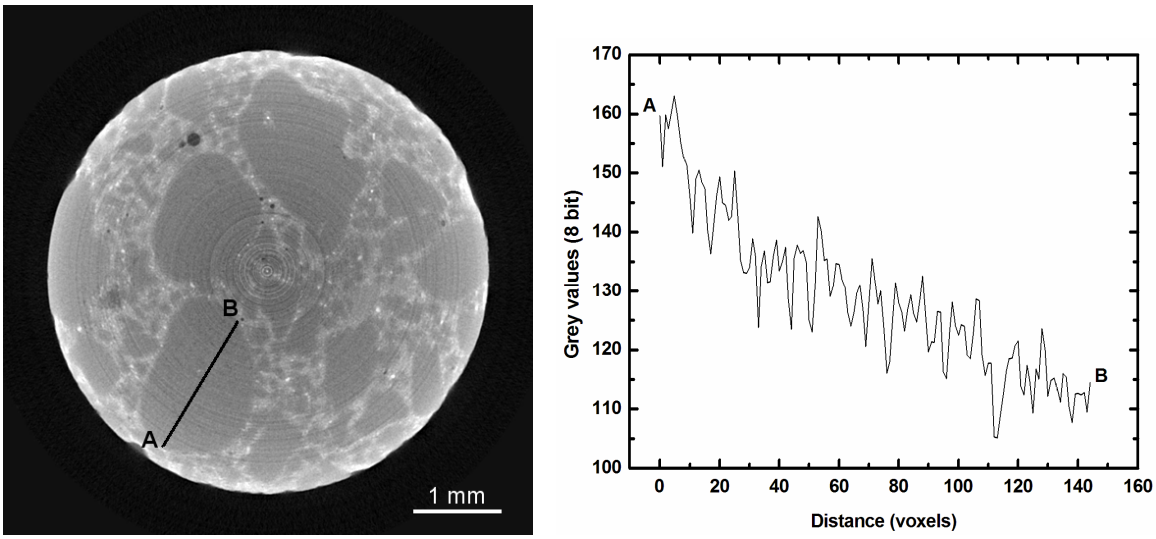

Figure 2.9 - Left: cross sectional slice of a mortar sample constituted by quartz grains in a cement matrix and analyzed using a microfocus (polychromatic) X-μCT system. The inhomogeneous radial distribution of grey values is due to the beam hardening effect. Ring artefacts are also present in the image. Right: plot of the grey values along the A-B radial profile, traced within a quartz grain. In the absence of beam hardening the line would have followed an almost horizontal trend. Fluctuations in the graph are caused by the presence of ring artefacts.

The beam hardening effect may be limited by placing adequate filters (typically an Al or Cu foil) directly in front of the exit window of the X-ray tube, in order to perform a sort of pre-hardening of the radiation. However, this is usually not sufficient to remove it completely and other corrections have to be applied during the reconstruction. This undesired artefact can be compensated by measuring a suitable reference object in order to find a correction function that can be used to virtually transform the radiographs from polychromatic to monochromatic (linearization technique). For beam hardening correction of tomographic data acquired at the Tomolab facility (see par. 3.1), the following polynomial formula was used:

$$S_{out} = a_0 + a_1 S_{in} + a_2 S_{in}^2 + a_3 S_{in}^3 \qquad (2.5)$$

where S_{in} is the signal attenuation value calibrated against air, S_{out} is the output and $a_{0\text{-}3}$ are four coefficients whose values are generally chosen by the user before reconstruction, through a trial and error procedure, until a satisfactory result is obtained. It has to be noted that the signal S is the "log attenuation" value defined according to Beer-Lambert's law as:

$$S = \ln(I_0) - \ln(I) = \mu d \qquad (2.6)$$

where I_0 and I are the measured intensity values without and with the object in the beam, μ is the linear attenuation coefficient and d is the length of the path through the object.

2.7.3 Metal artefacts

When highly absorbing objects within the sample (typically metallic particles) strongly reduce or prevent the transmission of the X-ray beam along its path, the information on other objects in this trajectory can be partially or totally lost. This mechanism leads to the generation of the so-called *metal (or streak) artefacts* which are seen in the reconstructed slices as star- or streak-shaped features. Such artefacts can be attenuated by an adequate filtering (e.g. linear interpolation) of the corresponding sinograms where they appear as bright sinusoidal lines. Alternatively, they can be reduced by increasing the beam energy, even though this necessarily leads to a general loss of contrast.

2.7.4 Motion artefacts

Motion artefacts, which are seen as a general blurring in the reconstructed images, are due to sample movement (e.g. tilting, shaking or shrinking) during data collection or to non exact positioning of the translational motors that may occur when the sample is moved out of the beam for flat-field acquisition during the scan. In this latter case the artefacts appears in the sinograms as small deviation from the ideal sinusoidal profile and can be easily corrected by applying an adequate displacement to the anomalous sinogram lines. On the other hand, when motion is inherent to the investigated sample (e.g. when studying liquids or evolving system as fresh cements) motion artefacts can hardly be corrected.

2.8 Phase contrast tomography

2.8.1 Introduction

Conventional X-ray radiography and tomography normally rely on absorption contrast for the extraction of qualitative and quantitative information. However, absorption is not the only mechanism that contributes to image formation. The refractive index for X-rays is slightly different from unity and an X-ray wave is modulated in its amplitude and phase after passing through a sample. This principle represents the basis of a relatively novel imaging technique known as phase contrast imaging which has become possible after the

great improvement achieved in terms of beam coherence with third generation synchrotron sources. Soon after the development of modern insertion devices, it was noticed that small imperfections in the optics and windows of the beamlines produced significant modulations in the observed intensity (Snigirev et al., 1995), often due to small thickness variations of the windows. Further investigations showed that, in practice, the coherence requirements for phase contrast imaging are very modest and it was demonstrated that phase contrast was possible also with conventional laboratory X-ray sources (Wilkins et al., 1996). The interaction of a wave with matter is described by the complex refractive index *n* of the medium which is usually written using the following complex expression:

$$n = 1 - \delta + i\beta \quad (2.7)$$

The imaginary part is responsible for the mass attenuation coefficient μ of the material, which creates the absorption contrast and is related to the wavelength (λ) by:

$$\mu = (4\pi\beta)/\lambda \quad (2.8)$$

The refractive index decrement δ (~ 10^{-5}, 10^{-6}) is proportional to the electron density in the material and causes a phase shift, which leads to a deviation of the wave front. In the simplest form (propagation-based method), if the incoming wave is approximately a plane wave, interference effects can be observed at certain object-detector distances. Fresnel's theory for diffraction explains the increase in contrast at the edges and interfaces in the object, where the gradient of the phase shift perpendicular to the beam is very high. This additional contrast to the absorption contrast is called phase contrast.

In X-ray radiography and tomography an important distinction has to be made between phase contrast (or visualization) and phase retrieval. In the former, the transmitted X-ray intensity becomes modulated by quantities related to the phase and the resulting images can be used in a qualitative manner to reveal shape information about a sample (i.e. edge detection). On the other hand, with phase retrieval the modulated intensity images are inverted to quantify the phase. Using phase-contrast tomography it is possible to visualize the three-dimensional distribution of some aspects of the phase distribution (i.e. its gradient). In phase retrieval-based tomography the raw phase-contrast data can be used as the starting point for calculations that allows to quantitatively map the complex refractive index of the sample in 3D (Peele & Nugent, 2008).

The methods for phase sensitive imaging can be classified into three major groups of

techniques, each one based on different principles and experimental configurations (Peele & Nugent, 2008) and showing specific advantages and disadvantages:

1- *Interferometry*: in the interferometric techniques, the contrast is due to interference of a wave transmitted through the object with a reference wave, resulting in interference fringes (i.e. Momose, 1995 & Beckmann et al., 1995). Bragg diffraction by perfect crystals slices are used to split, deviate and recombine the two beams. The recorded interference pattern cannot be directly used because the interference fringes cannot be linked to a projection of the object and because an intrinsic fringe pattern is always present (Cloetens et al., 2000). Several images for different external phase shifts must be recorded to reconstruct a single phase map. The main drawback are related to the complexity and the stability requirements of the technique. For instance, the sample must be immersed in a liquid having a similar refraction index in order to avoid large phase jumps and deflections at the air-sample boundaries that would perturb the interference fringes.
2- *Diffraction-enhanced imaging*: these techniques involve optical elements that, in the absence of amplitude modulations are configured so as to reveal the angular deviations of the X-ray beam (which are related to the phase gradients) with high sensitivity. Förster et al. (1980) used a double crystal setup with the first crystal acting as a collimator; the angular deviations introduced by the sample change the incidence angle relative to the second crystal, acting as an angular filter. Diffraction-enhanced techniques are excellent tools for phase contrast imaging (i.e. detection of edges) but are of limited value for phase retrieval. If compared to interferometric techniques, the experimental setup is simplified and can be coupled also with laboratory X-ray sources. An analogous technique in classical optics is called Schlieren imaging.
3- *Propagation-based contrast*: this method is the source of the phase visualization that was firstly observed with third generation synchrotrons and it is probably the most widely used due to the extreme simplicity of the setup (no additional optical elements are required) and the high resolution achievable. The experimental conditions are the same used for conventional absorption X-μCT, except for the higher sample-detector distance. The first intentional use of propagation-based phase contrast tomography was made by Raven et al. (1996) for the reconstruction

of a boron fibre. This technique is based on the spatial redistribution of photons due to deflections (or, more generally, Fresnel diffraction). In this case there is no distinct reference beam as in the interferometric technique and the occurrence of contrast can be explained as due to interference between parts of the wavefront that have suffered slightly different angular deviations associated to different phase gradients (Cloetens et al., 2000). As this is the method that has been used in the present work, it will be described in more detail in the next paragraph.

2.8.2 Propagation-based phase contrast imaging

The high degree of coherence of the X-ray beams produced at third generation synchrotrons is mainly due to the very small angular size of the source and allows to reveal, with great instrumental simplicity the phase variations of hard X-rays (E > 6 keV) by means of the propagation-based method. From an optical point of view, the interference at finite distances between parts of the beam that suffered different phase shifts and are mutually coherent is used to transform the local phase variations into intensity variations (Baruchel et al., 2003). In practice, in order to obtain a phase sensitive image, it is only necessary to place the detector at a distance D from the sample, on the order of 10^{-1} m, whereas a simple absorption image is obtained if D is small, on the order of 10^{-3} m (i.e. with the sample very close to the detector). This corresponds to the fact that the region in the sample that effectively determines the image at a point on the detector, the first Fresnel zone, has a size r_F expressed by:

$$r_F = (\lambda D)^{1/2} \quad (2.9)$$

where λ is the wavelength of the radiation. When D is a few mm, r_F is below the resolution of the detector (typically in the range of μm) and no interference is observed, hence the image is due only to absorption contrast. For larger D, but as long as r_F remains smaller than the size τ of the object or feature to be imaged, the edges of the image behave independently and provide the only phase contribution (Baruchel et al., 2003). For an object or feature with size τ, the best sensitivity is obtained for $D \sim \tau^2/2\lambda$.

The great advantage of this method is its increased sensitivity, provided that the spurious contrast due to inhomogeneities of the beamline components has been eliminated. The observed gain (in particular for light materials or composite materials with similar μ) is mainly due to the fact that in the hard X-rays range $\delta >> \beta$, i.e. the ratio of the effect of the

phase and the amplitude (δ/β) of a transmitted wave is significantly higher (Baruchel et al., 2003). Phase variations across the beam exiting the sample lead to variations in intensity (i.e. contrast), provided that the phase has a two dimensional Laplacian $\nabla^2\varphi(y,z) \neq 0$ (where φ is the phase). For increasing distances D, these variations appear first through a black-white line (see Fig. 2.10) at the phase discontinuities (edge detection), then through a more and more evident system of Fresnel fringes (holography), which progressively evolve towards the Fraunhofer regime (Baruchel et al., 2003).

Under some simplifying assumptions, the following expression for a first qualitative interpretation of the described phenomena may be written:

$$N_D(y,z) = N_0(y,z)[e^{-\int \mu(x,y,z)dx}][1-(\lambda D/2\pi)\nabla^2\varphi(y,z)] \quad (2.10)$$

According to eq. 2.10, the image (i.e. the intensity) at distance D is the product of the absorption image by a phase sensitive term. Inhomogeneities likes pores, cracks or inclusions are associated with abrupt changes of δ (and consequently of φ) where the path of the beam is tangential to an edge of the inhomogeneity. The second derivative will generate black-white contrast at each of these discontinuities.

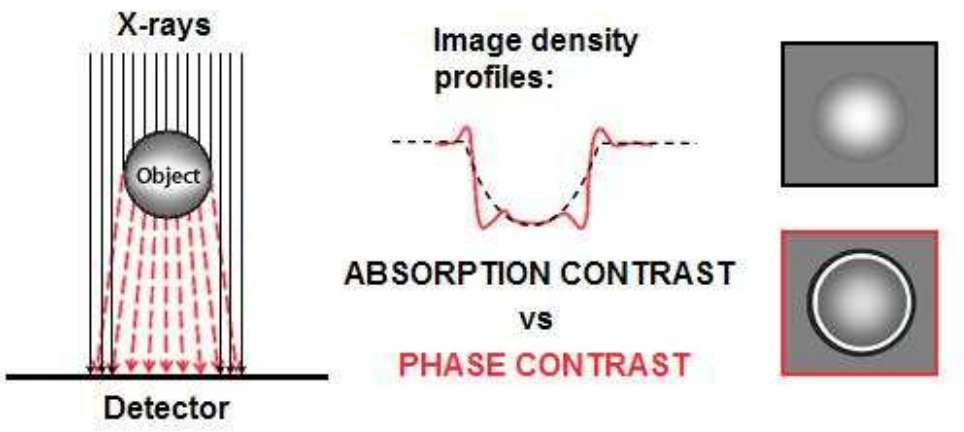

Figure 2.10 - Scheme of propagation-based phase contrast imaging. When X-rays pass through the object, the refractive index decrement (δ) causes a phase shift which leads to a deviation of the wavefronts. As a result of local focusing and defocusing of the deviated X-rays (see red profile), the formation of bright and dark fringes at the interfaces between different materials is observed, especially in the presence of high density gradients (e.g. at the sample/air interface). This effect can be seen only if the sample is placed far from the detector (in the order of cm-dm). In the classical absorption mode (black profile), i.e. when the sample is positioned very close to the detector, the fringes are not observed and the contrast is lower. Image modified from www.konicaminolta.com.

2.8.3 Phase retrieval

It has been shown that, once a set of phase contrast images (projections) is available, the reconstruction procedure based on the same filtered back-projection (FBP) algorithm used for conventional absorption contrast X-μCT provides an acceptable approximation for those distances D where the effect of edge detection is predominant (Cloetens et al., 1997). However, phase imaging based on the visualization of edges is not a quantitative technique and its spatial resolution is limited by the width of the fringes which delineates the discontinuities (Baruchel et al., 2003). For quantitative phase determinations and 3D reconstruction it is necessary to retrieve maps of the phase on 2D images (holographic reconstruction). Cloetens et al. (1999) developed a combined procedure (holotomography) for holographic reconstruction, based on the combination of a few images recorded at different distances for each angular position, which allows to reconstruct 3D quantitative maps of the distribution of the refractive index decrement (i.e. of the electron density) in the sample. The highest accessible spatial frequency is determined by the maximum resolution of the detector (a few μm). Another interesting approach to the problem has been recently proposed by Weitkamp et al. (2010) who developed a computer program (*ANKAphase*) for phase retrieval starting from single-distance phase-contrast projections. The method is based on an algorithm published by Paganin et al. (2002) which is valid if the distance *z* between the object and the detector fulfils the near-field condition:

$$z << d^2 / \lambda \qquad (2.11)$$

where *d* is the characteristic size of the smallest discernible features in the object and λ is the X-ray wavelength used. The intensity distribution in the phase contrast radiographs measured at a single, known distance *z* between the object and the detector plane can then be used to retrieve the projected thickness *t(x, y)* of the object (or, which is equivalent, the projected phase shift of the X-ray wavefront) using the following relation:

$$t(x,y) = -\frac{1}{\mu}\ln\left(F^{-1}\left[\frac{\mu F\left[I(x,y)/I_0(x,y) \right]}{\mu + z\delta\sqrt{u^2+v^2}} \right] \right) \qquad (2.12)$$

where *x* and *y* are the Cartesian coordinates in the image/object plane, *F* and F^{-1} are respectively the forward and backward Fourier transform operators, *I(x,y)* is the intensity distribution in the phase-contrast radiograph, $I_0(x,y)$ is the incident intensity, *u* and *v* are the complex conjugate coordinates of *x* and *y*. An example of application of this method to cementitious samples is reported in par. 4.4.

3- Experimental methods

The X-μCT experiments described in this work were carried out using essentially two different experimental setups which are described in this section. These are the non-commercial laboratory instrument of the *Tomolab* facility and the synchrotron-based system of the *ID-22* beamline at ESRF. The two setups differ greatly in terms of spatial resolution as well as in the quality and flux of the photon beam so that the Tomolab experiments allow medium-high spatial resolution and low time resolution, whereas the ID-22 measurements can be optimized for high time and/or spatial resolution.

3.1 The *Tomolab* facility

The custom-made X-μCT system in use at the *Tomolab* facility in Basovizza (Trieste, Italy) is the result of a collaboration between the Elettra Synchrotron Light Laboratory and the University of Trieste (Dipartimento di Ingegneria Civile e Ambientale and Unità Clinica Operativa di Clinica Odontostomatologica). *Tomolab* is a cone-beam system equipped with a sealed microfocus X-ray tube (*Hamamatsu L9181*) with micrometric focal spot size (Fig. 3.1).

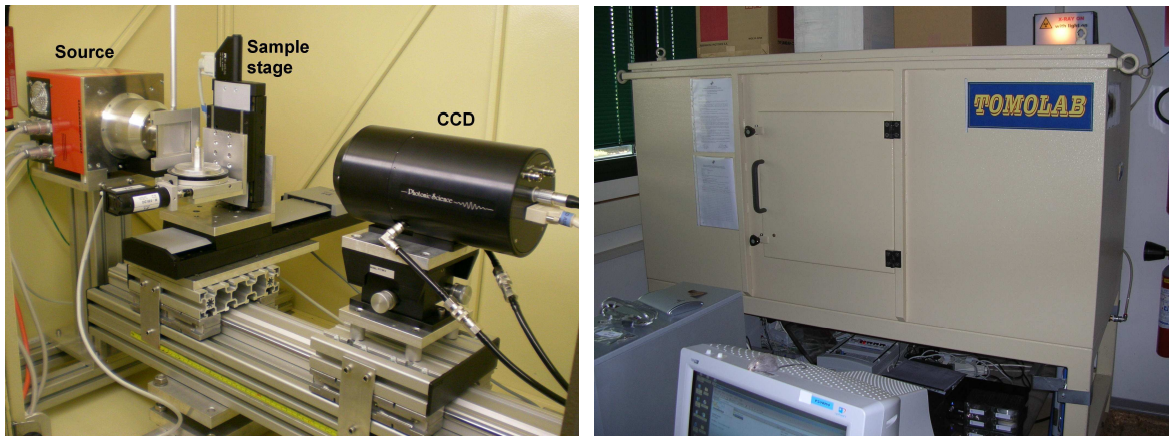

Figure 3.1 - The Tomolab experimental setup (left) and the lead-shielded cabinet (2x1x1 m) containing the whole system (right). A filter made of an Al foil is placed in front of the source in order to limit the beam hardening effect.

The source is air-cooled and can operate at voltages from 40 to 130 kV and currents up to 300 μA, with a maximum output power of 39 W when working in large focal spot mode (40 μm). However, in order to achieve the highest spatial resolution, the focal spot is typically set to its smaller value (5 μm at a maximum power of 8 W). X-rays are produced

by accelerating electrons onto a target (anode) made of tungsten and then exit the tube through a window made of a beryllium foil. The polychromatic spectrum is characterized by the continuous bremsstrahlung radiation (the maximum flux is in the range of 20-85 keV) and is dominated by the strong emission lines of tungsten ($K\alpha_1$ = 59.318 keV, $K\alpha_2$ = 57.982 keV, $K\beta_1$ = 67.244 keV). Aluminium and copper filters with variable thickness (from 0.1 to 1 mm) can be placed in front of the source in order to reduce the beam-hardening effect by attenuating the low-energy part of the spectrum (see par 2.7.2).

X-ray radiographs are collected by a high resolution and high readout CCD detector (*Photonic Science FDI VHR Camera*), characterized by a large field of view (4008 x 2670 pixels) and a small pixel size. A tapered bundle of optical fibres (magnification factor = 1.39) connects the CCD plate to a scintillator screen where a layer of terbium-doped gadolinium oxysulphide (Gd_2O_2S:*Tb*) powder is deposited at a density of 15 mg/cm^2. The resulting active area for acquisition is approximately 50 x 33 mm^2, with a pixel size of 12.5 μm. The scintillator converts X-rays into visible radiation with an emission wavelength (545 nm) that well matches the spectral region of maximum sensitivity of the CCD chip. Typically, the detector operates in 2x2 binning mode, which means that the signal is averaged on four adjacent pixels that work as a single superpixel. In this way, the resolution is of course reduced but the signal to noise ratio can be significantly improved, allowing to reduce the exposure times.

High-precision electrical motors control the movement of the sample by means of two translational stages (along vertical and lateral directions, z and y axes) and a rotating stage (around z axis) with an accuracy of 10^{-3} degrees. The magnification factor can be selected by manually moving the CCD and/or the sample stage along a scaled rail.

In its standard mode the CCD detector produces 12-bit .tif digital images (4096 grayvalues) even though the dynamic range can also be extended to 16-bit. Before the reconstruction process, the acquired projections (including flat and dark field) are converted to 16-bit .raw format images and cropped if necessary. The reconstruction of slices from the acquired 2D projections is carried out using the Feldkamp-Davis-Kress (FDK) algorithm (Feldkamp et al. 1984) for cone-beam geometry implemented in the *Cobra* software package (*Exxim Computing Corporation*). The *Image-Pro Plus* software (*Media Cybernetics, Inc.*) is used to control the CCD camera during image acquisition, where photon accumulation is synchronized with the rotation of the sample.

3.2 The ID-22 beamline at ESRF

The ID22 beamline (Somogyi et al., 2005) at the European Synchrotron Radiation Facility (ESRF) in Grenoble (France) is a multi-technique hard x-ray microprobe focused on X-ray fluorescence, absorption and diffraction on the micrometer scale (*http://www.esrf.eu/UsersAndScience/Experiments/Imaging/ID22/*). The beamline combines a two-undulators source with an achromatic focusing optics. By means of a double-crystal monochromator, this configuration can provide a focused monochromatic beam of about 3.5 x 1.5 μm^2 with a flux up to 10^{12} photons/s between 6.5 and 18 keV.

Besides absorption and phase-contrast micro-tomography, the flexible design of the beamline allows to perform a great variety of experiments, including X-ray fluorescence (XRF), X-ray absorption spectroscopy (XAS), X-ray diffraction (XRD), 3D fluorescence imaging and diffraction tomography (XRF-CT, XRD-CT, see chapter 6).

Projections are acquired using a 14-bit *Fast-Readout Low-Noise (FReLoN) 2000* CCD camera, developed by the Analog Transient Electronics Group (ATEG) in the ESRF Instrument Support Group (Labiche et al., 2007). The camera is equipped with a 2048 x 2048 pixels chip with a pixel size of 14 µm and is cooled by means of a Peltier device. At ID22, the FReLon camera is coupled with a variable magnification optical microscope system that projects light from a scintillator screen onto the CCD chip of the camera.

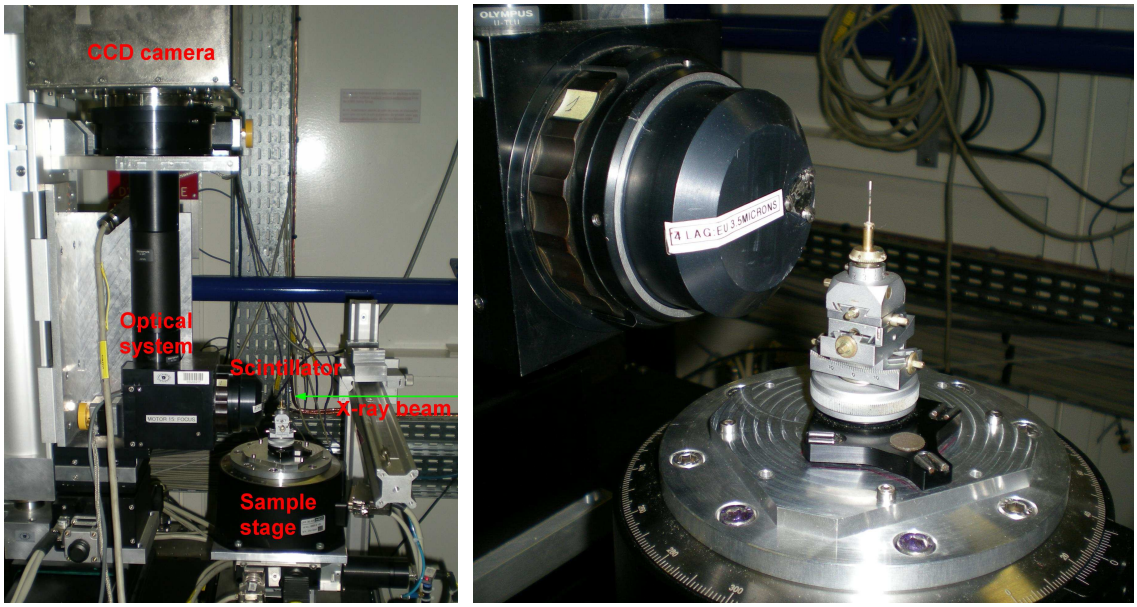

Figure 3.2 - Left: the X-µCT experimental setup (sample stage and detector) in use at the ID22 beamline. Right: a sample mounted on a goniometer head in front of the scintillator window. The sample is a glass capillary tube filled with a cement paste, with a diameter of ~ 500 µm.

The combination of several objectives and eye-pieces allow to reach a maximum magnification factor of 40x, corresponding to a pixel size of 3.5 μm. Various single-crystal scintillators are available that differ in spatial resolution and efficiency. In this particular case the scintillating material is a 3.5 μm-thick film of LAG:Eu (lutetium aluminum garnet, $Lu_3Al_5O_{12}$, doped with europium), with an emission wavelength of 595 nm.

The sample is mounted on a high precision translation and rotation stage by means of an adequate sample holder (e.g. a goniometer head, Fig. 3.2). The sample-detector distance can be adjusted in order to control and exploit the effect of phase-contrast (see par 2.8). The effective source-sample distance is approximately 41 m.

The acquired radiographs are generally saved as 16-bit .edf files and tomographic reconstructions are carried out using the ESRF software package *PyHST* (Mirone et al., 2009), implementing the filtered back-projection algorithm (Kak & Slaney, 1988).

4- Results: synchrotron X-μCT

4.1 Introduction

As the capabilities of X-ray micro-tomography systems in modern synchrotron radiation facilities have improved, it has now become possible to investigate the three-dimensional structure of cement-based materials with a resolution better than 1 μm. Since the beginning of the last decade, synchrotron-based X-μCT has been successfully applied to the study of cement-based materials and other construction materials (e.g. Bentz et al., 2000, Bentz et al., 2002, Helfen et al., 2005, Gallucci et al., 2007, Promentilla et al., 2009) for the extraction of qualitative and quantitative 3D information about pore structure properties, phase evolution, particles shape or other features of interest.

In this chapter, the microstructural evolution of cement paste and mortar samples during the early stages of hydration was studied using synchrotron-based X-μCT. The same region of each sample was scanned at different times from preparation (from ~ 1 hour to ~ 3 days) and then reconstructed in 3D with sub-micrometric spatial resolution. In particular, one of the main goals of these experiments was to investigate how the addition of organic superplasticizers (SP) may affect the behaviour of hydrating cementitious samples during the initial stages, which are known to be the most critical.

4.2 Experimental

4.2.1 Materials and sample preparation

A CEM I 52.5 R (EN 197-1 classification) ordinary Portland cement (OPC) was selected for the preparation of all the samples investigated in this study. The cement included a 5% by mass of Ca-sulphates (gypsum, bassanite, anhydrite) acting as set retarders. The phase composition of the dry cement, determined by means of the Rietveld method on X-ray powder diffraction data is reported in Tab. 4.1. The concentrations of major and trace elements in the same sample were also obtained by means of an X-ray fluorescence analysis (Tab. 4.2). Two cement pastes (samples A and B) were prepared according to different formulations. The first sample was prepared by simply mixing cement and de-ionized water with a water-cement ratio (w/c) of 0.5, while the second included also a PCE superplasticizer in its formulation (see par. 1.5.2 for a general description). The *Dynamon SP1* superplasticizer, produced by Mapei S.p.A., was selected for this study and added to the mix at a dosage of 0.6 % on the total mass. In this second sample, the w/c ratio was

reduced to 0.37 in order to obtain a comparable rheology between samples A and B. This value of w/c was chosen on the basis of mini-slump tests (Kantro, 1980); in practice, at the selected dosage of SP, a w/c of 0.37 allowed to obtain the same spread (i.e. the same initial workability) of a cement paste prepared without SP at w/c = 0.5.

Phase	**Cement notation**	**Weight %**
Alite	C_3S	58.3(4)
Belite	C_2S	19.6(3)
Aluminate	C_3A	7.3(2)
Ferrite	C_4AF	5.6(2)
Periclase	M	1.6(1)
Gypsum	$C\check{S}H_2$	0.5(1)
Hemihydrate	$C\check{S}H_{0.5}$	4.0(2)
Arcanite	K$\check{S}$	1.2(2)
Portlandite	CH	1.7(2)

Table 4.1 - Phase composition of the cement (clinker plus sulphates) selected for this work, determined by means of X-ray powder diffraction. A PANalytical X'Pert PRO MPD diffractometer, equipped with a PIXcel detector and operating in Bragg-Brentano geometry, was used for the analysis.

Major oxides (wt. %)				**Sulphur and trace elements (ppm)**			
CaO	64.65	**TiO_2**	0.30	**S**	23693	**Zn**	214
SiO_2	21.01	**P_2O_5**	0.16	**V**	155	**Rb**	42
Al_2O_3	4.75	**Na_2O**	0.13	**Cr**	92	**Sr**	1101
Fe_2O_3	2.37	**MnO**	0.08	**Co**	7	**Zr**	54
MgO	1.93	**Total**	**96.17**	**Ni**	68	**Ba**	791
K_2O	0.79	***L.O.I.***	*1.66*	**Cu**	175	**Pb**	37

Table 4.2 - Quantitative XRF analysis of the cement employed for the preparation of the samples. The value reported for the concentration of sulphur has to be taken with extreme care due to its volatile behaviour. The analysis was carried out on a fused bead using a Philips PW 2400 sequential WDS spectrometer. L.O.I. = loss on ignition.

In addition, also a mortar sample (sample C) was prepared by mixing cement, de-ionized water and a very fine quartz-feldspar sand, according to a 2:1:1 mass proportion. For this purpose, a CEN standard siliceous sand, conforming to the EN 196-1 norm, was sieved in order to separate the granulometric fraction between 80 and 100 μm. This fraction was then passed through an isodynamic magnetic separator thus obtaining a final product almost entirely constituted of quartz and feldspar grains. Cement powder and de-ionized water (plus additives for sample B and sand for sample C) were mixed by hand for 1 minute and

then manually injected into thin cylindrical glass capillary tubes. The internal diameter of the tubes, made of borosilicate glass in order to minimize X-ray absorption and reduce the acquisition times, ranged from ~ 400 μm to ~ 600 μm with a wall thickness of ~ 20 μm. The tubes were finally sealed with plasticine at both ends in order to prevent the loss of water.

4.2.2 X-μCT setup

The experiments described here were carried out at the European Synchrotron Radiation Facility (ESRF) in Grenoble (France) at the ID-22 beamline (Somogyi et al., 2005). The energy of the incident X-ray beam was set to 14 keV (λ = 0.887 Å) using a double crystal monochromator and the electron beam current in the storage ring was about 200 mA. The selected energy ensured a good balance between penetration and image contrast. Besides a more precise reconstruction of the variations of the linear attenuation coefficient within the sample, the use of a monochromatic radiation allows to avoid the artefacts related to the beam hardening effect (see par. 2.7.2). For each tomographic scan, 1800 projections were acquired in propagation-based phase contrast mode (see section 2.8) with an angular step of 0.1° over a 180° rotation. The sample-detector distance was kept fixed at 24 mm. Data were collected using a high resolution FReLoN CCD camera (Labiche et al., 2007) equipped with a 2048 x 2048 pixel chip. Under the selected conditions (20x effective magnification), the final pixel resolution was ~ 0.7 μm. Small adjustments of the exposure time, which ranged from 0.65 to 0.8 s per projection, were necessary in order to compensate for the different types and sizes of the samples and for the beam current decay with time. The exposure time has to be long enough to ensure an adequate signal to noise ratio but at the same time, an excessive heating of the sample should be avoided. In fact, especially in the very early stages of the hydration process, before the setting of cement has completed, the prolonged interaction between the synchrotron beam and the sample may lead to an evaporation of the mixing water, thus inducing some undesired movements within the fresh paste. As a consequence, strong motion artefacts may appear in the reconstructed images and, in some cases, the data may result completely altered and no longer usable. Moreover, in hydrating cements, as well as in other evolving systems, another critical aspect is related to the total scan duration. In fact, due to the ongoing reactions, the microstructure of the sample may undergo significant and rapid changes while the radiographs are being acquired. This of course does not represent an ideal

situation for an accurate computed reconstruction and may lead to undesired artefacts and, in general, to poor image quality. In this particular case, by using the setup described above, each scan took less than 40 minutes which can be considered an acceptable value for the study of the reactions taking place in hydrating cements.

Three-dimensional stacks of cross-sectional slices (~ 1600 contiguous images, each one 0.7 μm-thick, corresponding to ~ 1.1 mm in height) were reconstructed from projections data using the filtered back-projection algorithm (Kak & Slaney, 1988) for parallel beam geometry implemented in the ESRF software package *PyHST* (Mirone et al., 2009).

4.3 Results and discussion

4.3.1 Image analysis and grey values histograms

The stacking of the reconstructed slices allowed to visualize in 3D the inner structure of the investigated samples (Fig. 4.1). The attention was focused on the temporal evolution of the cement microstructure during the setting and hardening processes. A direct comparison of corresponding slices and volumes imaged at increasing time from preparation allows to obtain an immediate visualization of the transformations occurring within the cement paste that lead to the development of its mechanical strength. These are seen as modifications in the gray values (i.e. the mean attenuation coefficient) of the voxels in the tomographic images, related to the dissolution of the anhydrous clinker phases and the growth of hydration products.

Broadly speaking, among the different crystalline and amorphous phases that constitute cement, clinker phases exhibit the highest values of linear absorption coefficient (μ) while the hydration products are typically less absorbing (table 4.3). In particular, C_4AF shows by far the highest absorption, followed by free lime, C_3S, C_2S and C_3A respectively. For what concerns the hydration phases, the value of μ ranges from a maximum in portlandite (CH) to a minimum in ettringite. The absorption coefficient of C-S-H, the major hydration product, lies between these two end-members but can vary significantly according to its density and to the amount of structural water. Anyway, the discrimination of each single phase remains a difficult task, due to the very small absorption differences between various phases. The difference in μ between air and water is below the resolution of the technique at the adopted energies, hence no distinction can be made between air voids and free water on the basis of their grey values.

Phase	Density (g/cm^3)	Mean Z	LAC (cm^{-1}) at different X-ray energies/wavelengths						
			10 keV 1.241 Å	15 keV 0.828 Å	20 keV 0.621 Å	50 keV 0.248 Å	100 keV 0.124 Å	150 keV 0.083 Å	200 keV 0.062 Å
Ferrite	3.73	16.65	279.37	91.16	40.57	3.35	0.90	0.60	0.50
Lime	3.32	16.58	227.28	72.45	31.81	2.62	0.76	0.53	0.44
Alite	3.21	15.06	177.98	56.51	24.81	2.14	0.68	0.49	0.42
Belite	3.28	14.56	167.96	53.24	23.38	2.05	0.68	0.50	0.43
Aluminate	3.03	14.34	148.23	46.97	20.62	1.83	0.62	0.46	0.39
Anhydrite	2.98	13.42	125.46	39.60	17.38	1.60	0.58	0.44	0.39
Portlandite	2.24	14.30	118.96	37.91	16.68	1.46	0.48	0.35	0.30
$C_{1.7}$-S-$H_{1.8}$	2.60	13.11	108.53	34.37	15.12	1.41	0.52	0.39	0.34
Gypsum	2.32	12.12	79.82	25.19	11.09	1.10	0.44	0.35	0.30
$C_{1.7}$-S-H_4	2.12	12.09	75.05	23.76	10.48	1.03	0.41	0.32	0.28
Monosulph.	1.99	11.66	64.26	20.33	8.98	0.91	0.38	0.30	0.26
Periclase	3.58	10.41	53.90	16.34	7.19	1.01	0.58	0.49	0.44
Quartz	2.65	10.80	50.38	15.36	6.75	0.84	0.45	0.37	0.33
Ettringite	1.70	10.77	45.35	14.33	6.35	0.70	0.32	0.25	0.23
Water	1.00	7.22	5.33	1.68	0.81	0.23	0.17	0.15	0.14
Air	0.001	7.37	0.0062	0.0019	0.0009	0.0003	0.0002	0.0002	0.0001

Table 4.3 – Density, mean atomic number and linear attenuation coefficients at different X-ray energies for the most common phases in cements. Table modified from Promentilla et al. (2008).

Furthermore, as the size of the features to be observed typically approaches the spatial resolution level of the technique, further complications may arise. In this situation, the volume corresponding to a single voxel may be occupied by two or more different phases such as intergrown hydration products and micropores filled with air or water. Hence, the reconstruction process will attribute to these "mixed" voxels a gray value which is proportional to the weighted mean of the attenuation coefficients of the different phases contained in it. In the literature, this is commonly referred to as the partial volume effect. However, for a more accurate identification of phases, other experimental tools are now available, as for example the recently developed diffraction tomography technique (XRD-CT, Bleuet et al., 2008). This latter is a synchrotron-based technique which allows a non-invasive mapping of the distribution of a selected phase within a sample by combining a spatially resolved diffraction signal with the classical tomographic reconstruction principles. Some preliminary results obtained by means of XRD-CT on cement samples are presented in chapter 6.

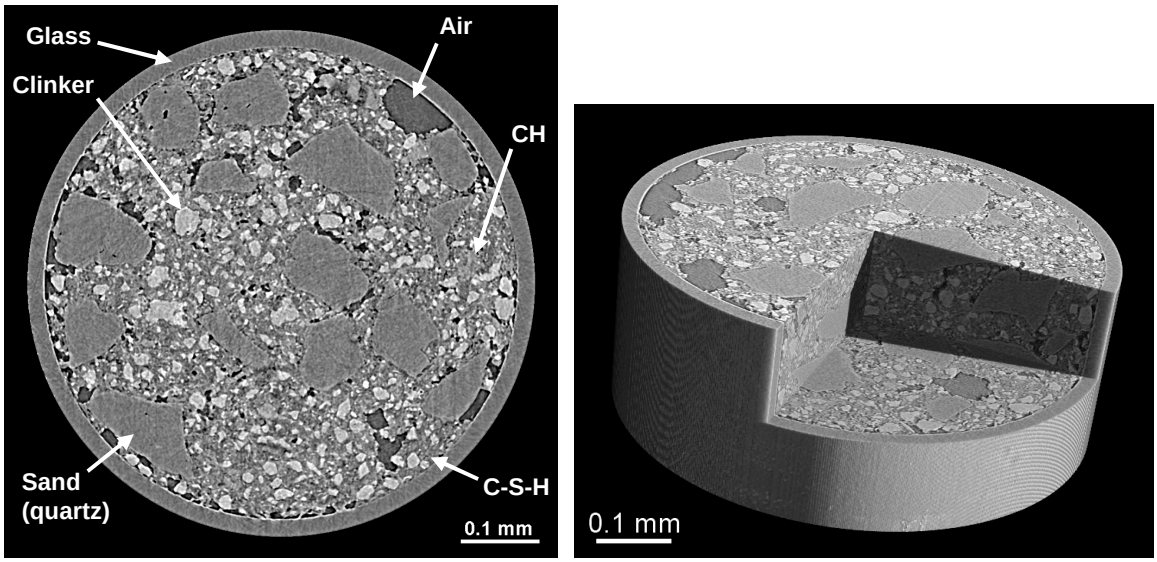

Figure 4.1 – Cross sectional slice and 3D reconstruction of a mortar sample in a glass capillary tube (Sample C). A sector of the 3D dataset was digitally removed in order to visualize the inner structure of the sample. The brightest features represent the unreacted clinker while the darkest ones are pores filled with air or water. The largest particles, showing an intermediate GV are quartz/feldspar grains and can hardly be differentiated from the hydration products (especially C-S-H) present in the cement matrix due to their similar absorption coefficient. Portlandite (CH) exhibits the higher GV among the hydrated phases.

From a qualitative point of view, one of the aspects that can be easily evaluated using X-μCT is the degree of packing of clinker grains. In Fig. 4.2, two cross sectional slices extracted from samples A and B, prepared at different w/c ratios (0.5 and 0.37 respectively) and analyzed approximately at the same hydration time (~ 2.5 h), have been compared. In the sample prepared with a lower w/c, a higher density of clinker particles, as well as a more compact matrix are clearly recognizable. The higher degree of packing of cement particles leads to the development of stronger bonds, thus resulting in the observed general increase of mechanical strengths and overall performances in real applications as w/c decreases. It has to be pointed out that the addition of a superplasticizer to the lower w/c sample allowed to dramatically increase the workability of the paste; otherwise the filling of the capillaries would have been problematic and much air could have been incorporated in the paste.

In order to obtain statistical and quantitative information about the evolution of the hydrating cement system, histograms of the gray values distribution at different hydration times were then calculated for each sample.

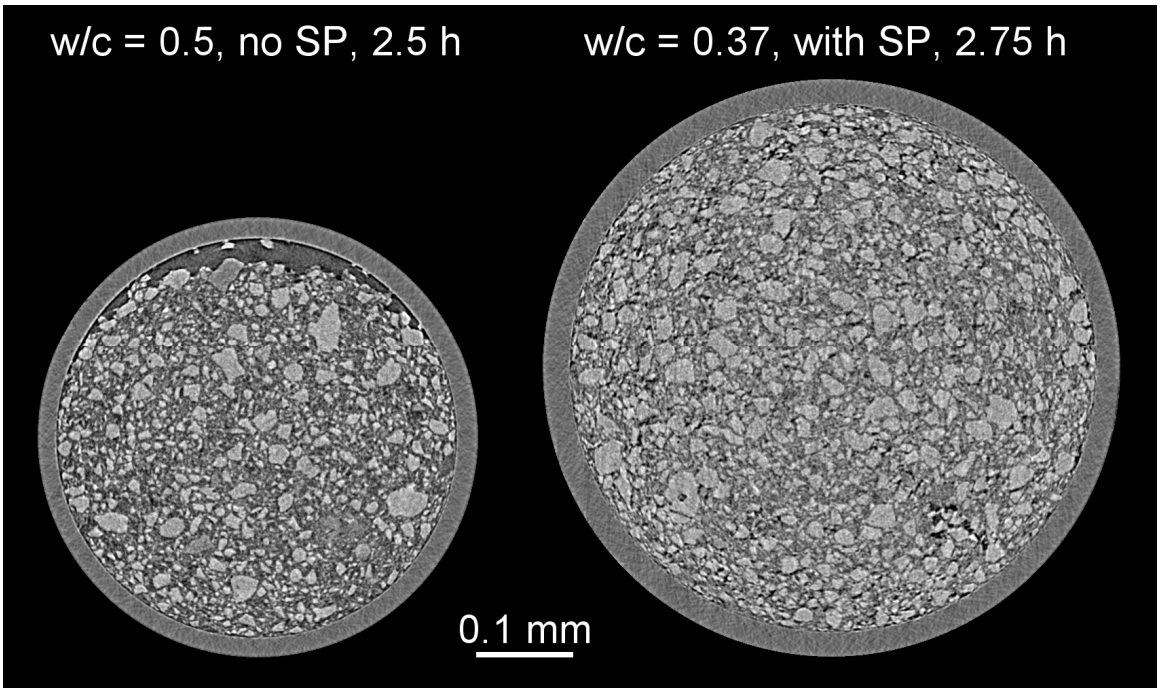

Figure 4.2 - Two reconstructed slices showing the effect of w/c ratio on the packing of clinker grains (brighter particles) in a cement paste. Left: sample A, w/c ratio = 0.5, no SP. Right: sample B, w/c ratio = 0.37, with SP. The two samples were analyzed approximately at the same hydration time, 2.5 and 2.75 hours respectively. Internal diameters of capillaries: ~ 410 μm and ~ 540 μm.

Corresponding volumes of interest (VOIs) were accurately selected at identical positions from each 3D dataset and their histograms were then compared. In particular, cylindrical VOIs, laterally delimited by the inner wall of the glass tubes and extending for 120 slices in height were extracted. The width of the circular selection ranged from ~ 600 to ~ 850 voxels, according to the size of the capillary tube used, resulting in a total number of voxels from ~ $30 \cdot 10^6$ to ~ $70 \cdot 10^6$. The vertical extent of the VOIs was limited to 120 slices in order to restrict the selection to regions characterized by a high homogeneity of the paste. A larger VOI would have included in the selection also portions of the samples affected by large macro-pores and air bubbles caused by the non-perfect filling of the tubes. This problem was particularly evident for the mortar sample whose preparation was complicated by the presence of sand grains. Nevertheless, from a statistical point of view, all the examined VOIs can still be considered sufficiently representative of each 3D stack. Before calculating the grey values histograms, a 3 x 3 x 3 median filter was applied to the selected volumes in order to even out brightness and contrast variations between contiguous slices and reduce image noise. It has to be pointed out that, in order to perform

reliable comparisons between images acquired at different times (i.e. with different scans), each single phase should display always the same mean grey values in all the datasets. For a series of technical reasons (e.g. beam flux decay with time, variations of the maximum and minimum absorption values within the object due to the chemical reactions), this aspect usually cannot be taken for granted. Therefore, the small brightness and contrast variations arising between different datasets have to be corrected prior to the calculation of histograms. For this kind of calibration, regions of interest within reference materials have to be defined and then compared between different scans. In this particular case, the glass of the capillary tubes, sand particles (mainly quartz) and the internal region of the largest clinker grains were chosen as reference materials because they can be assumed to remain unaltered during the entire hydration process. In general, a good correspondence was found between different datasets, thus only small adjustments in brightness and contrast (typically in the order of 1 or 2 GVs in a 8-bit scale) were necessary.

In Fig. 4.3 the evolution of the microstructure of sample A (cement paste, w/c = 0.5) from ~ 2 hours to ~ 3 days is illustrated through slices corresponding to the same virtual section. It may be noticed that the reconstruction plane is not exactly the same for all the datasets. In fact, when switching from one sample to the other, the capillaries had to be manually moved and remounted on the sample holder before each scan, thus introducing potential misalignment and tilting. Anyway, the amount of deviation from perfect co-planarity has been estimated to be less than one degree. The effect of the hydration reactions is seen as a progressive dissolution of the original clinker grains (brighter particles with a maximum size of ~ 70 μm) and the consequent growth of lower density hydration products (intermediate GVs) which fill the pores initially occupied by water (darker GVs). At least two levels of attenuation (i.e. two phases) may be identified within the hydrated portion of the sample. The less absorbing, which is also the most abundant, mostly corresponds to C-S-H and is uniformly distributed around the unreacted clinker particles. A second, higher absorbing phase, is probably portlandite (CH), which typically grows in large and isolated platy crystals. The contrast within clinker grains is not sufficient to clearly recognize the typical texture characterized by C_3S and C_2S grains in a C_3A and C_4AF matrix observed in SEM micrographs (see Fig. 1.1); only some local concentrations of ferrite, corresponding to very bright spots inside the particles can be identified. The edge-enhancement effects due to phase contrast can be recognized in the reconstructed slices but their effect will be discussed in detail in par. 4.4 and 4.5.

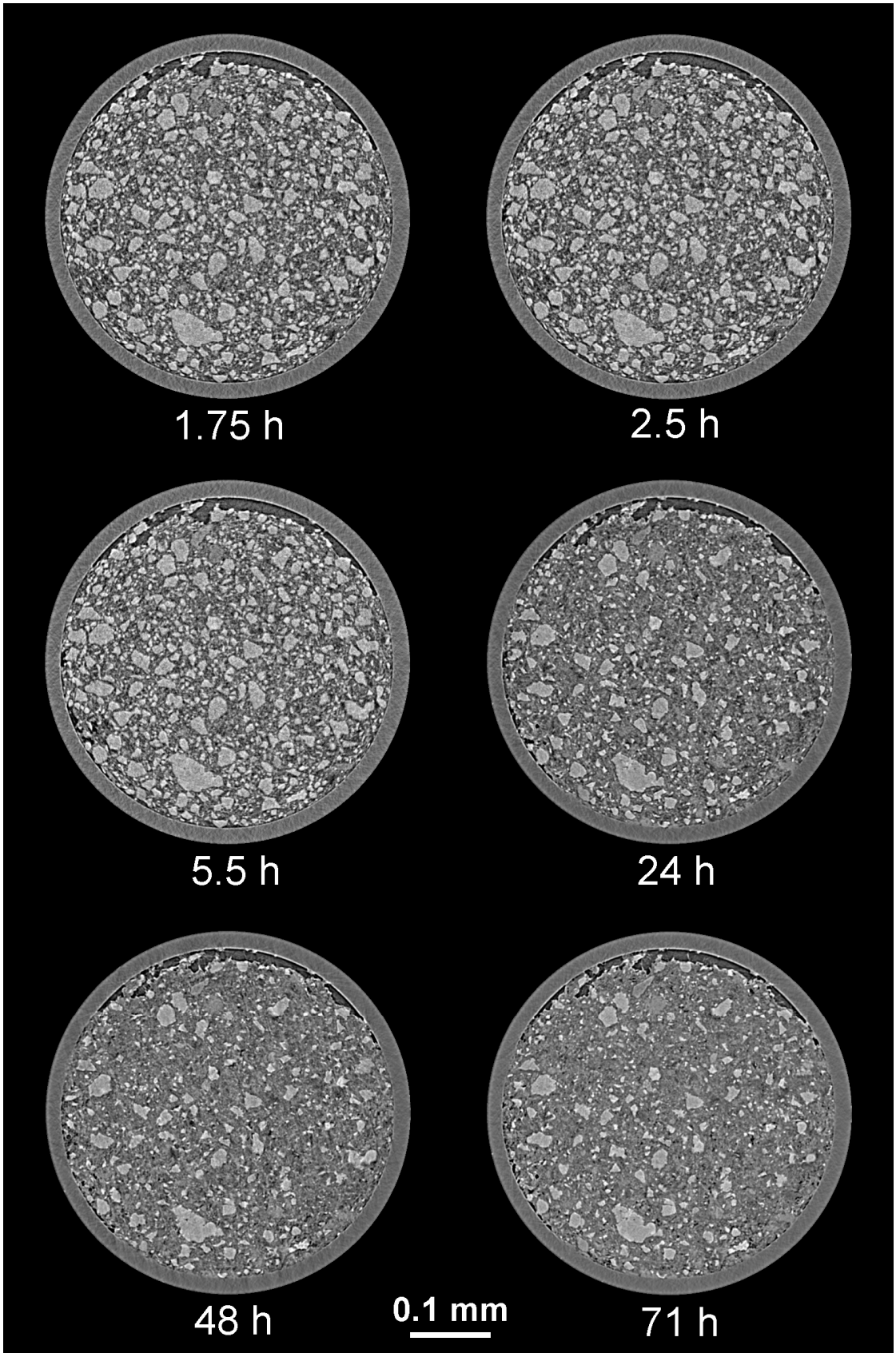

Figure 4.3 - Reconstructed slices (before median filtering) showing the evolution of the microstructure with hydration time in the same cross-sectional plane for sample A (w/c = 0.5).

The same kind of evolution can be seen also from the graph of Fig. 4.4 where the histograms of the grey values distribution within a selected VOI at different hydration times have been reported.

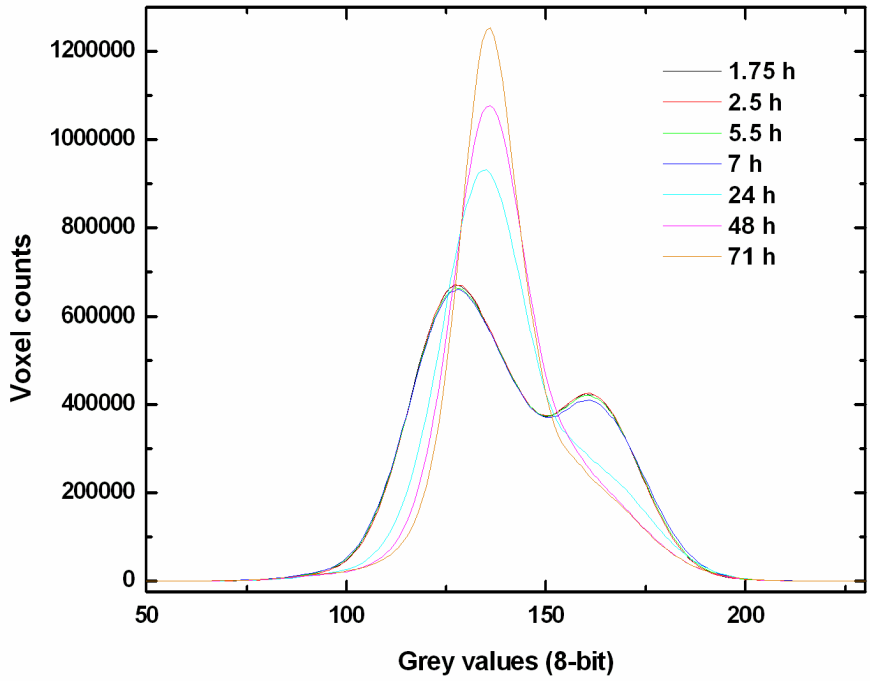

Figure 4.4 - Grey values distribution within a selected VOI at different hydration times for sample A (w/c = 0.5). The selected VOI is a cylinder whose diameter and height are respectively 587 and 120 voxels (voxel size = 0.7 μm). The evolution from a bimodal distribution towards an unimodal one is clearly recognizable. This is an effect of the progressive growth of hydration phases (intermediate GVs) at the expenses of clinker phases (higher GVs) and pores (lower GVs).

In an ideal case (extremely high spatial resolution and no mixed voxels), each phase would be characterized by a well defined grey value and the histogram would be constituted of a number of sharp and isolated vertical lines; however, this is of course not true in practical cases. Since the attenuation values for various phases are close to each other and also due to the effect of mixed voxels, the limits between different peaks are not well defined and significant overlaps occur, especially between pores and initial hydration products which are extremely intermixed. At early hydration times (up to 7 h) the GV curves show a bimodal distribution where the first peak (lower GVs) largely corresponds to air or water-filled pores and early hydration products while the second (higher GVs) has to be mostly attributed to unreacted clinker particles. As the age of the sample increases (24, 48 and 71 h), a significant change in the shape of the histogram is observed. The areas under the

porosity and clinker peaks appear progressively reduced while a third, intermediate peak continuously increases its height and sharpness, leading to an unimodal distribution. This is due to the reaction of the anhydrous cement to give lower density hydration products (mainly C-S-H and CH) which fill the pores. A limited shift of the hydration products peak towards higher values can also be observed between 24 and 48 hours, probably due to an increase of the degree of compactness of the hydrated products. Both in slices and histograms, a major jump in the evolution of the microstructure can be observed between the scans made at 7 and 24 hours, with the development of a considerable amount of hydration products. Following the conventional classification of the hydration stages of cement (see par. 1.4), this can be interpreted as an effect of the increased reaction rate of C_3S, corresponding to the beginning of the so-called acceleration period. This seems to be confirmed by the almost overlapping shape of the histograms from 1.75 to 7 hours which are compatible with the typical behaviour of cement during the induction (or dormant) period that follows the initial stage of rapid dissolution of the first minutes. Although the sequence of reaction is clear and seems to correspond to that investigated in macroscopic systems by calorimetric techniques (Taylor, 1990) it is possible that the kinetics of the reactions is modified by the small size of the samples.

The same procedure described for sample A has been followed also for sample B (w/c = 0.37, with SP), even though a smaller number of scans were performed on this sample, with a maximum hydration time of ~ 2 days. Cross-sectional slices showing the microstructural evolution vs. hydration time are reported in Fig. 4.5 while the variations of the GV distribution are shown in the graph of Fig. 4.6. If compared to the previous sample, fewer transformations can be observed within the microstructure, indicating, in general, a slower evolution trend. This can almost certainly be attributed to a sort of retarding effect caused by the addition of the superplasticizer (see par. 1.5.3). In addition, also the global shape of the GV curves appears to be considerably different of compared to sample A, showing in this case an initial less defined separation (and a lower difference in height) between the two peaks of the bi-modal distribution. This is related to the different w/c ratios of the two samples and in particular to the lower amount of pores and to the higher density of cement particles in sample B, prepared using a lower w/c (see Fig. 4.2). However, the overall evolution trend is the same (though less evident) already observed for sample A, with a progressive increase of the hydration products peak (that also shifts towards higher GVs) at the expense of the unreacted clinker.

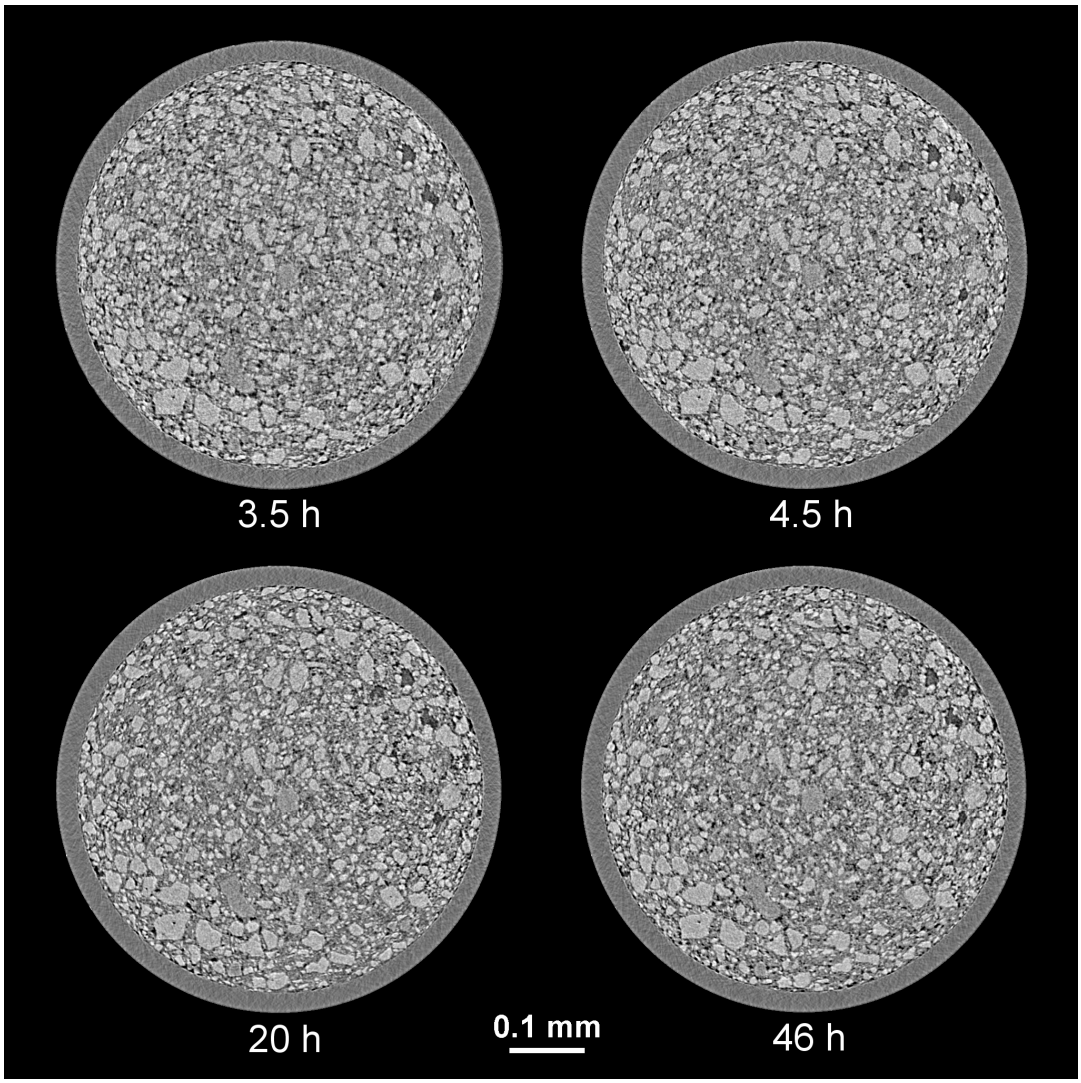

Figure 4.5 - Reconstructed slices showing the internal microstructure of sample B (w/c = 0.37, with SP) at 3.5, 4.5, 20 and 46 hours from preparation. The evolution of the hydration phases appears to be slower if compared to sample A, probably due to a retarding effect induced by the superplasticizer. Internal diameter of the capillary: ~ 540 μm.

4.3.2 Evolution of porosity and anhydrous cement content

In order to obtain a more quantitative interpretation of the results described above, the total porosity and the unreacted cement at different hydration times were also calculated. This was done by applying adequate thresholds to the GV histograms (segmentation) of the filtered datasets (3 x 3 x 3 median). Due to the high degree of overlap between the grey values of different phases, the determination of the correct threshold values is an extremely complicated task and represents the main potential source of error when quantitative analyses have to be carried out on X-μCT data. For this reason, extreme care has to be

taken during the segmentation step in order to avoid misleading interpretations. At the level of resolution achieved, the pore volume and the total anhydrous cement fraction were the easiest classes to separate while it was not possible to accurately discriminate between different hydration products. The volume fractions of anhydrous cement and pores in sample A and B were calculated for each dataset by simply dividing the number of segmented voxels by the total number of voxels included in the chosen volume of interest. The results were then plotted as a function of hydration time as shown in Fig. 4.7.

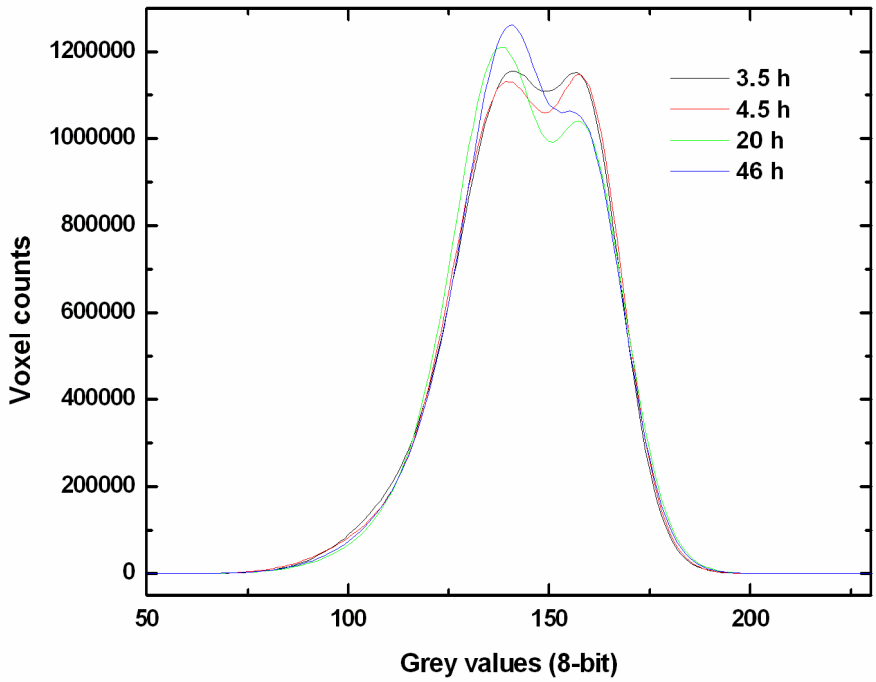

Figure 4.6 – Evolution of the grey values histogram of sample B (w/c = 0.37, with SP) with hydration time. Diameter and height of the selected VOI are respectively 770 and 120 voxels. A different shape of the curves is observed if compared to sample A, probably due to the higher degree of packing of particles at lower w/c. The overall slower evolution of the curves may be attributed to the retarding effect of the superplasticizer.

The evolution of the microstructure can be monitored also by means of direct 3D visualization as shown in Fig. 4.8. The unhydrated clinker fraction in a cement paste sample has been segmented from a selected VOI of 70 x 70 x 70 μm^3 on the basis of its grey values and then visualized by setting the remaining parts of the sample (pores and hydration products) to transparent. By repeating the same operation on datasets acquired at different ages, a progressive reduction in the size of cement particles can be observed as a consequence of their continuous reaction with water to give hydration products.

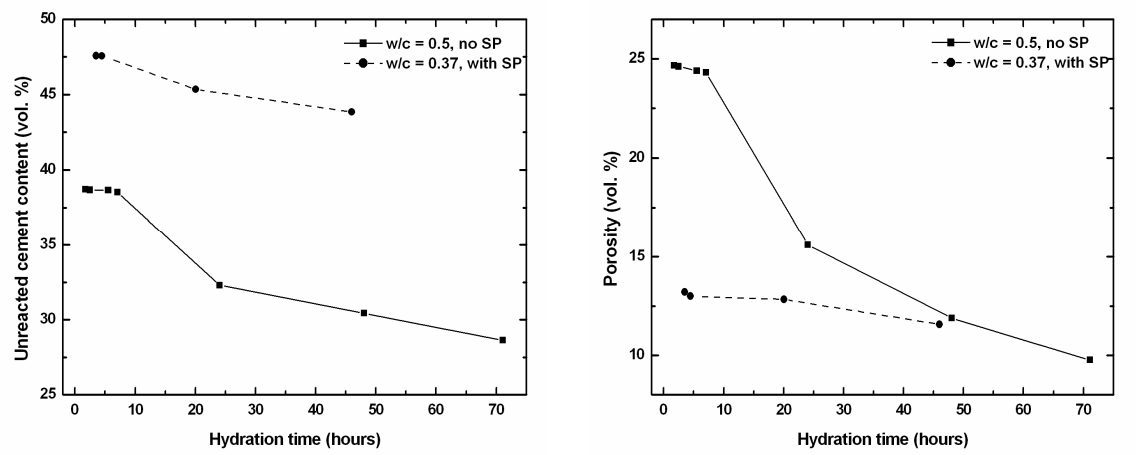

Figure 4.7 – Temporal evolution of the unreacted cement content (left) and pores (right) in sample A (solid line-squares) and B (dashed line-circles). Due to the lower amount of water, a reduced initial porosity and a larger fraction of unreacted cement are observed in sample B. Moreover, the different evolution rates of the two samples can be interpreted as due to the retarding effect of the superplasticizer.

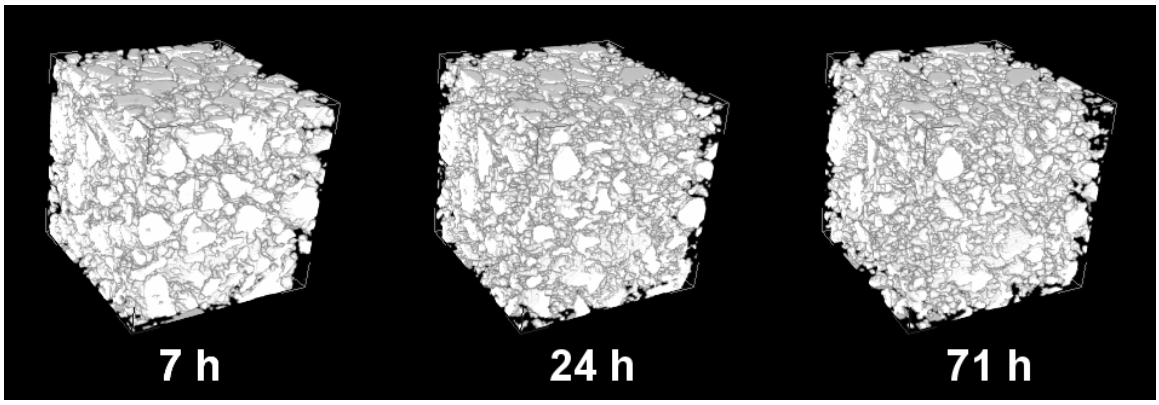

Figure 4.8 – 3D representation showing the evolution of the unreacted cement fraction with time in a VOI of 100x100x100 voxels (70x70x70 μm) for sample A. As a result of hydration reactions, smaller clinker particles are rapidly consumed and larger grains significantly reduce their size.

4.4 Effects of phase contrast on reconstructed images

It has to be pointed out that, due to the particular experimental configuration adopted, the grey values that are seen in the reconstructed slices are not only a function of the absorption contrast between different materials but also depend on the effect of phase contrast which is related to the sample-detector distance. As discussed in par. 2.8, phase contrast imaging, if compared with classic absorption imaging, represents an excellent tool for the visualization of tiny microstructural details within a sample due to its edge-

enhancement capabilities. Nonetheless, when precise quantitative analyses and segmentations have to be performed, the effect of phase contrast in tomographic images may lead to undesired artefacts and erroneous interpretations. As described in par. 2.8.2, propagation-based phase contrast is related to the deviations of the propagating X-ray wavefronts in response to the phase shifts generated by the refractive index decrement (δ) of different materials. In radiographs and reconstructed images, this leads to the formation of two bright/dark fringes at the interfaces between different substances, especially where the density gradient is very high. As a result, all the edges appear significantly enhanced, with positive effects on the visualization of features. This is particularly evident in the slices of Fig. 4.3 at the interface between the inner capillary wall and a large macro-pore where a bright line is clearly recognizable but can be observed also at the edges around clinker grains and hydration products. In practice, as a consequence of the local alteration of the attenuation values at the interfaces, the grey values distribution of an image may undergo relevant modifications thus making segmentation a very complicated task. However, as shown in par 2.8.3, phase retrieval methods (e.g. Cloetens et al., 1999, Weitkamp et al., 2010) allow to overcome these limitations by reconstructing quantitative maps of the distribution of the refractive index decrement δ (i.e. of the electron density) within a sample, starting from projections acquired in phase contrast mode. In this way, detailed information about density variations can be obtained allowing a more accurate classification of different materials if compared to pure absorption X-μCT (i.e. with the sample placed very close to the detector). In the next paragraph, an example of application of the phase retrieval algorithm developed by Weitkamp et al. (2010) to phase contrast tomographic data of cementitious samples is reported.

4.5 Reconstruction using phase retrieval

The *ANKAphase* software (Weitkamp et al. 2010, see par. xx) for single-distance phase retrieval has been tested here on X-μCT data acquired at the ID-22 beamline during a second experimental session. *ANKAphase* is a software that processes X-ray inline phase-contrast radiographs and reconstructs the projected thickness of the objects imaged in the radiographs following an algorithm proposed by Paganin et al. (2002). The program is designed to be used with sets of radiographs recorded for X-μCT although it does not perform tomographic reconstruction itself. This latter is carried out using the software package *PyHST* in use at ESRF (Mirone et al. 2009).

A phase contrast X-μCT scan was performed on a mature cementitious test sample, consisting in a simplified system constituted by a model mix of C_3S, C_3A and gypsum. The sample was analyzed only at 7 days from hydration, hence the temporal evolution was not investigated in this case. For this measurement, small changes were made to the experimental setup previously described in par. 4.2.2. An energy of 17 keV (λ = 0.730 Å) was selected, with the storage ring current being fixed at 200 mA. 1800 phase-contrast projections per scan were acquired using an angular step of 0.1° and an exposure time of 0.6 s; the sample-detector distance was set to 8 mm. The FReLoN CCD camera was coupled with a 40x optical system, thus pushing the nominal pixel resolution to 0.35 μm. In the reconstructed images, this resulted in an excellent visualization of the microstructural features of cement.

Fig. 4.9 shows the appearance of one of the acquired radiographic projection before and after the phase retrieval procedure. The edge-enhancement effect of phase contrast is clearly recognizable throughout the radiograph on the left (see enlargement), especially at the inner and outer walls of the glass capillary, in the form of black and white fringes. Even though the processed image (right) is apparently less contrasted and blurred, with not well defined edges, a lot of information about the variations of δ is contained in it.

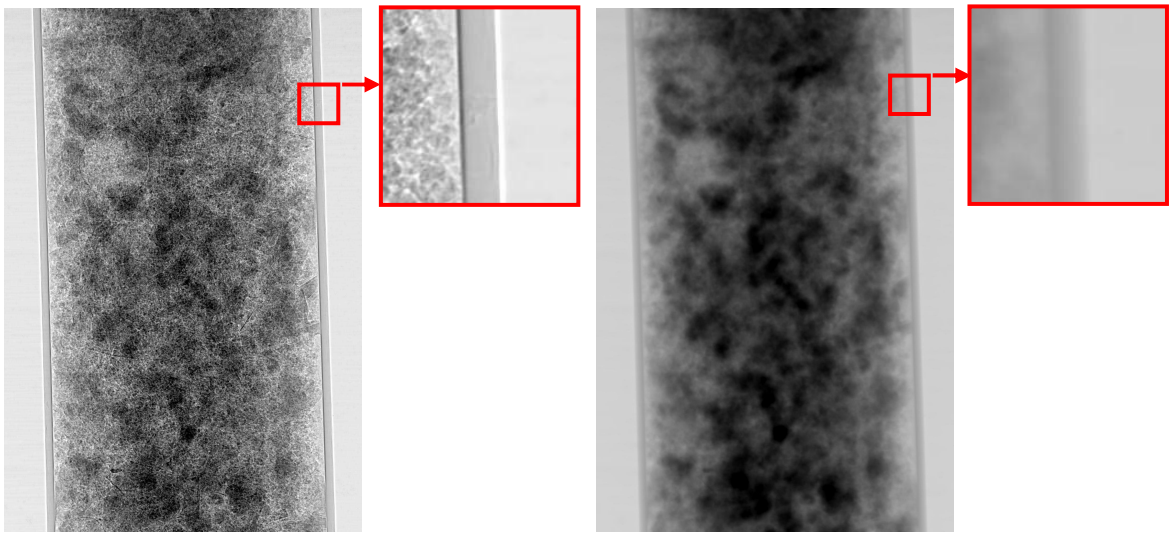

Figure 4.9 – Comparison between a normalized radiographic projection acquired in phase-contrast mode and the same image after having been processed with the *ANKAphase* software (Weitkamp et al. 2010) for phase retrieval. Even though a loss of detail is observed in the second image, the dark and bright fringes due to phase contrast have been significantly attenuated. The internal diameter of the capillary is ~ 650 μm.

Tomographic reconstructions were carried out for both sets of radiographs, obtaining the results reported in Fig. 4.10.

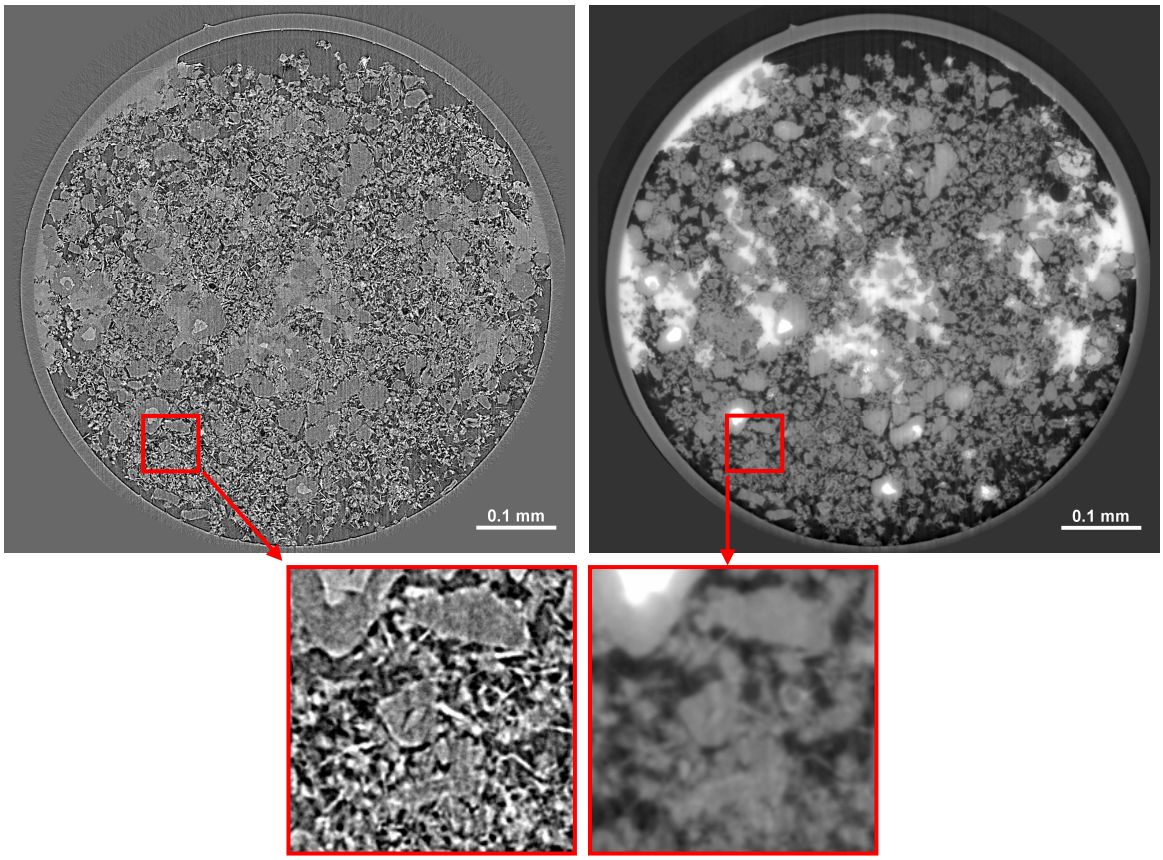

Figure 4.10 – Sample: hydrated mix of C_3S + C_3A + gypsum at 7 days of hydration. A slice reconstructed in the conventional way (left) is compared with the same image reconstructed after having processed all the radiographs using the *ANKAphase* software for phase retrieval.

The image reconstructed from conventional phase contrast projections shows an excellent level of detail. The high content of macropores, especially close to the capillary walls is due to an inhomogeneous filling of the capillary. In addition, a high degree of hydration is observed, as clinker particles seem to have almost completely reacted to give hydration products (mainly C-S-H). Large portlandite crystals (whose GV is comprised between those of clinker and C-S-H) are also clearly recognizable. In the top left corner of the relative enlargement, the remnants of a clinker particle surrounded by a thick rim of hydration products can be observed. Furthermore it is interesting to focus the attention on the abundant needle-like crystals which probably correspond to fibrous (or lamellar) C-S-H. Such elongated crystals show anomalously large attenuation for an hydration product. Again, this has to be interpreted as due to the effect of phase contrast. In practice, due to

their high aspect ratio, C-S-H crystals result completely occupied by bright phase contrast fringes. It is clear that, when a GV segmentation is carried out under these conditions, such crystals are erroneously interpreted as highly absorbing materials while their density is actually quite low. By simply thresholding the histogram of this slice, it is easy to demonstrate that a large fraction of C-S-H needle-like crystals exhibit the highest GVs in the image, even above those of clinker, which should be by far the most absorbing material in this kind of samples. On the other hand, the image reconstructed using the radiographs processed for phase retrieval shows a very homogeneous distribution of GVs within each particle and the effects of phase contrast are no more observed. As a consequence, a lower level of detail is achieved with this kind of visualization (though small needle-like crystals are still recognizable) but the various materials are more easily identified. The resulting grey values are a function of the variations of the refractive index decrement (δ) within the sample, which is related to the electron density. Unreacted clinker remnants show the maximum GV (white), followed by portlandite crystals, which also appear very bright. The remaining part of the hydrated paste (mainly C-S-H) exhibit an almost uniform grey values and can be clearly differentiated from porosity, which is practically black. This can be seen also from the distribution of grey values in the two slices, as reported in Fig. 4.11. In the histogram of the image reconstructed after phase retrieval (right) a sharp peak at low GVs, corresponding to voxels occupied by porosity can clearly be distinguished. Moreover, at higher GVs the contributions of unreacted clinker and CH are more easily identified. On the other hand in the conventional slice, the choice of adequate thresholds for the classification of different materials represents a problematic issue due to marked overlaps in the histograms, ultimately caused by the anomalous GVs measured at the interfaces between small crystals and air and to partial volume effects (par. 4.3.1).

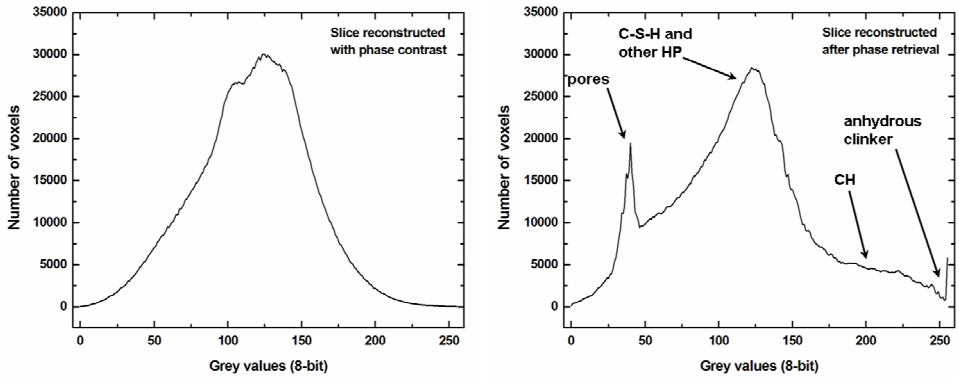

Figure 4.11 - GVs histogram of the two slices shown in Fig. 4.10 (only the circular region within the inner capillary wall was included in the calculations).

5- Results: microfocus X-μCT

In the previous chapter some of the capabilities of synchrotron X-ray computed tomography for the study of cementitious samples were demonstrated. The inner 3D microstructure of hydrating cement samples was investigated at sub-micrometric spatial resolution, providing cross-sectional slices showing an image quality not far from that achievable with SEM imaging on polished surfaces. Although conventional laboratory X-μCT instruments provide a spatial resolution which is approximately one order of magnitude lower than synchrotron-based systems, they can be successfully used for the study of several larger scale features of interest in cementitious materials. In this chapter, some results of X-μCT experiments carried out using the microfocus system in use at the *Tomolab* facility (see par. 3.1) are presented. A series of measurements was carried out on cement pastes with different w/c ratios in order to test the suitability of microfocus X-μCT for the study of subtle variations in the microstructure of cements. In addition, other experiments were carried out on cement pastes and mortar samples with the aim of extracting quantitative information about the pore size distribution.

5.1 Study of cement pastes with different w/c

5.1.1 Sample preparation and experimental setup

A CEM I 52.5 R (EN 197-1 classification) ordinary Portland cement (OPC) was used for the preparation of three cement pastes characterized water to cement ratios of 0.35, 0.5 and 0.65 respectively; no admixtures were included in the formulations. For each specimen, a cement powder (including a 5 % by mass of Ca-sulphates) was mixed with de-ionized water by means of an automatic mixer for one minute. Soon after mixing, the obtained fresh pastes were injected by hand into cylindrical glass tubes with an internal diameter of ~ 2.5 mm. The tubes were then sealed with plasticine in order to prevent the loss of water. Tomographic scans were carried out on each sample at 24 hours, 7 days and 28 days of hydration using the microfocus X-μCT system in use at the Tomolab facility (see par. 3.1 for details). All the experimental parameters were kept constant throughout the whole series of experiment in order to ensure a higher level of uniformity between different scans. The small variations of the glass tube diameter, in the order of ~ 10-20 μm, were considered negligible. The X-ray source operated at an accelerating voltage of 80 kV and a current intensity of 100 μA, with a focal spot size of ~ 5 μm. A total number of 1440

projections per scan were acquired over a 360° rotation (angular step = 0.25°) with an exposure time of 6 s. Under these conditions, each X-μCT scan took approximately 2.5 hours which can be considered an acceptable duration at the selected ages of hydration (1, 7 and 28 days). The source-object and source-detector distances were set respectively to 80 and 40 mm, thus obtaining a magnification factor M equal to 5. Considering that, in order to improve the signal to noise ratio, the detector operated in 2 x 2 binning mode, the effective pixel resolution on the acquired radiographs was ~ 5 μm. A 0.5 μm-thick Al foil was placed in front of the source exit window in order to attenuate beam hardening by filtering the lower energy portion of the polychromatic X-ray spectrum. As the effects of beam hardening in the reconstructed images were very limited, the polynomial correction described in par. 2.7.2 was not applied in order to avoid non-uniform alterations of the grey values between different reconstructed datasets. Tomographic reconstructions were performed using the *Exxim Cobra* software in use at Tomolab and a ring artefacts correction was successfully performed on the slices using the ring removal algorithm (see par. 2.7.1) developed by Brun et al. (2009).

5.1.2 Results

The effects of water-cement ratio on the microstructure of cement paste samples were investigated starting from the analysis of 2D projection data. Absorption profiles of the different samples (Fig. 5.1) were measured on radiographs normalized according to the standard flat field and dark field correction described in par. 2.6. As shown in Fig. 5.1 for the samples at 7 days of hydration, the absorption of X-rays decreases with increasing w/c as a consequence of the higher amount of water and the overall lower density of the sample. Despite its slightly larger diameter, the sample prepared with w/c = 0.65 shows the lower X-ray attenuation. Such variations in the density of the cement paste are expected to produce significant microstructural changes which can be detected in the reconstructed images. For this reason, volumes of interest were selected from the 3D datasets of samples prepared with different w/c ratios and then compared to each other. For this purpose, the first step consists in bringing all the datasets at the same levels of brightness and contrast, otherwise no reliable comparisons would be possible. In practice, the same material should exhibit the same level of attenuation (i.e. the same mean grey value) throughout all the images to be compared. This was done by selecting regions of interests within known materials (in this case the glass of the tube and the unreacted cement fraction) and

calculating their GV histograms thus assigning to each material its mean grey value. The procedure is repeated for each sample, then, by means of simple calculations, the histogram of each dataset is adequately shifted and/or stretched until each reference material corresponds exactly to the same mean grey value in all the reconstructed volumes.

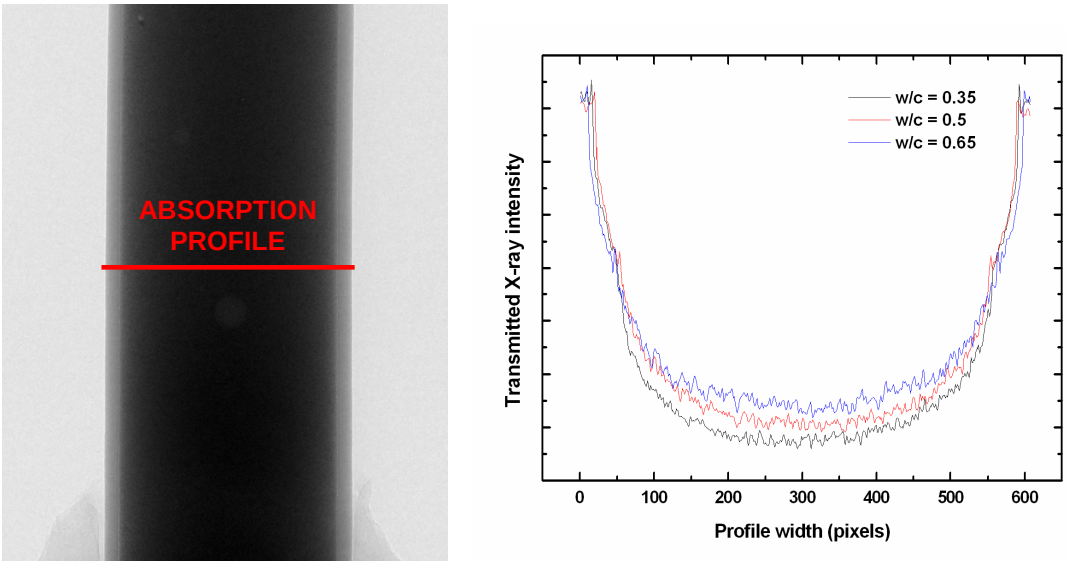

Figure 5.1 - X-ray transmission (absorption) profiles measured on normalized radiographs of three cement pastes prepared at different w/c ratios. Samples are contained within cylindrical glass tubes with an internal diameter of ~ 2.5 mm. An increase in w/c is reflected in a lower X-ray attenuation of the sample, as a consequence of the larger amount of water included in the mix. The plot refers to three cement samples scanned at 7 days of hydration; however, the trends at 1 and 28 days are nearly identical.

Due to the high homogeneity of the paste within the tubes, with very few entrained air bubbles, it was quite easy to select, within each sample, suitable volumes of interest for the calculation of the grey values distribution. The results of a comparison carried out between three cement pastes with w/c of 0.35, 0.5 and 0.65 (at 24 h of hydration) are illustrated in Fig. 5.2 by means of both cross sectional slices and grey values histograms. Remarkable differences can be observed between the microstructures of the three different samples, despite the limited spatial resolution of the images if compared to synchrotron X-μCT. The first aspect that can be noticed is a general decrease of the overall brightness (i.e. attenuation) of the paste with increasing water content, as a result of density variations and in accordance with the results obtained from the radiographs (it may be useful to remember here that the grey scale adopted in the radiographs is traditionally inverted if compared to

slices). The overall darker appearance of the slice referring to a w/c of 0.35 is the result of a less dense microstructure, characterized by a lower degree of packing of cement particles and a higher porosity.

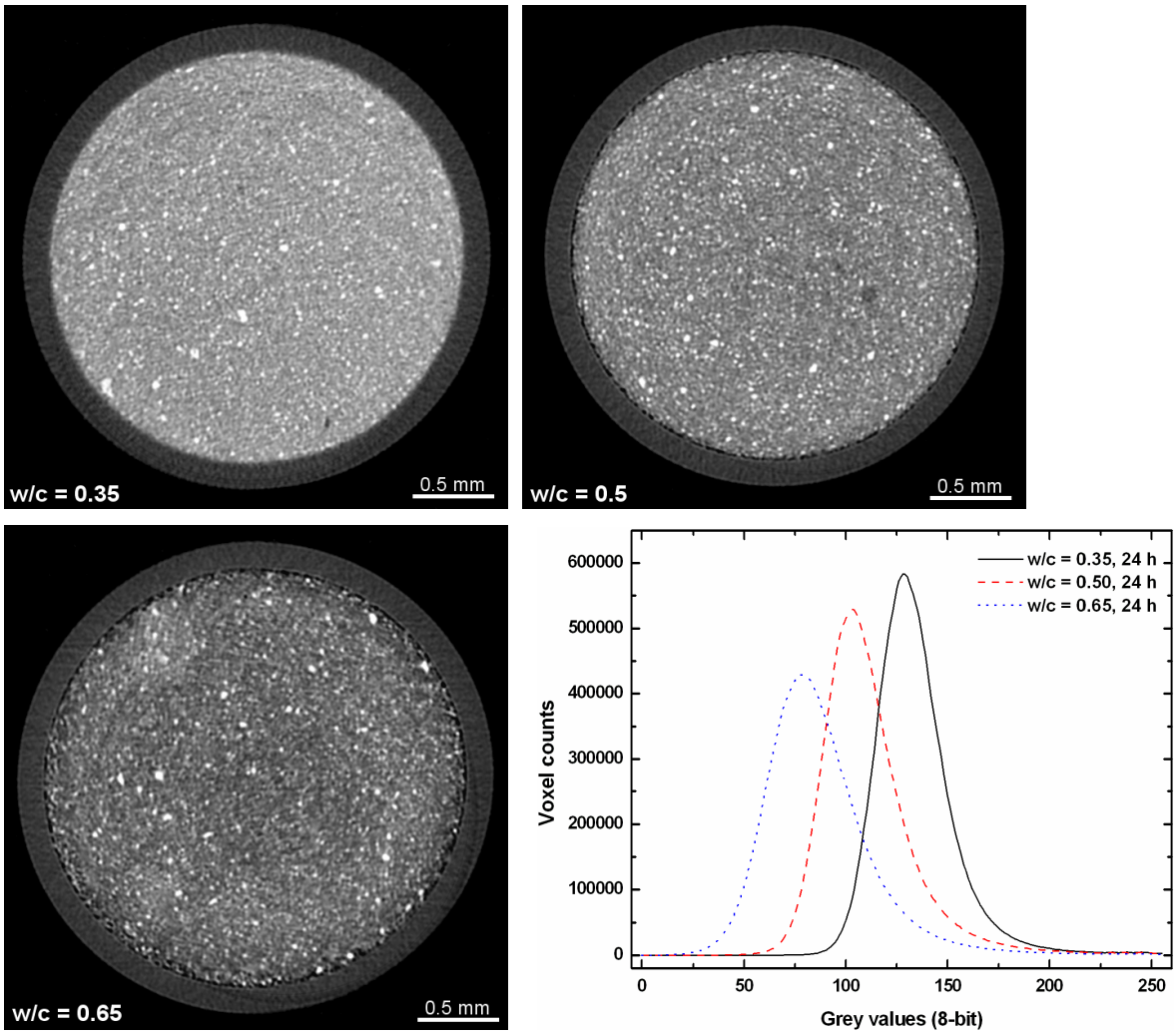

Figure 5.2 – Effect of w/c ratio on the microstructure of cement pastes, illustrated by means of cross sectional slices and grey values histograms. The voxel size in the reconstructed images is ~ 5 μm. Grey values distribution histograms were calculated over cylindrical VOIs selected within the cement paste with a diameter of 490 voxels (2.45 mm) and a thickness of 120 slices (0.6 mm), characterized by high homogeneity and absence of large macropores. A different overall attenuation (i.e. density) as a function of w/c can be clearly recognized.

However, as it can be seen from the GV histograms of the selected VOIs, the contribution of different phases (pores, clinker, hydration products) are not easily separated from each other and a single broad peak is observed as a result of partial volume effects (i.e. the presence of “mixed pixels”). For this reason, the segmentation of pores or unreacted

cement on the basis of their GV is not a straightforward task. For instance, the contribution of the largest unreacted clinker particle is concentrated in the right tail of the GV distribution but smaller ones are highly intermixed with micropores and hydration products thus resulting in intermediate grey values. Nonetheless, the shift of the distribution towards lower values as w/c increases represents a direct evidence of the progressively lower compactness of the microstructure which is the ultimate cause of the lower mechanical strengths typically measured for samples with higher w/c ratios.

Another aspect that can be easily visualized from reconstructed slices is the drying shrinkage which is related to moisture loss from the cement. The amount of shrinkage in cement and concrete is related to external factors such as temperature and relative humidity but depends also on internal factors related to the formulation (w/c ratio, type of cement, use of admixtures) and on the total surface exposed to air. The first water to be lost is that held in the large capillary pores. The loss of this water does not cause significant volume change. However, as the drying process continues, loss of water from small capillary pores and later from gel pores takes place. With the reduction in the vapour pressure in the capillary pores, tensile stress in the residual water increases. Tensile stresses in the capillary water are balanced by compressive stresses in the surrounding cement and as a result the concrete shrinks.

In the reconstructed slices of Fig. 5.2 the effect of shrinkage and its dependency on w/c ratio are clearly recognizable. With increasing water content, the development of an increasingly well defined thin rim of voids is observed at the interface between the cement paste and the inner wall of the glass tube. In the sample prepared with a w/c of 0.35 drying shrinkage is not recognizable. These evidences are in accordance with what is commonly observed also at a larger scale (e.g. in real concrete applications) where higher shrinkage occurs in the presence of higher w/c ratios. However, no significant cracks due to shrinkage were detected from the inspection of the 3D datasets.

Besides the effect of w/c ratio, also the temporal evolution of a sample may be visualized and investigated using microfocus X-μCT in analogy with has been previously shown for synchrotron X-μCT, even though the limited spatial resolution achievable hamper a precise quantitative analysis. Moreover, microfocus X-μCT cannot provide an adequate temporal resolution during early hydration stages, due to the longer acquisition time. However at later hydration ages (as in this particular case) this is generally not a problem. From a qualitative point of view, the typical evolution of the grey values distributions within the

same selected VOI at different hydration ages can be recognized, as shown both from the slices and the plot in Fig. 5.3. A progressive sharpening of the grey values distribution is observed as a consequence of the continuous growth of hydration products at the expenses of clinker particles (higher GVs) and pores (lower GVs).

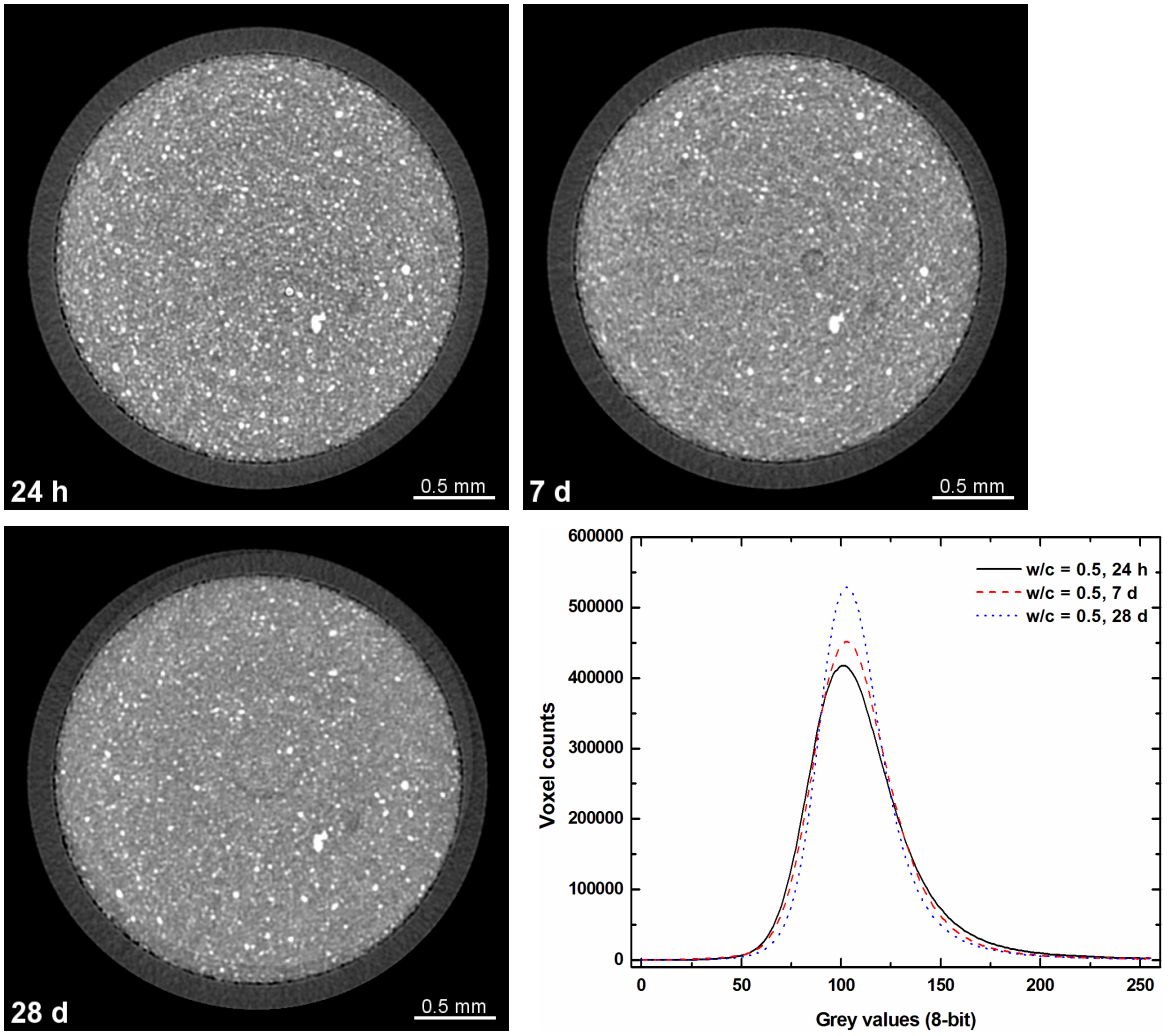

Figure 5.3 - Temporal evolution of a cement paste illustrated by means of corresponding slices and GV histograms. The sample was prepared at a w/c of 0.5 and scanned at 1, 7 and 28 days of hydration. Voxel size in the slices is ~ 5 μm. Histograms were calculated over a cylindrical VOI selected within the cement paste with a diameter of 490 voxels (2.45 mm) and a thickness of 120 slices (0.6 mm), characterized by high homogeneity and absence of large macropores.

In chapter 7, another example of practical application of microfocus X-μCT is presented. The technique has been applied, in combination with other established methods, to the performance evaluation of a method for the solidification and stabilization (S/S) of contaminated soils, based on the use of Portland cement.

6 – Crystal phase mapping in cements using XRD-CT

6.1 Introduction

In the previous parts of this work, some potentialities of X-μCT applied to the study of cementitious materials have been presented. X-μCT provides a map of the variations of the X-ray attenuation coefficient within a sample in a totally non-invasive manner, allowing 3D images to be reconstructed with a spatial resolution approaching the sub-micrometric scale when using modern synchrotron-based systems. As the physical properties of cements are strictly dependent on the evolution of their intimate organization, the ability of investigating such materials without perturbing their micro-structure represents a fundamental advantage. However features having high-density contrast, such as voids and fractures within the solid material, are clearly identified by means of X-μCT, whereas different crystalline or amorphous phases with similar density and composition are hardly distinguished. In order to overcome these limitations, a new generation of non-destructive analytical techniques has been recently developed by combining microbeam-based methods such as X-ray micro-fluorescence and micro-diffraction with the tomographic principles of reconstruction. The X-ray beams produced at modern synchrotron radiation sources can be focused into a very small spot (in the range of μm and even nm) with extremely high intensity, by means of adequate focusing devices. The obtained microbeams can be scanned point-by-point across a sample and the different signals arising from the interaction of X-rays with matter can be measured and mapped, obtaining local quantitative information about one or more selected properties (in analogy with scanning electron microscopy). However, even though classical microbeam-based methods provide a lot of information (e.g. on the local structure) that cannot be obtained when using a broad incident beam, their application is restricted to the study of surface 2D samples and no volume 3D resolution can be achieved.

In this framework during the last decade, the idea of combining microbeam-based methods with the principles of tomographic reconstruction represented a revolutionary approach towards the development of non-destructive 3D probes. Nowadays, experimental techniques such as X-ray fluorescence micro-tomography (XRF-CT, Simionovici et al. 1999) or X-ray diffraction micro-tomography (XRD-CT, Bleuet et al. 2008) allow to map the spatial distribution of selected elements or phases (both crystalline and amorphous) within a heterogeneous sample at the micrometric scale in a totally non-invasive approach.

In this chapter, the first application of the XRD-CT technique to the mapping of selected phases in cement-based materials is described. The experiments were carried out at the ID22 beamline of the European Synchrotron Radiation Facility during the same experimental session previously described in chapter 4. The main purpose of this experiment was to test the feasibility of XRD-CT analyses on cementitious samples and in particular to investigate the phase distribution of ettringite, one of the fundamental hydration phases in cements. The results were then compared with those obtained by means of X-μCT on the same samples. In addition, in the last paragraph of the chapter, some preliminary results of a second XRD-CT experimental session are presented. The aim of this second series of measurements was to investigate the spatial distribution of C-S-H in hydrating cements and to prove that the technique can be applied to amorphous or disordered structures as well.

6.2 XRD-CT basic principles

X-ray diffraction micro-tomography (XRD-CT) is a synchrotron-based experimental technique recently developed at the ID-22 beamline of the ESRF (Bleuet et al., 2008) and consisting in the combination of micro-diffraction with the principles of X-ray computed micro-tomography. The typical experimental setup for XRD-CT in use at the ID-22 beamline is showed in Fig. 6.1.

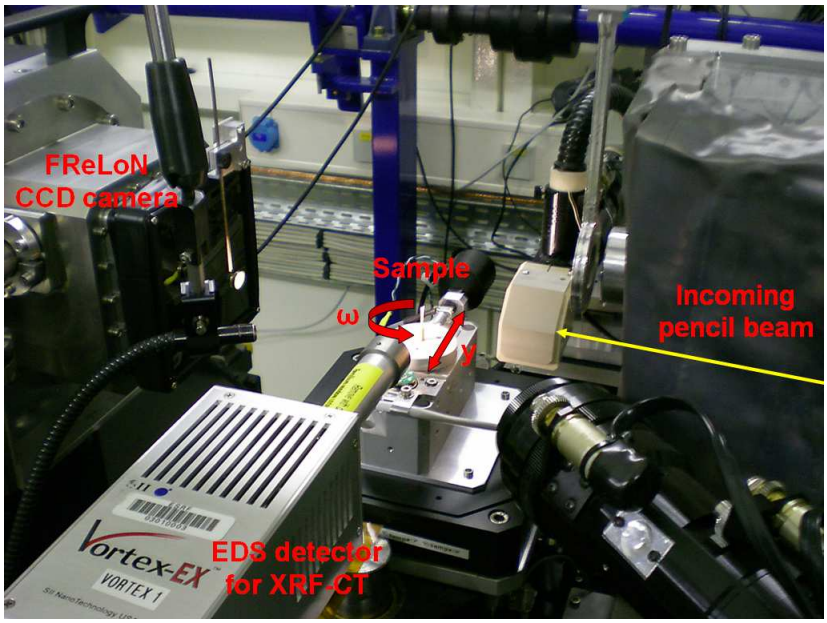

Figure 6.1 - The experimental setup for combined XRD-CT and XRF-CT in use at the ID-22 beamline of the European Synchrotron Radiation Facility.

A Kirkpatrick-Baez mirror system is used to obtain a well collimated pencil beam, which scans the specimen while it is rotated and translated by a high-precision stage; the diffracted X-rays are detected by a FReLoN CCD camera (Labiche et al., 2007). The fluorescence signal emitted by the sample can be simultaneously measured using an EDS detector placed at 90° with respect to the beam. The acquisition and reconstruction scheme for XRD-CT data is illustrated in Fig. 6.2.

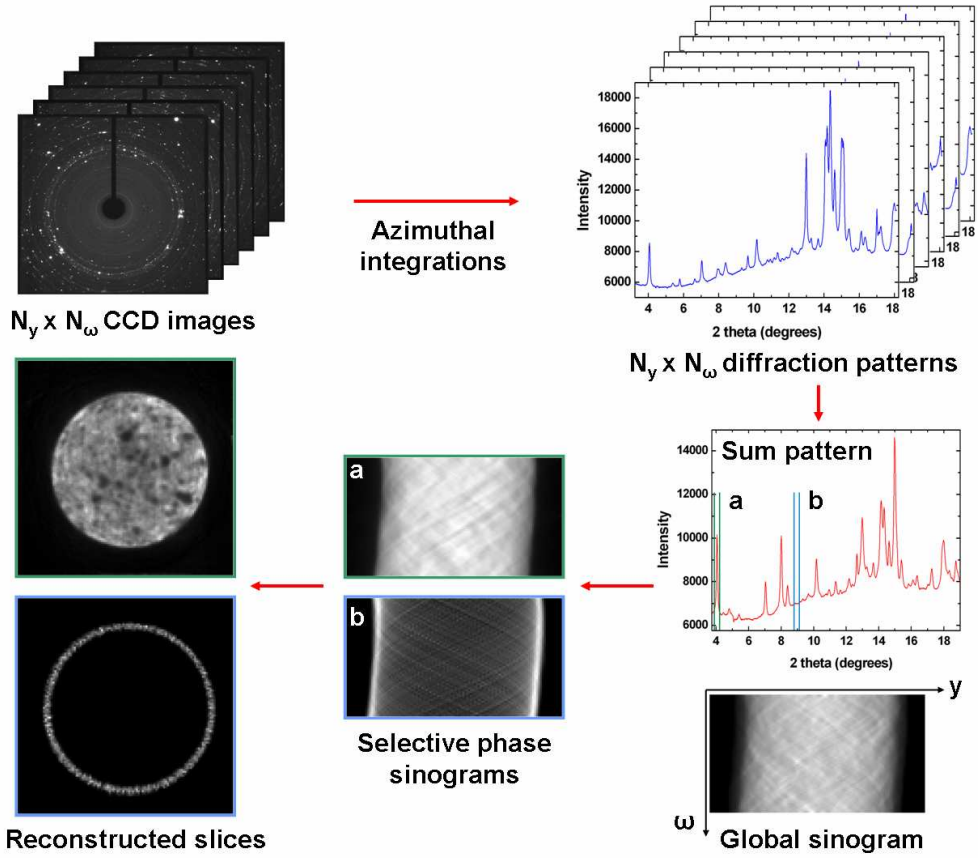

Figure 6.2 - Reconstruction scheme of the XRD-CT direct analysis: for every translation (y) and rotation (ω) of the sample, a 2D diffraction pattern is collected, thus obtaining a set of integrated linear diffraction patterns. Regions of interest corresponding to a particular 2θ range can be selected on the linear diffraction patterns to build up sinograms, representing the variations of the diffracted intensity as a function of y and ω. Sinograms are then used to reconstruct cross-sections mapping the spatial distribution of selected phases of interest.

For each sample rotation (ω) and lateral translation (y), a 2D diffraction pattern is collected by a CCD camera. In practice, each pattern records the contribution to diffraction originating from a line of material within the sample and corresponding to the propagation path of the beam. From the azimuthal integration of all the acquired images, a series of

linear (1D) diffraction profiles is obtained. The stack of images is thus reduced to a 3D dataset whose dimensions are *y* (position), ω (tomographic angle) and 2θ (diffracted angle). A sum pattern is then calculated by summing the linear diffraction patterns over *y* and ω, in order to identify the major phases. The linear diffraction profiles are then integrated along 2θ and the result is plotted as a function of *y* and ω to build up a global sinogram of the investigated slice, which is useful to reconstruct a cross-section of the total diffracted intensity. Regions of interest (ROIs) over any 2θ angular range, corresponding to a given scattering contribution or a diffraction peak can be defined to extract selective sinograms of the corresponding individual phases. Finally, tomographic reconstruction provides a map of the variations of the intensity of any selected ROI (e.g. a peak) in the investigated portion of the sample corresponding to a single slice. The vertical resolution (i.e. the thickness of the slice) is determined by the height of the incident beam.

6.3 Sample preparation and experimental setup

As for X-μCT, diffraction tomography experiments were performed at the ID-22 beamline of the European Synchrotron Radiation Facility (ESRF, Grenoble, France) which can be adapted for both experimental setups. XRD-CT experiments were carried out on two of the samples previously described in chapter 4 for X-μCT measurements, namely sample A (cement paste) and sample C (mortar). The cement sample was prepared by mixing a CEM I 52.5 R powder with de-ionized water, using a water to cement ratio (w/c) of 0.5. For the preparation of the mortar sample, the same cement powder was mixed with a very fine siliceous sand (80-100 μm) and de-ionized water, according to a 2:1:1 mass proportion. Both samples, after 60 seconds of hand-mixing, were manually inserted into thin, cylindrical glass capillary tubes (Ø ~ 500 μm) which were finally sealed with plasticine at both ends.

For the experiments described here, a pencil beam with a size of 4 μm (width) x 2 μm (height) was employed; the energy of the radiation was set to 18 keV (λ = 0.689 Å) by means of a double-crystal monochromator. 2D diffraction patterns were recorded using a lateral step (*y*) of 5 μm and a rotational step (ω) of 3° over a 180° rotation, obtaining a very large number of 2D diffraction patterns (from ~ 6000 to ~ 8000, according to sample diameter). An exposure time of 0.8 s per frame was adopted, resulting in a total scan duration for a single slice of ~ 6-8 h (including readout time and sample movements). The long time required for the measurements is one of the main drawbacks of the XRD-CT

technique, especially when analyzing samples that can evolve during the experiment as fresh cements. The total time required to scan a single slice is of course a function of sample size and absorption as well as of the translational and rotational steps adopted, which determine the spatial resolution. In practice, for the investigated cementitious samples, at the selected level of resolution, the analysis was restricted to 1-2 slices per sample.

The *XRDUA* software package (De Nolf, 2006) was used for the entire process of calibration and correction of 2D diffraction images, azimuthal integration, sinograms extraction and tomographic reconstruction. Diffraction frames were corrected for spatial distortion and dark current; sinograms were normalised for the incident beam intensity (which decays with time due to the finite lifetime of the storage ring beam current). Tomographic reconstructions were carried out using the maximum-likelihood expectation-maximization (MLEM) algorithm (Shepp & Vardi, 1982). In the final reconstructed slices, the voxel size (which is determined by the beam size and the lateral step) was 5x5x2 μm^3.

Two XRD-CT measurements were carried out on the cement sample, starting at 9 h and 58 h from preparation, in order to test the capabilities of the technique in monitoring the evolution of cement hydration over time. In addition, a single scan was performed on the mortar sample, starting at 12 h from hydration. This second sample was chosen in order to verify the feasibility of XRD-CT on a highly heterogeneous system, both in composition and grain size, due to the presence of very large quartz and feldspar crystals.

6.4 Ettringite phase mapping

Tomographic reconstructions based on several angular regions of interest (ROIs) corresponding to different phases were carried out. It was observed that the main factor affecting the quality of the reconstruction process is the grain size of the selected phases. The ideal case for XRD-CT reconstruction is represented by very fine grained phases, whose grain size is approximately one (or more) order of magnitude smaller than the X-ray probe. Under these conditions, each sampled volume (i.e. a voxel in the reconstructed image) may contain a sufficiently large number of variously oriented crystals, to give good powder diffraction signals which are seen as sharp rings on the acquired CCD frames. The best results were obtained with ettringite, one of the most important early hydration products of cement, being this phase very fine grained and well distributed in the studied samples. In addition, the main ettringite diffraction peaks showed high intensities and no

overlapping with other peaks (in particular those of clinker phases), allowing a more reliable intensity extraction. On the other hand, major problems were encountered when trying to map the spatial distribution of other phases, present in the studied samples in the form of larger grains (roughly from 10 to 100 μm), such as C_3S, C_2S, C_3A, CH or quartz, which behave as strongly diffracting single crystals. In the 2D diffraction patterns, their effects are seen as very intense spots, often leading even to an undesired saturation of the CCD pixels. In practice, the volume elements occupied by large single crystals can generate diffraction effects only under those selected viewing angles where the Bragg's conditions for diffraction are satisfied, which are a relatively limited number. As a result, the information from such volume elements over a 180° rotation is highly incomplete and the reconstructed images are affected by severe artefacts, thus hampering an accurate mapping of those phases behaving as single crystals.

An XRD-CT reconstructed slice (or tomogram) for a mortar sample, based on the intensity of the (100) peak of ettringite ($C_6AS_3H_{32}$ in cement chemistry notation), is shown in Fig. 6.3 (left). The selected angular ROI, corresponding to the maximum intensity peak of ettringite, is also highlighted.

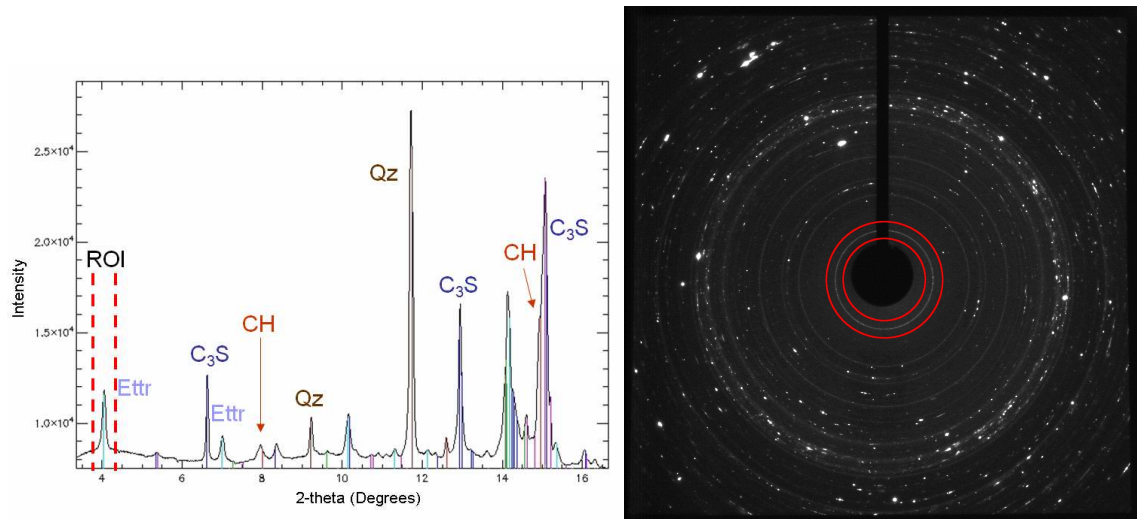

Figure 6.3 - Left: 1D diffraction pattern of a mortar sample showing the angular region of interest (ROI) selected for tomographic reconstruction and corresponding to the low-angle (100) ettringite peak (d_{100} = 9.75 Å). Right: 2D diffraction pattern (CCD image) where the diffraction ring of the (100) ettringite peak has been highlighted in red.

The reconstructed XRD-CT slices are constituted by a matrix of voxels of 5 x 5 x 2 μm^3 whose grey values are proportional to the amount of ettringite within the corresponding volume of the sample as shown for the mortar sample in Fig. 6.4 (left). Brighter voxels

correspond to regions of maximum ettringite concentration while darker ones to its absence (e.g. macro-voids, quartz grains and unreacted clinker). An X-μCT slice of the same sample, corresponding approximately to the same plane of the XRD-CT slice is also shown in Fig. 6.4 (right). A good correspondence can be observed between various features in the two images despite the significant difference in spatial resolution of the two techniques (5 μm in XRD-CT, 0.7 μm in X-μCT). The non-perfect co-planarity of the two slices is due to the fact that X-μCT and XRD-CT measurements are not carried out simultaneously as the experimental setup and operational mode are significantly different. In order to switch between the two techniques, it is necessary to move the specimen to a different sample holder thus introducing a potential slight tilt of the capillary tube and, as a consequence, of the reconstruction plane which is always normal to the rotation axis. The exact plane of XRD-CT reconstruction could be retrieved by an adequate inclined digital cut of the three-dimensional X-μCT stack; however this was not done in this particular case because the amount of the misalignment was very limited (less than one degree).

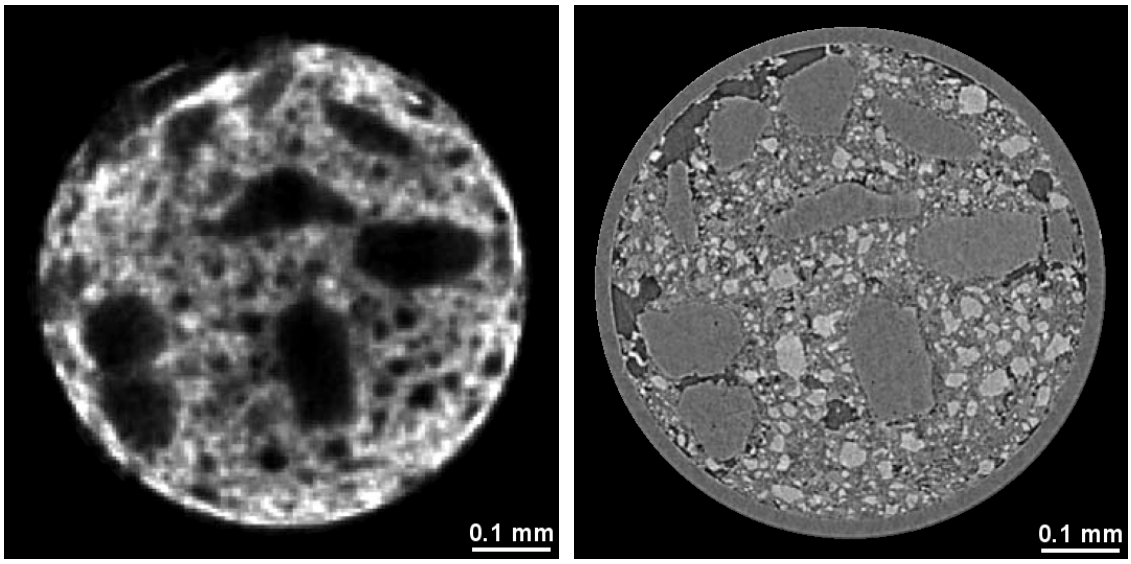

Figure 6.4 - Left: XRD-CT tomogram reconstructed on the basis of the (100) peak intensity of ettringite in the mortar sample at 12 h of hydration. Right: X-μCT slice corresponding to approximately the same cross-section at 6 h from hydration.

Unperturbed phase distribution maps were also obtained for the cement paste sample (sample A) and compared with the corresponding slices extracted from X-μCT datasets as shown in Fig. 6.5. Ettringite appears to be ubiquitously distributed within the cement paste, with slightly higher concentration in areas close to the capillary walls. A non-

homogeneous distribution of the paste is also visible in the X-μCT image where it can be observed that the compactness of cement increases from the capillary towards the centre. The preferential growth of ettringite in less compact areas of the sample can be interpreted as due either to the favoured circulation of sulphate-rich pore solution near the capillary walls or to the difficulties in achieving an homogeneous filling of the capillary.

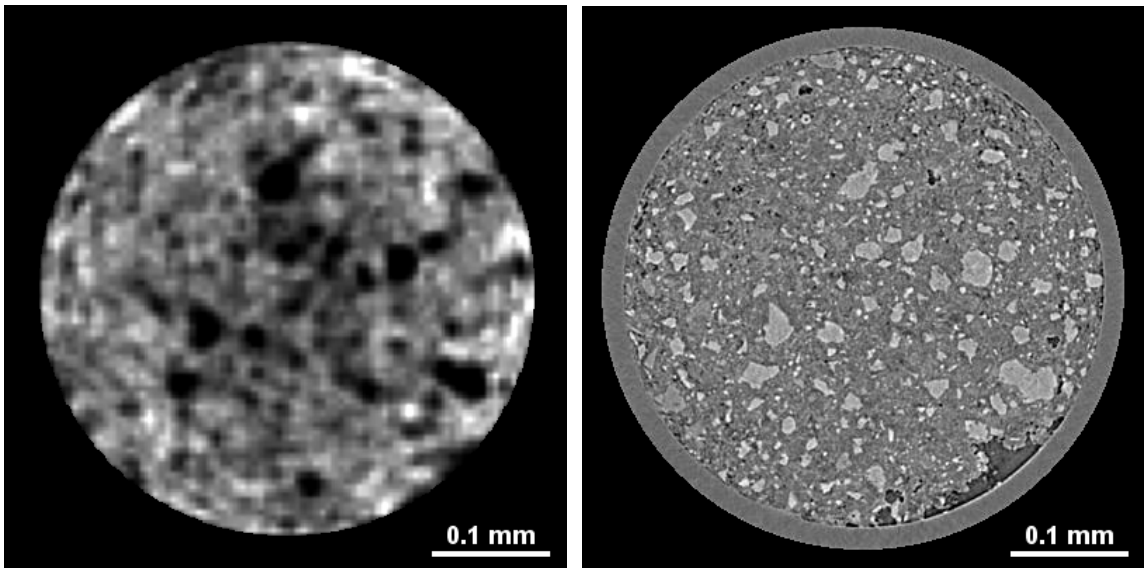

Figure 6.5 – Left: XRD-CT tomogram based on the (100) peak intensity of ettringite in the cement sample at 58 h of hydration. Right: X-μCT slice of approximately the same cross-section of the cement sample at 48 h of hydration.

The evolution of the ettringite content as a function of hydration time was also studied by comparing the grey values histograms of two reconstructed XRD-CT slices of the same sample measured at different hydration ages, 9 and 58 h respectively (Fig. 6.6). As the age of the cement increases, a shift of the distribution towards higher values is observed, indicating an increase of ettringite volume fraction per pixel. Ettringite weight fractions in the sampled slices were also estimated by means of Rietveld refinements on the averaged diffraction patterns. The results obtained (14 wt% and 22 wt% at 9 and 58 h respectively) confirmed the increase in ettringite concentration observed in the grey values histograms. However, as it was not possible to quantify the amorphous content (e.g. C-S-H) by means of the Rietveld method, the calculated weight fractions should not be considered as absolute values and were used just to compare the relative ettringite evolution in the cement sample during hydration.

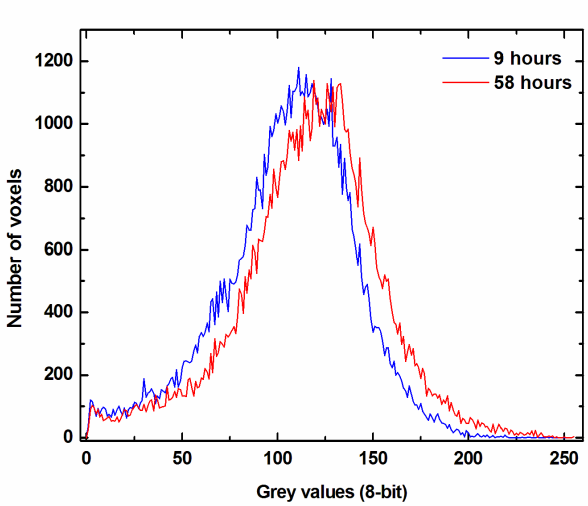

Figure 6.6 - Variations in the grey value histograms relative to reconstructed ettringite tomograms of the cement sample at 9 and 58 h from hydration.

In order to confirm the reliability of the XRD-CT tomogram reconstruction and the reproducibility of the method, ettringite mapping was carried out also on the basis of the (110) diffraction peak, which is the second most intense peak for this phase. The reconstructed slice was then compared with the results previously obtained using the (100) peak. As shown in Fig. 6.7, a good correspondence can be found between the two images for what concerns the distribution and concentration of ettringite. The overall higher brightness (i.e. higher concentration) in the ettringite map on the left is due to the fact that (110) tomogram normalization was biased by other peaks interfering in the selected ROI.

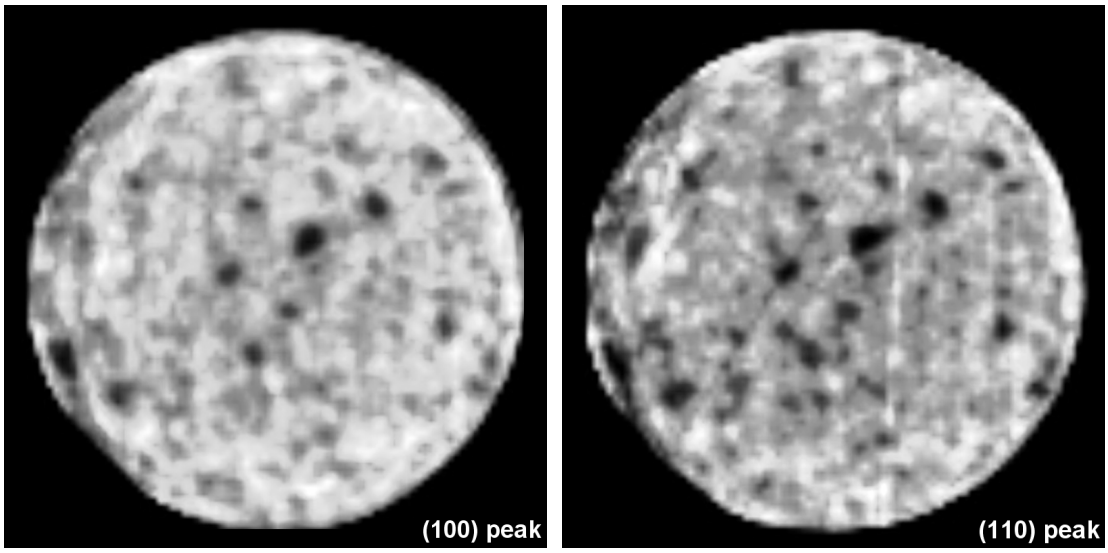

Figure 6.7 - XRD-CT tomograms showing the intensity variations of the (100) and (110) ettringite peaks (d_{100} = 9.75 Å and d_{110} = 5.63 Å) within a cement paste sample. Sample diameter ~ 400 μm.

In addition, it was demonstrated that the XRD-CT technique can be applied also to the mapping of non-crystalline phases as illustrated in Fig. 6.8. An angular region characterized by a high scattering contribution originating from the glass capillary was selected for XRD-CT reconstruction. As a result, a map containing only a single bright ring corresponding exactly to the capillary tube was obtained. This suggested that the selection of appropriate portions of the scattering data could also provide information on the distribution of C-S-H. A second experiment was planned accordingly (see par 6.6).

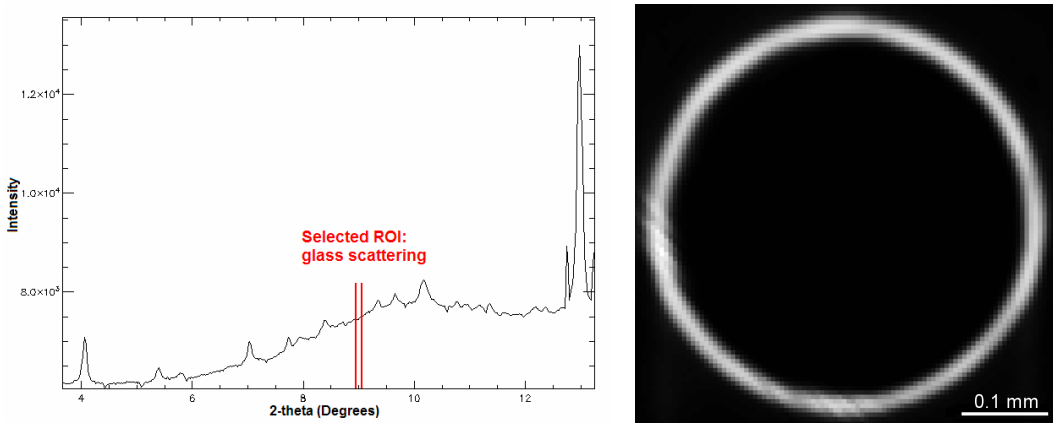

Figure 6.8 - Left: diffractogram illustrating the selected angular region of interest corresponding to the scattering contribution from glass. Right: reconstructed tomogram showing the intensity variations of the ROI within the investigated cement sample. The bright ring-shaped region corresponds exactly to the glass capillary tube.

6.5 XRF-CT

As previously shown in Fig. 6.1, the microbeam experimental setup of the ID22 beamline includes also an energy dispersive spectrometer (EDS), placed at 90° with respect to the beam, for the simultaneous detection of the characteristic fluorescence radiation emitted by the sample. In analogy with what has been shown in XRD-CT, for each combination of y and ω (lateral and angular position respectively) an XRF spectrum of a single line of material within the sample is collected. A spectral ROI, corresponding to the fluorescence peak of a selected element can be defined on the acquired spectra. Then, by applying a reconstruction algorithm very similar to the one used for XRD-CT, a map of the intensity distribution of the selected fluorescence peak across a slice of the sample is obtained. This is what is commonly referred to as X-ray fluorescence micro-tomography (XRF-CT). The simultaneous acquisition of the XRD and XRF signals offers a great opportunity for a totally non-invasive, multi-disciplinary approach with phase and elemental sensitivity,

whose potentialities in the field of materials science are enormous.

The results of an XRF-CT analysis carried out on the mortar sample previously described are presented in this paragraph. XRF-CT mapping strongly suffered from the high self-absorption of the fluorescence X-rays inside the sample. Good results were obtained only for those elements having higher emission energies, even if present at very low concentrations. Fig. 6.9 shows the reconstructed maps obtained for Si ($K\alpha_1$ = 1.740 keV) and Rb ($K\alpha_1$ = 13.395 keV). Due to the strong self-absorption of the emitted radiation within the sample, the presence of Si can be detected only in the external portion facing the detector (i.e. upwards in Fig. 6.9), corresponding to half of the glass capillary. Practically no information could be extracted from the central part and far side of the sample, due to the high attenuation of the low-energy emission line of Si. On the other hand, the reconstructed map for Rb, whose emission energy is significantly higher, appears more complete even though the effect of self-absorption is still recognizable. If the Rb-map is compared with the corresponding X-μCT and XRD-CT slices (Fig. 6.4), a strong, local concentration of Rb is observed in a single sand grain. This latter is almost certainly a K-feldspar ($KAlSi_3O_8$) crystal, a phase which typically includes in its structure significant amounts of Rb in substitution of K. It is interesting to note that, on the basis of the simple absorption signal, this grain could not be distinguished from the other sand particles, due to the very similar absorption coefficient of quartz and K-feldspar.

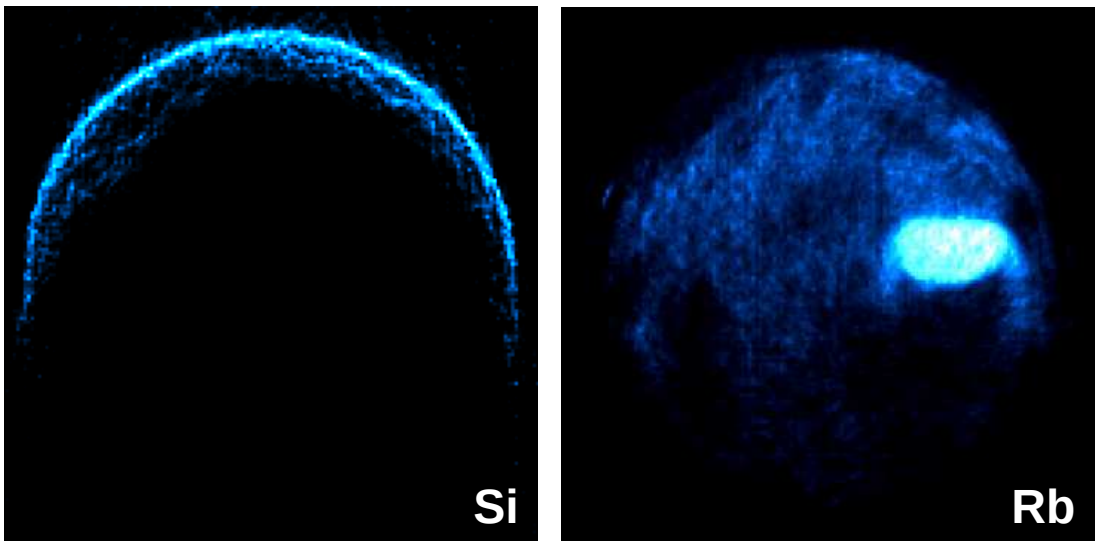

Figure 6.9 – Maps of the distribution of silicon and rubidium in the same slice shown in Fig. 6.4, obtained by means of XRF-CT reconstruction of a mortar sample. Higher brightness values correspond to higher concentrations. Sample diameter ~ 610 μm.

6.6 C-S-H phase mapping

In the previous paragraphs, the suitability of XRD-CT for the phase mapping of ettringite in hydrating cementitious systems was demonstrated. Satisfactory results were obtained because ettringite was present in the investigated samples in the form of very fine-grained crystals which yield well recognizable powder diffraction patterns. Under these ideal conditions the reconstruction of the intensity variations of selected diffraction peaks is quite easy to achieve. In addition, it was shown that also amorphous phases such as glass can be successfully mapped by selecting adequate angular regions of scattering. Major problems were encountered when trying to map phases characterized by a "single-crystal" behaviour because the standard requirements for XRD-CT reconstructions are not fulfilled in such cases. In addition, no information was obtained about C-S-H which is known to be the main responsible of the development of strengths in cements. This was due to the lack of well-defined diffraction peaks to be selected for reconstruction, being this phase characterized by a poorly crystalline structure and extremely variable composition. Historically, two C-S-H types have been described, namely C-S-H(I) and C-S-H(II) according to their Ca/Si ratio (Taylor, 1990). Their structure show similarities with those of tobermorite and jennite, two rare Ca-silicate hydrate minerals with a layered structure. A comprehensive review on the different structural models of Ca-silicate hydrates proposed in the literature during the last fifty years has been recently written by Richardson (2008). In a recent XRPD study, Renaudin et al. (2009) reported the presence of strong contributions from C-S-H in a low-angle region corresponding to a broad low-angle basal peak. A similar effect is also recognizable in the diffraction patterns reported in Fig. 6.10 which were measured at different hydration ages on a C_3S + C_3A + gypsum simplified cementitious system.

During the previously described XRD-CT experimental session, it was not possible to access the angular region corresponding to the C-S-H broad peak, due to the shadowing effect of the beam stopper at low diffraction angles. Thus, a second series of XRD-CT experiments was carried out at the ID-22 beamline of the ESRF using a slightly different setup, in order to try to map the spatial distribution of C-S-H. In this case, a smaller beam stopper was adopted and the energy of the beam was decreased from 18 to 17 keV (therefore increasing λ from 0.689 to 0.730 Å) in order to access the C-S-H low-angle scattering region. The size of the beam was maintained at 4 x 2 μm^2 while the lateral and

angular steps were reduced (4 μm and 1.5°) with respect to the previous experiment. A CEM I 52.5 R OPC paste, prepared at a w/c ratio of 0.5 was selected for this study. As for the previous experiments, XRD-CT measurements were performed in combination with X-μCT scans (see par. Xx for experimental details) in order to compare cross-sectional slices reconstructed using the two different techniques.

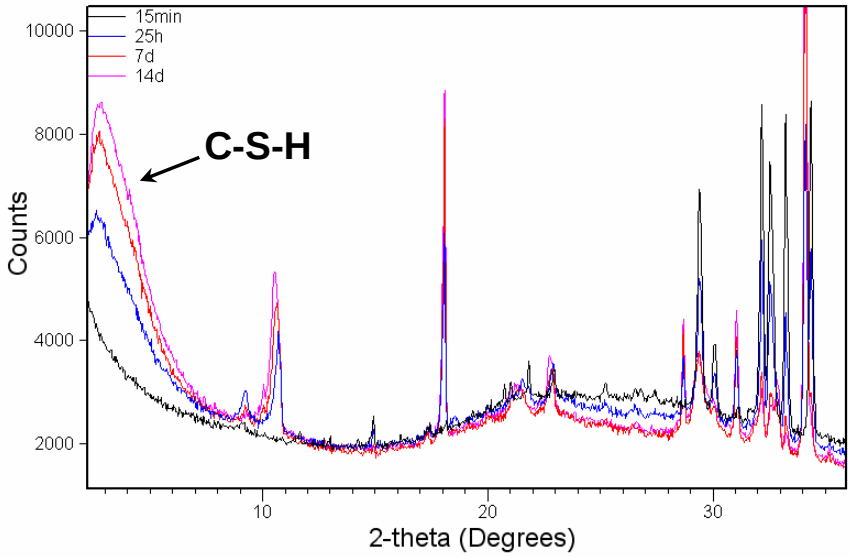

Figure 6.10 – X-ray powder diffraction patterns (focusing transmission capillary geometry) showing in-situ evolution during hydration (from 15 minutes to 14 days) of a simplified cementitious system constituted by C_3S, C_3A and gypsum. A progressive increase of the low-angle broad basal peak (d ~ 33 Å) of C-S-H is observed. The radiation used was Cu-Kα (λ = 1.541 Å).

Some preliminary results of XRD-CT reconstructions of different angular regions (C-S-H and ettringite) are reported in Fig. 6.11. The distribution of ettringite and C-S-H were successfully mapped within a slice of the sample by reconstructing the intensity variations of the (110) peak of ettringite (d_{110} = 5.63 Å) and the C-S-H low-angle broad peak (d ~ 33 Å, unknown crystal structure). Even though the spatial resolution in the XRD-CT images is approximately one order of magnitude lower if compared to X-μCT (4 μm vs 0.35 μm), a high degree of correspondence can be found between microstructural features in the two images. Moreover, the image quality appears substantially improved in comparison with previous XRD-CT results as a consequence of the narrower lateral and rotational steps adopted. As expected, no C-S-H and ettringite are detected in regions occupied by large pores, clinker grains or portlandite crystals (see X-μCT image), thus confirming the reliability of the technique. Moreover, due to the different mechanisms of nucleation and growth of ettringite and C-S-H, the two phases show considerably different distributions

throughout the hydrated paste. A combined comparison of ettringite and C-S-H maps with the X-μCT slice allows to identify preferential concentrations of C-S-H around larger clinker particles (some of them being completely replaced by C-S-H, as shown in the red square in Fig. 6.11) whereas ettringite appears more uniformly distributed.

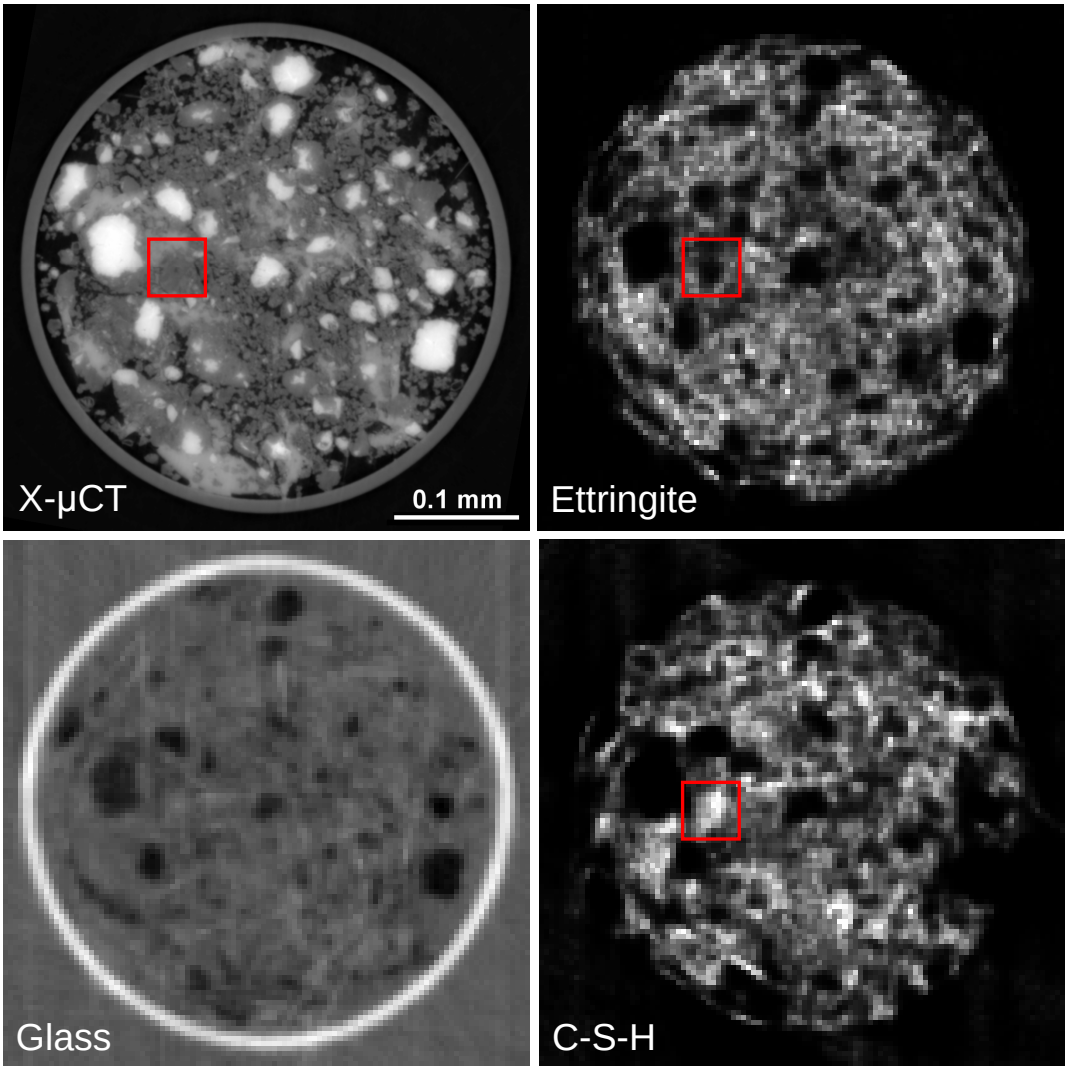

Figure 6.11 - Comparison of corresponding X-μCT and XRD-CT slices for a cement paste (w/c = 0.5) at 7 days of hydration, voxel size: 0.35 and 4 μm respectively. In XRD-CT maps, grey values are proportional to the intensity of the selected ROI (i.e. to the concentration of the relative phase) while in X-μCT they are proportional to density. Top left: phase retrieval X-μCT slice (see par. 4.5). Top right: XRD-CT mapping of the intensity variations of the (110) peak of ettringite. Bottom left: XRD-CT mapping of glass showing also absorption effects due to variations in intensity of the selected angular ROI. Bottom right: XRD-CT mapping of the low-angle wide peak of C-S-H.

7- Application of X-μCT to the characterization of cementitious granular materials produced from contaminated soils

In this chapter, microfocus X-ray computed micro-tomography has been combined with other established experimental techniques (mercury intrusion porosimetry, physico-mechanical and leaching tests) to the characterization of granular cementitious materials produced from the solidification and stabilization process (S/S) of soils contaminated by heavy metals. In particular X-μCT has been used to study the pore size distribution within two sets of samples prepared following two different formulations.

7.1 Introduction

The mitigation of the impact of anthropogenic activities on the environment (either atmosphere, hydrosphere or land) represents one of the most challenging goals in the wide field of environmental sciences. In particular, the study of soil pollution and the re-qualification of lands contaminated by hazardous wastes represent the major topics of investigation wherein the cement scientific community may be actively involved.

Recently, the term “brownfields” has been introduced to indicate areas formerly occupied by abandoned industrial or commercial facilities (e.g. power plants, factories, chemical warehouses, junk yards, fuel stations, etc.) whose re-utilization is hindered by a strong environmental contamination. Brownfield sites are often located close to urban areas and this of course increases their degree of human and environmental hazard. Typical contaminants that may be found on these lands, both organic and inorganic, include hydrocarbons, dioxins, PCBs, PCDFs, heavy metals, metalloids and asbestos. In such critical situations, the classical approach based on the disposal of the contaminated ground in dumps and the subsequent refilling of the site with new materials is not sustainable anymore, both environmentally and economically. As a consequence, a specific treatment and recycling of the polluted soils and sediments, in accordance with the European directives, has become necessary. Nowadays, the solidification/stabilization (S/S) techniques (Cullinane et al., 1986) allows to reduce the solubility and mobility of solid and liquid wastes by mixing the contaminated materials with a binder (typically Portland cement), in order to obtain a final product characterized by increased workability and physico-chemical stability. Their effectiveness depends not only on the physical mechanism of encapsulation into a high-strength and low-porous matrix, but also on

chemical processes as the uptake of some elements by certain cement hydration products such as ettringite and C-S-H (Glasser, 1994, Klemm, 1998). Over the past two decades, S/S methods, both *in situ* and *ex situ*, have found increasing application in a large number of environmental remediation actions. For instance, 24 per cent of the US Superfund Program remedial actions involving source-control in the period 1982-2002 were based on S/S technologies (US EPA 2004). Laboratory and *in situ* leaching tests have widely demonstrated that S/S techniques can substantially reduce the concentration of contaminants into the ground, well below the limits fixed by laws for the residential use. However, some controversial issues still remain about the long-term performance of such products, due to the degradation of the cement matrix with time.

In the present work an innovative S/S process, called Mapintec HPSS (High Performance Solidification and Stabilization) and founded on the principles of high performance concretes (HPCs) is presented.

7.2 The *Mapintec HPSS* process

The *HPSS* (High Performance Solidification/Stabilization) developed by Mapintec S.r.l. (Mapei S.p.A. group) is an integrated solidification/stabilization and decontamination process for the treatment of contaminated soils and sediments. The HPSS process aims at producing cm-sized granular cementitious aggregates (see Fig. 7.3) characterized by extremely low leaching values, good environmental compatibility, high mechanical strength and improved durability. The granular nature of the final product is the main aspect that differentiates the HPSS method from conventional S/S techniques; the stabilized material can be re-used *in situ* as backfillings or as aggregates in non-structural concretes.

As mentioned earlier, the process is based on the technology of high performance concretes and in particular on the use of superplasticizing and hydrophobic additives. The American Concrete Institute (ACI) defines HPCs as concretes meeting special combinations of performance and uniformity requirements which cannot be achieved routinely when using conventional constituents and normal mixing, placing and curing techniques. One of the commentary to the definition states that a high-performance concrete is one in which certain characteristics are developed for a particular application and environment. Examples of characteristics which are considered critical in HPCs are: long term mechanical properties, permeability, density, volume stability and long life in

severe environment. All these properties are correlated and largely depend on the amount of water used in the concrete mixture. It is well known that water to cement ratio (w/c) is the main factor which determines most of the properties of hardened concrete; by lowering w/c, also the porosity of the microstructure of the cement paste and consequently its permeability to liquid and gaseous aggressive agents from the environment are reduced and all its properties are consequently improved. Superplasticizers (see par. 1.5) are essential ingredients for the production of HPCs; they consist of water soluble polyelectrolytes which dramatically reduce the viscosity of fresh cement mixtures and allow to cast flowable, easy to place concretes characterized by low w/c ratios (≤ 0.4). Other important ingredients for the production of HPCs are mineral admixtures, such as natural pozzolanas, silica fumes, fly-ashes and other pozzolanic materials. Portlandite produced from the hydration of clinker's Ca-silicates, due to its high solubility (about 2 mg/L) can be dissolved by the water present in the pores and washed off from the cement microstructure. This process causes the progressive broadening of the capillary pores and favours the intrusion of aggressive agents from the environment (sulphates, chlorides) which accelerate the degradation of concrete microstructure. Pozzolanic materials are added to cement mixtures at dosages from 5 to 30% and react with calcium hydroxide present in cement mixtures forming additional silicate hydrates, according to the following reaction:

$$\text{Amorphous silica (S)} + \text{CH} = \text{C-S-H} \quad (7.1)$$

This produces the double beneficial effect of transforming the highly soluble portlandite into the less soluble C-S-H and reducing the porosity of cement microstructure by the formation of new silicate hydrated products. The combination of superplasticizers and mineral admixtures presently represents the best way to improve the microstructure of cement paste and consequently to produce HPCs with higher durability (Collepardi, 2006).

The HPSS method consists of two main steps:

- inorganic decontamination (mainly heavy metals and metalloids) and production of the granular conglomerate by means of specific production apparatuses;
- removal of organic volatile compounds and semi-volatile substances directly from the solidified granular material by means of a thermal desorption process. Of course, in situations where the nature of the contamination is exclusively inorganic, this second step is not necessary.

At the beginning of the process, the contaminated material is excavated and trasported to a dedicated plant placed directly on the remediation site. The procedure of inorganic decontamination is subdivided into the following four stages (Fig. 7.1):

- *Sieving*. In order to remove the coarser fraction (diameter > 2 mm) of the ground, typically constituted by gravel, bricks or generic waste materials, the excavated material undergoes a preliminary sieving treatment. This is done because the granulation process is effective only on the fine fraction of the soil or sediment which is generally the most contaminated. The coarser materials are easily separated (e.g. by means of vibro-sieving) and are generally re-used after being washed in order to remove the superficial contamination. If the contamination of the coarse fraction is stronger, the material is disposed in specific dumps.
- *Water content reduction*. The ideal humidity content for the production of the HPSS grains is generally comprised between 10 and 20% on the total weight of the soil or sediment. For soils excavated in the presence of water, these values are commonly exceeded and the excess of water has to be eliminated. This is generally done by means of filter press or air drying processes or by adding a small amount of CaO that reacts with water.

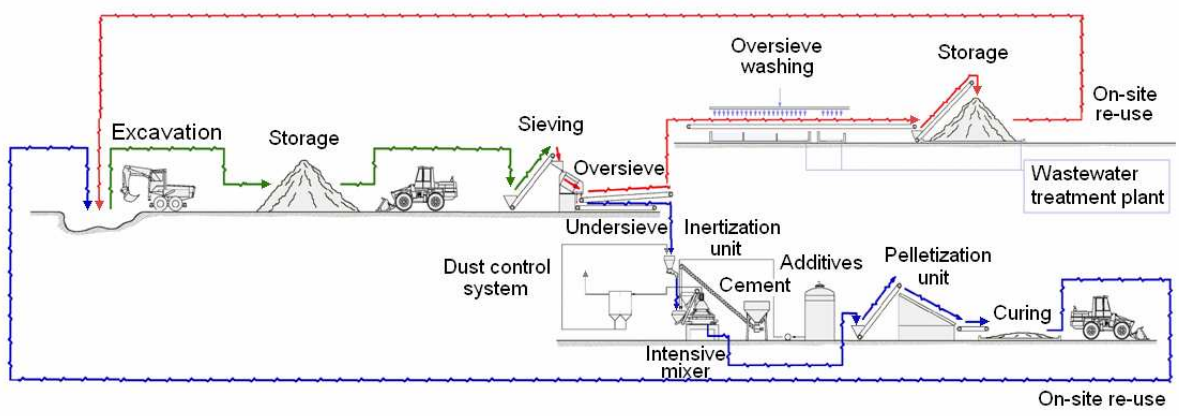

Figure 7.1 - Schematic representation of the inorganic decontamination and granulation (pelletization) step of the HPSS process.

- *Mixing*. The contaminated material is then mixed with Portland cement, additives and, if required, additional mixing water in an intensive mixer (Fig. 7.2) for a few minutes. The two additives employed, Mapeplast ECO1 A and Mapeplast ECO1 B have been specifically developed by Mapei S.p.A. for environmental applications

and are characterized by high biodegradability and low toxicity. The Mapeplast ECO1 B superplasticizer (PCE-type, see par. 1.5.2) is constituted by a mix of hydrosoluble polymers that, by reducing the required amount of mixing water, allow to significantly reduce the porosity of the final granular material thus limiting the leaching of contaminants and the penetration of aggressive fluids. This aspects are further limited by the hydrophobic properties of the Mapeplast ECO1 A additive.

The resulting mixture is a wet, finely divided mass, with the same aspect of the starting soil/sediment, but due to the intensive mixing and the effect of the superplasticizer, the nucleation of micro-seeds takes place within the whole mass.

- *Granulation*. The fresh mixture is then transferred onto an inclined rotating plate (Fig. 7.2) where the nuclei start to increase their size through a mechanism similar to that of a growing snowball. In this way, a granular material (also referred to as *pellets*) is formed whose final size depends on the rotational speed and the inclination of the plate as well as on the duration of the treatment and on the amounts of water and additives employed (Fig. 7.3). Typically, the pellets exit the rotating plate with a final diameter ranging from 4 to 16 mm and are finally stored and cured properly. If the nature of the contamination is also organic, the granular material undergoes the second stage of the process (thermal desorption) before being re-used.

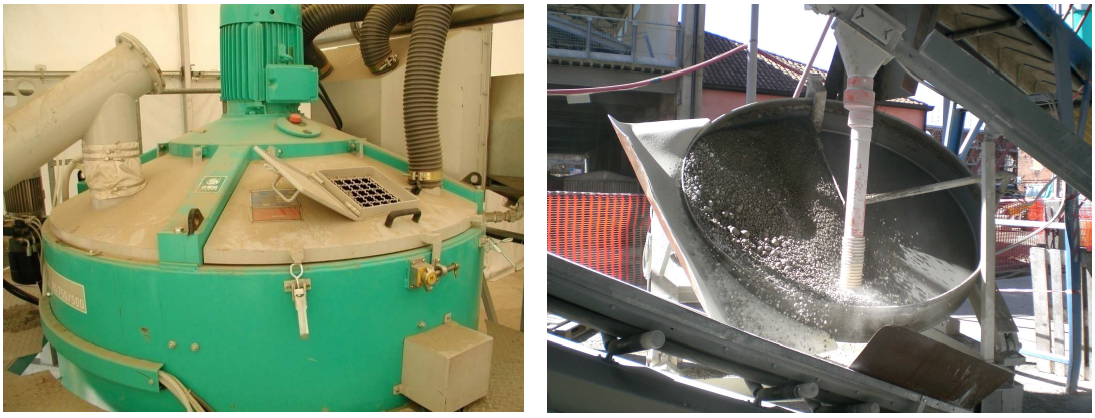

Figure 7.2 - An industrial intensive mixer (left) for blending the initial components and an inclined rotating plate (right, diameter ~ 3 m) for the production of HPSS granular material.

During the thermal desorption stage, the granular materials produced in the first step are heated in a reactor at temperatures comprised between 100 and 250 °C at reduced pressure

(P ~ 0.1 bar), in order to distillate the organic contaminants directly from the grains. In this way it is possible to drastically reduce the problems related to the development of dusts during distillation with a consequent simplification of the dust control system. More than 95% of volatile and semi-volatile organic contaminants (light and heavy hydrocarbons, dioxins, PCBs, PAHs) as well as volatile metals such as Hg can be removed after this stage. Due to the mild operating conditions, the cement microstructure is not substantially degraded and the mechanical properties of the granular materials remain essentially the same.

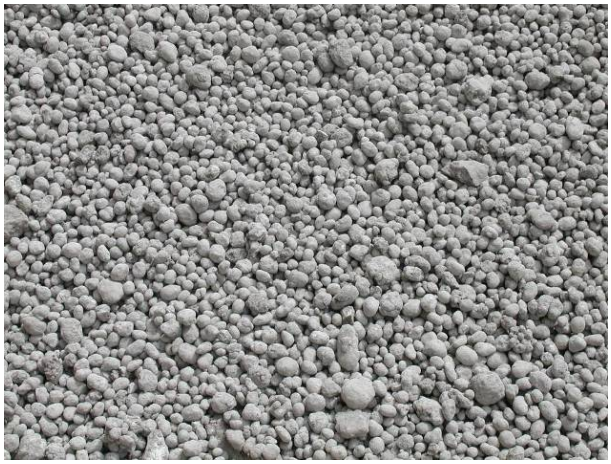

Figure 7.3 - Artificial granular material obtained following the HPSS process. The diameter of the grains ranges approximately from 4 to 16 mm.

7.3 Experimental

7.3.1 Site description and sample preparation

The samples studied in this work were prepared using a contaminated soil from the "ex-Conterie" industrial site (Fig. 7.4) in Murano, Venice (Italy). In this area the HPSS process is currently being applied for the first time at industrial scale for the re-qualification of a contaminated site. In the "ex-Conterie" area, an ancient factory for the manufacture of artistic glass had been operating until 1990. Such activity introduced a significant environmental contamination, mainly due to inorganic pigments and additives, based on heavy metals and arsenic. In the glass industry a great variety of compounds (oxides, chlorides, sulphates, etc.) may be added during the production process in order to modify the final properties of the glass, especially in terms of colour, opacity and refractive index. A total volume of ~ 30000 m^3 of ground is estimated to have been affected by the contamination.

Figure 7.4 - An aerial view of the “Ex-Conterie” site (circle) in Murano (photo from Google Maps).

The ground of the "ex-Conterie" area may be roughly classified as a sandy silt, containing also a minor amount of coarser particles; only the granulometric fraction thinner than 2 mm (the same used for the production of the S/S pellets) was studied here. The results of an XRF analysis performed on the original soil are reported in Tab. 7.1. The significant amount of Pb, Ba, Sr, Zn, Cu and Cr detected, confirms the presence of a real contamination on the area. In a recent work (Parisatto et al. 2011), the contamination of the "ex-Conterie" site and the mechanisms of fixation of contaminants in the cementitious matrix of the pellets was studied by means of SEM and micro-PIXE (particle-induced X-ray emission) analyses.

Major elements (wt %)				**Trace elements (ppm)**					
Na_2O	0.96	**CaO**	35.62	**S**	5040	**Zn**	398	**Ba**	529
MgO	7.97	**TiO_2**	0.51	**V**	73	**Rb**	59	**La**	19
Al_2O_3	7.47	**MnO**	0.09	**Cr**	105	**Sr**	490	**Ce**	42
SiO_2	40.32	**Fe_2O_3**	4.08	**Co**	9	**Y**	23	**Nd**	20
P_2O_5	0.22	**Total**	**98.55**	**Ni**	35	**Zr**	150	**Pb**	719
K_2O	1.31	**L.O.I.**	28.75	**Cu**	201	**Nb**	16	**U**	3

Table 7.1: Quantitative XRF analysis of a soil sample from the “ex-Conterie” site. As, Cd and Hg were not included due to their volatile behaviour and the lack of appropriate calibration standards. The analysis was carried out using a Philips PW 2400 sequential WDS spectrometer.

The S/S granular materials were prepared by mixing the "ex-Conterie" soil with an ordinary Portland cement (CEM I 52.5R), water and the Mapeplast ECO1 (part A and B) additives. Two distinct sets of granular samples have been produced with the soil and then investigated here. The grains included in the first batch (sample A) were prepared with the wet granulation step without additives, while those belonging to the second group (sample B) were produced according to the HPSS method, including the Mapeplast ECO1 additives. The formulations of the investigated samples are reported in Tab. 7.2. Both sets of samples were cured for more than 60 days in normal conditions (23 °C and 95% relative humidity) before being analyzed by means of X-ray computed micro-tomography, mercury intrusion porosimetry, leaching and physico-mechanical tests and thermal analyses.

Ingredient/Property	**Composition (g)**	
	Sample A	**Sample B**
"Ex-Conterie" soil	1000	1000
Portland cement (CEM I 52.5R)	400	400
Mapeplast ECO1 (part A+B)	-	11
Water	280	210
w/s(*)	0.20	0.15

Table 7.2 - Composition of the two investigated sets of granular samples. Water to solid ratio (w/s) refers to the ratio between water and total solids (i.e. the sum of cement and soil). It can be easily seen that sample A, produced by means of the wet granulation process without additives, required 25 % more water in comparison with sample B, produced with a dosage of 0.8 % of additives by weight on the whole solid material.

7.3.2 X-μCT setup

Tomographic scans on S/S products were carried out using the microfocus system in use at the Tomolab facility, Basovizza (Trieste, Italy); a complete description of the instrument is given in section 3.1. The microtomography experiments described here were mainly focused on the investigation of the microstructure of the pore system that plays a fundamental role in cement-based materials not only for their mechanical properties but also for their durability (e.g. freeze-thaw resistance) and transport properties. A few samples, approximately 6-8 mm in diameter, were selected from the two groups (sample A and B) of solidified grains; the chosen size was a good compromise between representativeness, overall X-ray absorption and spatial resolution achievable. The source voltage and the beam current were slightly adjusted for each experiment according to the

amount of absorption shown by the sample and varied in the range of 70-74 kV and 108-110 μA. 1440 projections over a 360° rotation (angular step: 0.25°) were acquired per each scan, with an exposure time per frame ranging from 5 to 5.3 s. The source-object and source-detector distances were set at 80 and 330 mm respectively (M = 4.125). With this experimental setup, the voxel size in the final images was approximately 6 μm (the detector operated in 2x2 binning mode during data acquisition, i.e. with a pixel size on the scintillator of 25 μm). A 0.5 mm thick Al filter was placed in front of the source in order to suppress the low energy portion of the spectrum and reduce the beam hardening effect. After reconstruction, each entire original data sets, composed by more than 1000 contiguous slices, was down-sampled from 16-bit to 8-bit grey scale, in order to reduce the file size and the computational demand for the analysis. The contrast of the reconstructed images was then enhanced by stretching the GV histograms of the stacks, trying to keep brightness and contrast as constant as possible for the various samples. A gentle smoothing of the images was then performed by using a 3x3x3 median filter that allowed to reduce the noise without significantly modifying the information contained in the datasets. For each sample, the pore fraction was then extracted by accurately thresholding the reconstructed images on the basis of their grey value histograms, thus obtaining a stack of binary images where voids are represented in black (GV = 0) and the solid fraction in white (GV = 255). It should be pointed out that significant errors may be introduced during this step, so particular care has to be taken in the choice of the threshold value, especially when comparisons between different samples have to be made. For each sample, almost the entire reconstructed volume has been considered for the calculation of porosity, excluding only a few upper and lower slices of the stack. In order to work with a larger, more representative volume, no cropping of the central portion of the slices was performed; this was possible because the edge effects due to beam-hardening were adequately corrected using the polynomial correction described in section xx.x. After the segmentation of the pore fraction, the total entrained air content and the pore size distribution were calculated. All the image processing operations described here were carried out using the ImageJ software (Abramoff et al. 2004) and related plugins.

7.3.3 Mercury intrusion porosimetry

Mercury intrusion porosimetry (MIP) is a widely used technique for the characterization of the pore space properties of many materials, including cement-based materials. MIP can

provide indirect measurements of total porosity, pore size distribution and other related properties, detecting pores ranging from a few hundreds of μm down to the nm scale. In the present study, MIP experiments have been carried out in order to estimate the differences in total porosity and pore size distribution between S/S grains produced by the wet process without additives (Sample A) and those prepared using superplasticizers (Sample B). MIP is based on the fact that mercury is a non-wetting fluid, therefore a pressure needs to be applied in order to force the liquid metal into the empty pores of a certain material. By progressively incrementing the pressure applied to the mercury surrounding the sample, increasingly smaller pores can be intruded. The well-known Washburn's equation relates the diameter of the intruded pore to the applied pressure, in a porous system assumed to be constituted of a network of cylindrical pores, entirely and equally connected to the exterior of the sample. Washburn's equation is usually written as follows:

$$d = \frac{-4g\cos\theta}{P} \qquad (7.2)$$

where d is the diameter of the cylindrical pore being intruded, g is the surface tension of mercury (~0.48 N/m at 20 °C under vacuum), θ is the contact angle between mercury and the solid (typically between 135° and 142°) and P is the applied pressure.

MIP measurements were carried out at the Environmental Agronomy Department of the University of Padua (Italy) using two Thermo Scientific Pascal 140/240 porosimeters. The first instrument can reach an intrusion pressure of 0.4 MPa, detecting pores ranging from ~200 to ~4 μm in diameter while the second one can measure the finer pore fraction (diameter up to 6-8 nm) with a maximum pressure of 200 MPa. For each measurement, in order to improve the statistical significance of the experiment, several S/S grains (previously dried) were put inside the porosimeter chamber at the same time, for a total mass of approximately 4 grams of material.

7.3.4 Leaching tests, physico-mechanical tests and thermal analyses

Leaching tests were carried out on fractions of granular materials of sample A and B according to the EN 12457/2 method. 100 grams of each sample, after reduction of the grain size below 4 mm, were mixed with 1 litre of de-ionized water (liquid to solid ratio, l/s = 10) for 24 hours. Eluates from the leaching tests were then analyzed according to the EPA 6020A method by means of a Perkin-Elmer ELAN-DRC ICP-mass spectrometer.

The physico-mechanical properties of the artificial cement-based granular materials, prepared both with and without additives were measured according to the standard methods commonly used for concrete aggregates. Specific gravity and water absorption were measured according to the EN 1097-6 method. Resistance to fragmentation was measured with two different methods: aggregate crushing value (ACV), according to BS 812-110 and Los Angeles test, according to EN 1097-2. Freeze-thaw resistance was measured according to the EN 1367-1 norm while alkali-silica reactivity was evaluated following the UNI 8520-22 method.

The thermogravimetric technique was used to evaluate the presence and the amount of portlandite originated from the hydration of cement in the artificial aggregate produced with the presented method. Analyses were performed by means of a Netzsch STA 409 thermo gravimetric analysis/differential scanning calorimeter (TGA/DSC) on 40-50 mg of sample after 48 h of hydration, with an heating ramp rate of 40 °C/min (from 20 to 1100 °C) in static air.

7.4 Results

7.4.1 X-μCT

The stacking of all the reconstructed X-μCT slices allowed the internal structure of the investigated samples to be visualized in 3D, as shown in Fig. 7.5.

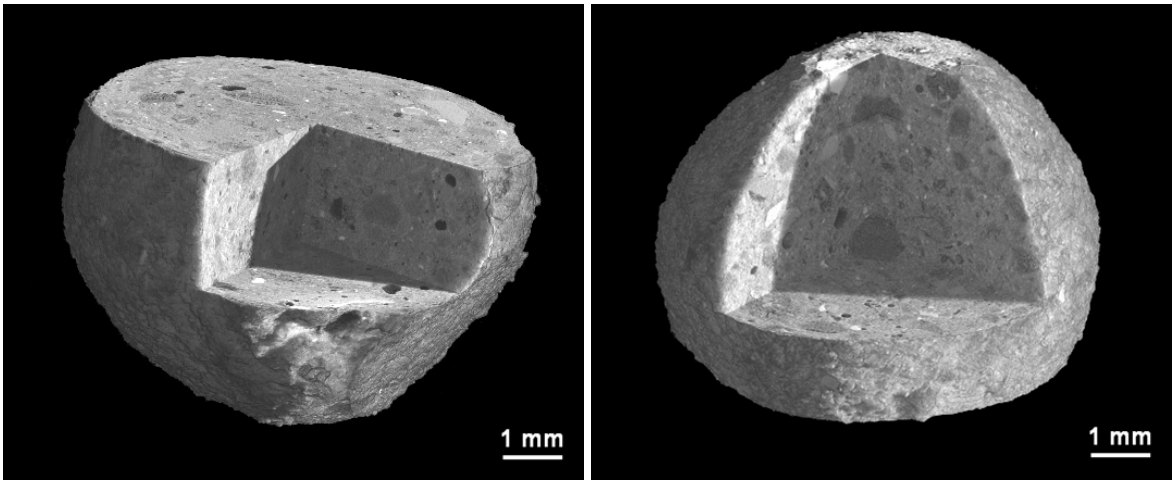

Figure 7.5 - 3D reconstructions of two cement-based S/S grains prepared according to the HPSS method. A portion of each dataset has been digitally removed in order to visualize the interior of the samples. Darker grey values correspond to low attenuation (air voids) and brighter ones to high-absorbing particles (metals, lead-containing glass).

Several distinct features were clearly recognized in the reconstructed images as for example entrained air bubbles, heterogeneous mineral grains, glass fragments, vegetal remains, mollusc shells and several very highly absorbing particles of probable metallic nature. All these elements were of course contained in the original contaminated soil, some of them naturally included, others introduced by the glass production activity formerly operating in the "ex-Conterie" site. The mentioned presence of dense, highly attenuating particles was a problematic issue during the image analysis procedure. In fact, if these particles are large enough to cause the incoming X-ray beam to be completely stopped, severe artefacts can be introduced into the reconstructed slices. These are generally seen as black shadows and streaks around the high-absorbing particles, creating a region characterized by a total lack of information that may be mistakenly considered as a void. This problem could be partially overcome by increasing the energy of the beam but this would of course cause a loss of contrast in all the other portions of the image. Therefore, in some cases, a manual correction was necessary to correct such artefacts, in order to avoid an overestimation of the entrained air content.

Fig. 7.6 shows a comparison between two reconstructed slices obtained from two S/S grains prepared without and with superplasticizer.

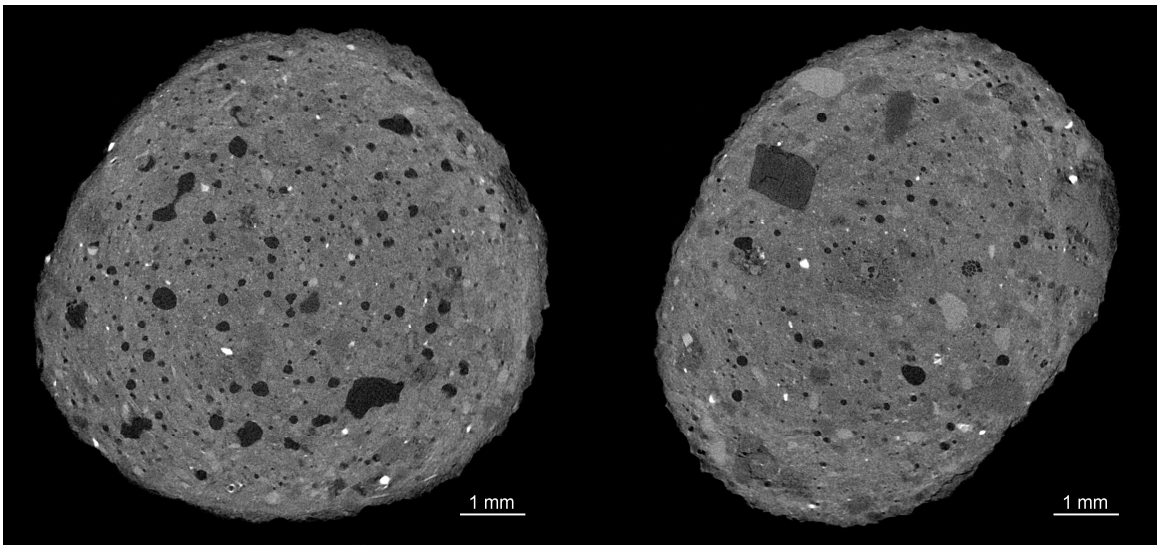

Figure 7.6 - Cross-sectional reconstructed slices illustrating two S/S grains prepared without (left) and with (right) additives. A more compact matrix, with a significantly lower air void content can be achieved following the S/S procedure presented here.

By looking at the two images, a significant difference in total air void content as well as in void shape and size can be clearly recognized. The total entrained air content, calculated

(over the entire 3D volume) after the segmentation of the pore fraction by simply dividing the number of black voxels by the total number of voxels (solids and voids) is 5.17 % for the conventional S/S grain (Sample A) and 1.97 % for the sample prepared using superplasticizers (Sample B). It should be pointed out that the size of a considerable amount of pores in cement-based materials is well below the resolution level of the technique (voxel size ~ 6 μm in this specific case), thus making their discrimination from the solid matrix practically impossible. Hence, our investigation was limited to larger, isolated (at least at this spatial resolution) air voids with a diameter greater than 10 μm. It should also be noted that some low-attenuating organic particles may show very low gray values in the reconstructed images, so they can be hardly discriminated from pores just by thresholding the GV histogram. The volume of each individual pore was calculated using the *Object Counter 3D* plugin of the *ImageJ* software and their size was then approximated according to the equivalent sphere diameter (i.e. the diameter of the sphere having the same volume as that pore). Significant differences were found between the two series of samples as illustrated by the histograms of pore size distribution of Fig. 7.7.

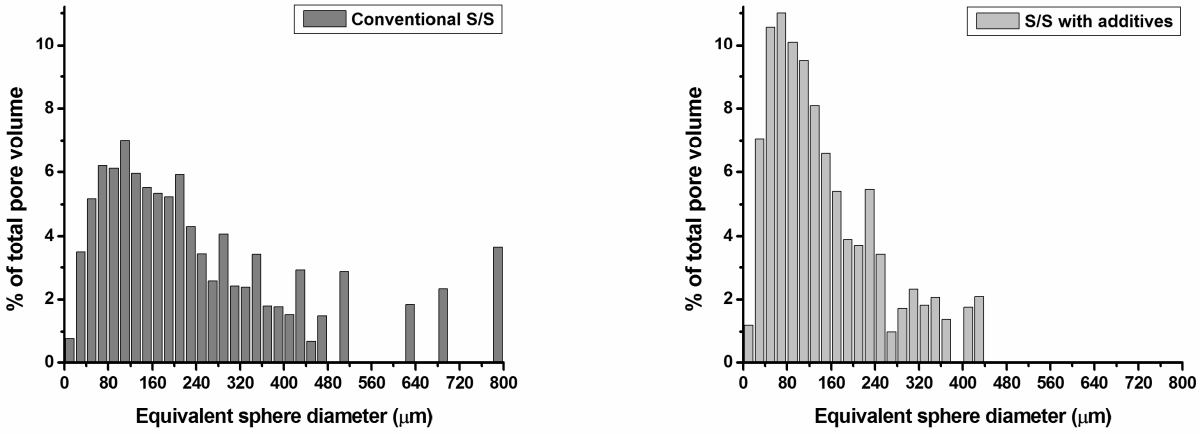

Figure 7.7 - Pore size distribution histograms calculated from the analysis of tomographic data for two S/S grains formulated without (left) and with (right) superplasticizers. The relative fraction of the total pore volume was plotted versus the equivalent sphere diameter. The bin width is 20 μm. Due to limitations in the spatial resolution of the technique, pores smaller than 10 μm were not detectable, so they were not included in the calculations.

Even without taking into account the few very large (> 500 μm) air voids, the pores contained in the conventional S/S grain result to be distributed over a broader range of sizes if compared to the sample prepared using additives. Moving from the conventional

sample to that produced with the superplasticizer, the relative amount of pores whose equivalent diameter is smaller than 100 μm increases from 21.7 % to 39.9 %. Moreover, in the first case, the maximum peak of the distribution corresponds to the 100-120 μm class while in the second one the dominant interval is 60-80 μm. The comparison of the reconstructed slices of Fig. 7.6 and the results of Fig. 7.7 clearly confirm that the use of a superplasticizer in the wet S/S granulation process of the "Ex-Conterie" contaminated soil significantly reduced the entrained air content (pore sizes from 10 μm to 400 μm) of the final product. This is a direct effect of the reduction in the viscosity of the soil-water-cement fresh mix, induced by superplasticizers.

7.4.2 Mercury intrusion porosimetry

A comparison between two porosimetric curves obtained for the samples prepared without (dashed line) and with superplasticizer (solid line) is reported in Fig. 7.8.

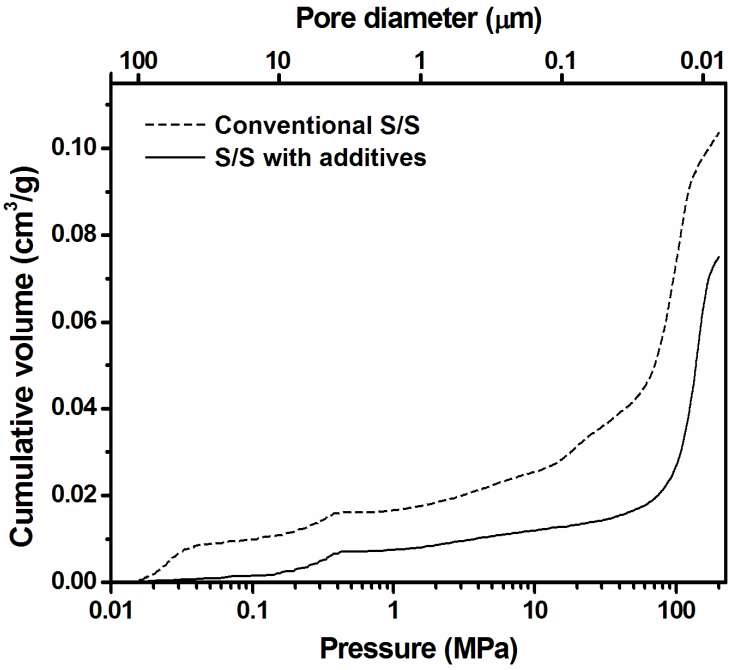

Figure 7.8 - Porosimetry curves obtained for S/S grains prepared with (solid line) and without (dashed line) superplasticizer. The cumulative volume of mercury intruded per gram of sample was plotted versus the applied pressure.

As a first result, it can be easily seen that the curve referring to the samples with the superplasticizer lies below the curve measured for the conventional S/S grains, clearly indicating a reduced total connected porosity. In particular, the measured total void content decreases from 20.07 % to 15.34 % of the entire sample volume. In this graph, the

minimum and maximum data points of the curves roughly correspond to intruded pores with diameters of 100 μm and 6 nm respectively. A slight change in the slope of the two curves at 0.4 MPa of intruding pressure is indeed an artefact due to the non-perfectly smoothed connection between the data points measured with the first and the second porosimeter. The use of superplasticizers seems to be effective in reducing porosity both at the larger and the thinner pore level. During the very early stages of intrusion (up to 0.04 MPa) a significantly larger volume of mercury is intruded in the conventional S/S sample if compared to the additivated one, as confirmed by the different slopes of the two curves. This indicates that the coarser pore fraction, ranging approximately from 100 to 40 μm (as calculated from pressure values), is far more represented in the first sample. From that point, the two datasets assume a nearly parallel trend until 5-6 MPa (roughly corresponding to a pore diameter of 0.4 μm), where the upper curve starts increasing again its slope. A remarkable change in the lower curve is seen only at very high pressure values thus indicating that the great majority of porosity is concentrated in the dimensional interval below 15-20 nm. This evidences seem to confirm that a lower w/c ratio and the use of superplasticizers substantially contribute to the reduction of micrometer and sub-micrometer scale porosity, creating a more dense matrix. According to many authors, pores larger than 50 to 100 nm may be detrimental to strength and permeability of cement paste (Mehta 1986, Goto and Roy 1981). Therefore, the observed decrease of the porosity in the sub-micrometer scale of the granular material produced with the superplasticizer are expected to produce an improvement of the environmental and mechanical properties of the artificial aggregates.

For what concerns the differences between the two samples in the low-pressure (high diameter) part of the graph, a major role may be played by the region commonly referred to as the interfacial transition zone (ITZ). In concretes and mortars ITZ is a thin, heterogeneous region of paste existing between the cementitious matrix and the surface of the aggregate particles, characterized by increased porosity and concentration of portlandite crystals if compared to the matrix paste (see for example Bonen 1994, Scrivener and Nemati 1996, Shane et al. 2000). In our specific case, the aggregates are represented by the grains included in the contaminated soil that was used for the preparation of the S/S products. Though there is no complete agreement about the mechanisms of formation, ITZs are likely to form as a result of an inefficient packing of cement grains at the aggregate surface (Ollivier et al. 1995). The relevant amount of

coarser porosity (left part of the graph) detected in conventional S/S samples is probably related to the presence of a percolating network of pores originating from contiguous ITZs around the aggregate grains. Superplasticizers, coupled with a lower w/c ratio of the mix, are thought to inhibit the growth of ITZs, thus hampering the formation of a preferential pathway for the percolation of fluids. This is demonstrated by the very low amount of mercury intrudable during the initial, low-pressure stages for the additivated samples.

For the interpretation of pore size distributions in the region of the micropores (right part of the graph), extreme care has to be taken when dealing with cement-based samples. In fact, in this kind of materials, the pore system usually does not satisfy the requirements of the classical model, thus giving rise to problematic artefacts in the output data. For example, as shown by electron microscope investigations, the shape of the pores in an hydrated cement paste is far more complex than the ideal network of cylindrical tubes of the classical Washburn's model. Anyway, this can be considered a minor problem, affecting to different extents also many other materials. A major issue is related to the fact that the great majority of the pores are not directly linked to the outer surface and can be reached by mercury only after it has travelled through a long and complex series of intermediate pores of different sizes and shapes (Diamond 2000). A critical role is played by the presence inside cement pastes, mortars and concretes of a significant fraction of relatively large entrained air voids, as shown also by means of X-μCT. It is widely accepted that these air bubbles are not isolated but are part of the percolating pore system. In practice, a large air void inside the matrix cannot be reached by mercury until a certain threshold pressure value is reached, necessary to fill the smaller channels that lead to the said void. At that point, the large pore starts to act as a reservoir for mercury and the corresponding intruded volume is mistakenly referred to the threshold pressure and hence attributed to a much finer pore fraction which will then result overestimated. This phenomenon is commonly referred to as the "ink-bottle effect". Due to these intrinsic limitations related to the microstructure of cement-based materials, some authors (e.g. Diamond 2000) suggested that MIP should not be considered a completely reliable method for the determination of the pore size distribution and other associated parameters. However, this technique still remains an invaluable tool for the determination of the total intrudable volume enabling to detect pores having sizes several orders of magnitude smaller than those measurable with other techniques, as for example X-μCT.

7.4.3 Leaching tests, physico-mechanical tests and thermal analyses

The concentration of heavy metals in the eluates of the "Ex-Conterie" soil exceeded the regulatory standard of the Italian Government for the reusable materials (Decree of Ministry of the Environment n. 186/2006) for As, Cr, Cu and Pb, as shown in Tab. 7.3. The eluates of the pellets produced without the superplasticizer (sample A) complied with the standards for all the metals except for copper; this metal, most at the high values of pH typical of Portland cement mixtures, forms complexes with soil soluble organic matter and therefore increases its solubility (Xue and Sigg, 1999). On the other side, sample B, produced according to the HPSS formulation (with SP), complied with the regulatory limits for all the contaminants. These results confirm the importance of using superplasticizers in S/S processes, in order to improve the environmental compatibility of the solidified products. The results of physical and mechanical tests performed on the granular materials without and with the superplasticizer (Sample A and B, respectively) are shown in Tab. 7.4

Element	**Unit**	**Concentration**			
		Soil	**S/S without SP**	**HPSS with SP**	**Reg. limits**
As	µg/L	1254	7	<1	50
Cd	µg/L	3.9	<0.1	<0.1	5
Cr	µg/L	64	<1	<1	50
Cu	µg/L	175	100	20	50
Hg	µg/L	<0.1	<0.1	<0.1	1
Pb	µg/L	218	25	10	50

Table 7.3 - Results of leaching tests carried out according to the EN 12457-2 norm on the "ex-Conterie" untreated soil and the pellets produced with and without SP. The Italian regulatory limits for residential use are also reported. The eluates were then analyzed by means of ICP-MS, according to the EPA 6020A method.

Test	**Reference norm**	**Unit**	**S/S without SP**	**HPSS with SP**
Specific gravity	EN 1097-6	-	2.17	2.33
Water absorption	EN 1097-6	%	6.6	2.5
Aggregate crushing value	BS 812-110	%	29	24
Los Angeles (abrasion)	EN 1097-2	%	42	35
Freeze/Thaw	EN 1367-1	%	5.5	3.2
Alkali-silica reactivity	ASTM C1260	-	negative	negative

Table 7.4 - Results of some physico-mechanical tests commonly used for concrete aggregates, carried out on S/S grains prepared with and without superplasticizers.

A general improvement of all the investigated physico-mechanical properties can be observed for S/S granular materials prepared including SPs in their formulation. This is a direct effect of the lower water to solid ratio achievable when using such additives. Due to the lower amount of mixing water, a more compact matrix, characterized by higher strength and reduced porosity, can be obtained (Fig. 7.9). As a result, also the resistance to aggressive fluids from the environment and to freeze/thaw cycles is improved, with positive effects on the durability of the S/S products.

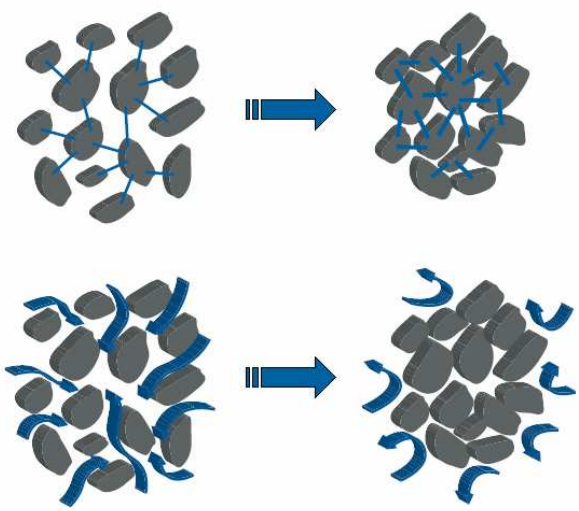

Figure 7.9 - Effect of the reduction of w/c on the microstructure of cement-based S/S products. Due to the closest packing of cement particles and to the reduced porosity, higher mechanical strengths and improved resistance to aggressive agents can be achieved, with beneficial effects on durability.

The results of thermal analyses carried out on a set of grains from sample B (with additives) are reported in Fig. 7.10. Such analyses were performed in order to verify the occurrence of pozzolanic reactions (eq. 7.1) between the highly soluble portlandite and some of the soil components. This is commonly done by monitoring the reaction of decomposition of portlandite at ~500 °C:

$$Ca(OH)_2 \rightarrow CaO + H_2O \uparrow \quad (7.3)$$

The absence of a significant loss of weight at ~500 °C seems to indicate that a considerable amount of Ca-hydroxide produced by cement hydration reacts during the first two days of hydration with some pozzolanic materials included in the original soil, most likely clay minerals, forming more stable calcium silicate hydrates (C-S-H).

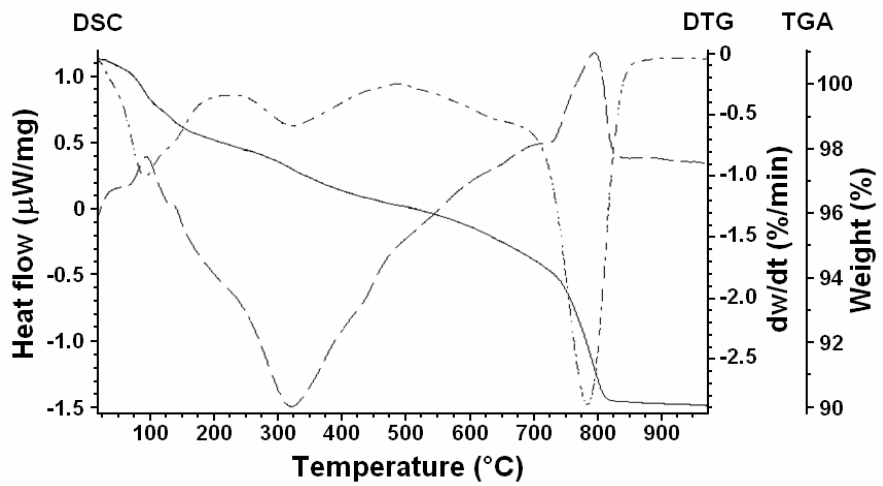

Figure 7.10 - Thermogravimetric analysis (TGA, solid line), differential thermal gravimetry (DTG, dash-dotted line) and differential scanning calorimetry (DSC, dashed line) curves of granular cementitious materials produced following the HPSS process (after 48 h of hydration). No significant loss of weight is detectable at ~ 500 °C, the dissociation temperature of portlandite.

8- Conclusions

The results obtained in this PhD thesis clearly demonstrate the suitability of X-ray computed micro-tomography (X-μCT) as a non invasive technique for the three dimensional (3D) investigation of cement-based materials. In particular, synchrotron based X-μCT is at present the only non-destructive imaging technique capable of sub-micrometric resolution, thus representing a fundamental tool for the *in-situ* study of the reactions taking place during the hydration of cements. It was demonstrated here that synchrotron X-μCT allows small microstructural variations to be monitored with a sufficiently high temporal resolution. This is of crucial importance, especially in the study of the early hydration stages that are known to be the most critical. The development of hydration products at the expenses of anhydrous clinker grains and pores was demonstrated by means of comparisons between cross-sectional slices, 3D reconstructed volumes and grey values histograms extracted from datasets acquired at different hydration ages. The amount of pores and unreacted clinker as a function of hydration time were successfully quantified. Moreover, this technique allowed to obtain a direct visualization of the microstructural changes induced in cements by different water-cement ratios and by the addition of superplasticizers. At present, the main drawback of X-μCT is related to its lower spatial resolution if compared to SEM imaging. Moreover, due to the similar values of the attenuation coefficient between different cement phases, their discrimination may represent a very complicated task. However, the total non-invasiveness and the access to the third dimension provided by X-μCT definitely represent two major advantages. Further technological developments, especially for what concerns the detectors, are expected to lead in the future to an improvement of the achievable spatial resolution as the theoretical limits have not been reached yet. It was also shown that, due to their intrinsic microstructural complexity, cement-based materials represent an ideal case for the visualization of edge-enhancement effects caused by phase contrast, as they are characterized by a large amount of crystal-air interfaces and high surface-volume ratios. However it was also demonstrated that the effects of phase contrast may lead to erroneous interpretations of the grey values distribution in the reconstructed images. A method based on phase retrieval has been successfully tested in order to overcome this limitation.

The capabilities of conventional laboratory X-μCT were also investigated. Though being characterized, due to intrinsic technical reasons, by a lower spatial and temporal resolution

and by a general higher occurrence of image artefacts, this technique allowed to obtain satisfactory results from the analysis of cementitious samples. Even though the resolution of microfocus X-μCT limits its use to the investigation of larger scale features (e.g. macropores) important qualitative information can still be achieved. It was shown that the effects of different water-cement ratios on the microstructure of cement pastes (e.g. compactness of the paste or drying shrinkage) can be easily visualized. This results can be directly correlated with the mechanical properties measured in macroscopic samples.

The capabilities of a novel technique called diffraction tomography (XRD-CT) were also tested for the first time on cement materials. The results of XRD-CT test measurements indicate that this technique can be successfully applied to the non-destructive investigation of cement materials. The main advantage of XRD-CT is the access to the real distribution of selected crystalline or amorphous phases. This method allowed to map the ettringite distribution in mortar and cement samples and its evolution with hydration. In addition, also the poorly crystalline C-S-H phase was successfully mapped. The main problems encountered concerned artefacts in tomographic reconstruction for phases with crystal sizes comparable or larger than the dimension of the incident beam. Other drawbacks are related to the limited spatial resolution (4-5 μm in the present study) if compared to X-μCT and especially to the long acquisition time for a complete XRD-CT scan. At present, the long duration of the scan does not match the time resolution required for studying the cement paste evolution during the early stages of hydration. This limitation can partially be overcome by reducing the size of the measured volume, thus reducing the total acquisition time. As a general conclusion, it can be said that the limits of applicability of the technique concern the dimensions of the crystalline objects that can be mapped in relation to the desirable spatial resolution. The main constraint is to investigate crystals which are one order of magnitude smaller than the incident X-ray beam size. By increasing the probe dimensions, crystalline materials with larger crystals can be mapped but of course at the expense of spatial resolution. Despite the present limitations, XRD-CT represents a powerful and very promising method for the mapping of the distribution of phases, irrespective on their crystalline nature, with a totally non-invasive approach. Its combination with X-μCT (but also XRF-CT) will surely represent a new multimodal approach to the understanding of the physical and chemical processes occurring in cements.

In the last part of the work, microfocus X-μCT was successfully applied (in combination with other established experimental methods) to the performance evaluation of an

innovative method for the remediation of contaminated sites. Microfocus X-μCT was employed to characterize cementitious granular materials produced from the solidification/stabilization (S/S) of contaminated soils. The pore size distributions of samples prepared with different formulations (with and without superplasticizers) were successfully investigated. The results obtained indicated that PCE-based superplasticizers (SPs) play a fundamental role in the achievement of improved properties also for materials produced with S/S methods. As a result of the reduced amount of mixing water required when SPs are included in the formulation, all the physico-mechanical properties (e.g. permeability, strength) of the final S/S products are significantly improved, with beneficial effects on their durability and environmental compatibility.

Acknowledgements

This PhD project was funded by Mapei S.p.A. in the frame of its research agreement with the Department of Geosciences of the University of Padua. Mapei S.p.A. is acknowledged also for providing materials and facilities for many experiments during these three years. The synchrotron experimental sessions were supported by the European Synchrotron Radiation Facility (Exp. MA-648 and CH-3087).

Among the various people who helped me during my PhD, I would like to thank the entire staff of the SyRMeP beamline at Elettra for introducing me into the world of X-ray micro-tomography and for their help and useful comments during the experiments at Tomolab. I am also grateful to Alexander Rack and Remi Tucoulou of the ID22 beamline at ESRF for their technical support during experimental sessions at the synchrotron and their fundamental tips concerning X-μCT and XRD-CT data analysis. Finally I would like to thank my supervisor, Prof. Gilberto Artioli and Mariachiara Dalconi for sharing their scientific enthusiasm with me during my PhD and for their useful review of this thesis.

References

Abramoff, M.D., Magelhaes, P.J. & Ram, S.J. (2004) *Image processing with ImageJ*, Biophotonics International, 11(7), 36-42.

Baruchel, J., Cloetens, P., Härtwig, J. & Schlenker, M. (2003) *X-ray imaging with hard synchrotron radiation*. In: Mobilio, S. & Vlaic, G. (Eds.), Conference proceedings vol. 82, Synchrotron radiation: fundamentals, methodologies and applications, Società Italiana di Fisica, Bologna (Italy), 743-770.

Beckmann, F., Bonse, U., Busch, F., Günnewig, O. & Biermann, T. (1995) *A novel system for X-ray phase-contrast microtomography*. HASYLAB Annual Report II, 691-692.

Bentz, D.P., Quenard, D.A., Kunzel, H.M., Baruchel, J., Peyrin, F., Martys, N.S. & Garboczi, E.J. (2000) *Microstructure and transport properties of porous building materials. II: Three-dimensional X-ray tomographic studies.* Materials and Structures, 33(3), 147-153.

Bentz, D.P., Mizell, S., Satterfield, S., Devaney, J., George, W., Ketcham, P., Graham, J., Porterfield, J., Quenard, D., Vallee, F., Sallee, H., Boller, E. and Baruchel, J. (2002) *The visible cement data set*, Journal of Research of the National Institute of Standards and Technology, 107, 137-148.

Bleuet, P., Welcomme, E., Dooryhée, E., Susini, J., Hodeau, J.-L. & Walter, P. (2008) *Probing the structure of heterogeneous diluted materials by diffraction tomography*, Nature Materials, 7, 468-472.

Boin, M. & Haibel, A. (2006) *Compensation of ring artefacts in synchrotron tomographic images*. Optics Express, 14, 12071-12075.

Bonen, D. (1994) *Calcium hydroxide deposition in the near interfacial zone in plain concrete*, Journal of the American Ceramic Society, 77, 193-196.

Bonse, U., Nusshardt, R., Busch, F., Pahl, R., Johnson, Q., Kinney, J., Saroyan, R., & Nichols, M. (1989) *Optimization of CCD-based energy modulated X-ray microtomography*. Review of Scientific Instruments, 60, 2478-2481.

Brun, F., Kourousias, G., Dreossi, D. and Mancini, L. (2009) *An improved method for ring artifacts removing in reconstructed tomographic images*, World Congress on Medical Physics and Biomedical Engineering, IFMBE Proceedings, Munich (Germany), 25, 926-929.

Bullard, J.W., Jennings, H.M., Livingston, R.A., Nonat, A., Scherer, G.W., Schweitzer, J.S., Scrivener, K.L. & Thomas, J.J. (2010) *Mechanisms of cement hydration*. Cement and Concrete Research, doi: 10.1016/j.cemconres.2010.09.011.

Cloetens, P., Salomé, M., Buffière, J.Y., Peix, G., Baruchel, J., Peyrin, F. & Schlenker, M. (1997) *Observation of microstructure and damage in materials by phase sensitive radiography and tomography*. Journal of Applied Physics, 81, 5878-5886.

Cloetens, P., Ludwig, W., Baruchel, J., Guigay, J.-P., Rejmankova-Pernot, P., Salomé-Pateyron, M., Schlenker, M., Buffière, J.Y., Maire, E. & Peix, G. (1999) *Hard X-ray phase imaging using simple propagation of a coherent synchrotron radiation beam*. Journal of Physics D: Applied Physics, 32, A145-A151.

Cloetens, P., Ludwig, W., Guigay, J.-P., Baruchel, J., Schlenker, M. & Van Dyck, D. (2000) *Phase contrast tomography*. In: Baruchel, J. et al. (Eds.), X-ray tomography in material science, Hermes Science Publications, Paris (France), 29-44.

Collepardi, M. (2006) *The New Concrete*, ENCO, Ponzano Veneto (Italy).

Cullinane, M.J., Jones, L.W. & Malone, P.G. (1986) *Handbook for stabilization/solidification of hazardous waste*. EPA/540/2-86-001, U.S. Environmental Protection Agency, Cincinnati (OH, USA).

Daimon, M. & Roy, D.M. (1978) *Rheological properties of cement mixes: I. Methods, preliminary experiments, and adsorption studies*. Cement and Concrete Research, 8(6), 753-764.

Davis, R. & Elliott, J.C. (1997) *X-ray microtomography scanner using time-delay integration for elimination of ring artefacts in the reconstructed image*. Nuclear Instruments and Methods in Physics Research A, 394, 157-162.

De Nolf, W. (2006) *XRDUA, 2D powder-XRD analysis*. http://xrdua.ua.ac.be

Diamond, S. (2000) *Mercury porosimetry: an inappropriate method for the measurement of pore size distributions in cement-based materials*, Cement and Concrete Research, 30, 1517-1525.

Feldkamp, L.A., Davis, L.C. & Kress, J.W. (1984) *Practical cone-beam algorithm*, Journal of the Optical Society of America, A1(6), 612-619.

Förster, E., Goetz, K. & Zaumseil, P. (1980) *Double crystal diffractometry for the characterization of targets for laser fusion experiments*. Kristall und Technik, 1, 937-945.

Gallucci, E., Scrivener, K., Groso, A., Stampanoni, M. & Margaritondo, G. (2007) *3D experimental investigation of the microstructure of cement pastes using synchrotron X-ray microtomography (μCT)*. Cement and Concrete Research, 37, 360-368.

Gartner, E.M., Young, J.F., Damidot, D.A. & Jawed, I. (2002) *Hydration of Portland cement*. In: Bensted, J. & Barnes, P. (Eds.), Structure and performance of cements, Spon Press, New York (NY, USA).

Glasser, F.P. (1994) *Environmental uses of cement in waste conditioning*. In: Grutzeck, M.D. & Sarkar, S.L. (Eds.), Engineering Foundation Conference Proceedings, Advances in Cement and Concrete, American Society of Civil Engineers, New York (NY, USA), 499-507.

Goto, S. & Roy, D. (1981) *Diffusion of ions through hardened cement pastes*. Cement and Concrete Research, 11, 751-757.

Haibel, A. (2008) *Synchrotron X-ray absorption tomography*. In: Banhart, J. (Ed.), Advanced tomographic methods in materials research and engineering, Oxford University Press, New York, (NY, USA), 141-160.

Helfen, L., Dehn, F., Mikulìk, P. & Baumbach, T. (2005) *Three-dimensional imaging of cement microstructure evolution during hydration*. Advances in Cement Research, 17(3), 103-111.

Hewlett, P.C. (Ed.) (2007) *Lea's chemistry of cement and concrete (fourth edition)*, Elsevier, Amsterdam (Netherlands).

Hounsfield, G.N. (1973) *Computerized transverse axial scanning (tomography)*. British Journal of Radiology, 46, 1016-1022.

Kak, A.C. & Slaney, M. (1988) *Principles of computerized tomographic imaging*, IEEE Press, New York, (NY, USA).

Kantro, D.L. (1980) *Influence of water-reducing admixtures on properties of cement paste: a miniature slump test*. Cement, Concrete and Aggregates, 2, 95-102.

Klemm, W.A. (1998). *Ettringite and oxyanion-substituted ettringites. Their characterization and applications in the fixation of heavy metals: a synthesis of the literature*, Research and development bulletin RD116W, Portland Cement Association, Skokie (IL, USA).

Kuba, A. & Herman, G.T. (2008) *Some mathematical concepts for tomographic reconstruction*. In: Banhart, J. (Ed.), Advanced tomographic methods in materials research and engineering, Oxford University Press, New York, (NY, USA), 19-36.

Labiche, J.C., Mathon, O., Pascarelli, S., Newton, M.A., Guilera Ferre, G., Curfs, C., Vaughan, G., Homs, A. & Fernandez Carreiras, D. (2007) *The fast readout low noise camera as a versatile x-ray detector for time resolved dispersive extended x-ray absorption fine structure and diffraction studies of dynamic problems in materials science, chemistry, and catalysis*. Review of Scientific Instruments, 78, 091301.

Matsuyama, H. & Young, J.F. (1999) *Intercalation of polymers in calcium silicate hydrate: a new synthetic approach to biocomposites?* Chemistry of Materials, 11, 16-19.

Mehta, P.K. (1986) *Concrete: its structure, properties and materials*, Prentice-Hall, Englewood Cliffs, (NJ, USA).

Mirone, A., Wilcke, R., Hammersley, A. & Ferrero, C. (2009) *PyHST (High Speed Tomographic Reconstruction)*, http://www.esrf.eu/UsersAndScience/Experiments/ TBS/SciSoft/.

Momose, A. (1995) *Demonstration of phase-contrast X-ray computed tomography using an X-ray interferometer*. Nuclear Instruments and Methods in Physics Research – A, 352, 622-628.

Natterer, F. (1986) *The mathematics of computerized tomography*. Teubner, Stuttgart (Germany).

Ollivier, J.P., Maso, J.C. & Bourdette, B. (1995) *Interfacial transition zone in concrete*. Advanced Cement Based Materials, 2(1), 30-38.

Paganin, D., Mayo, S.C., Gureyev, T.E., Miller, P.R. & Wilkins, S.W. (2002) *Simultaneous phase and amplitude extraction from a single defocused image of a homogeneous object*, Journal of Microscopy, 206, 33–40.

Parisatto, M., Artioli, G., Ferrari, G., Gerarduzzi, M. & Mazzoli, C. (2011) *Characterization of artificial aggregates produced from contaminated soils*. Submitted for the proceedings of the XIII International Congress on the Chemistry of Cement, Madrid (Spain).

Peele, A.G. & Nugent, K.A. (2008) *Phase-contrast and holographic tomography*. In: Banhart, J. (Ed.), Advanced tomographic methods in materials research and engineering, Oxford University Press, New York, (NY, USA), 161-180.

Plank, J., Keller, H., Andres, P.R. & Dai, Z.M. (2006) *Novel organo-mineral phases obtained by intercalation of maleic anhydride-allyl ether copolymers into layered calcium aluminum hydrates*. Inorganica Chimica Acta, 359(15), 4901-4908.

Plank, J., Pöllmann, K., Zouaoui, N., Andres, P.R. & Schaefer, C. (2008) *Synthesis and performance of methacrylic ester-based polycarboxylate superplasticizers possessing hydroxy-terminated poly(ethylene glycol) side chains*. Cement and Concrete Research, 38, 1210-1216.

Promentilla, M.A.B., Sugiyama, T., Hitomi, T. & Takeda, N. (2009) *Quantification of tortuosity in hardened cement pastes using synchrotron-based X-ray computed microtomography*. Cement and Concrete Research, 39(6), 548-557.

Radon, J. (1917) *Über die Bestimmung von Funktionen durch ihre Integralwerte längs gewisser Mannigfaltigkeiten.* Berichte über die Verhandlungen der Königlichen Sächsischen Akademie der Wissenschaften, 69, 262-277.

Raven, C., Snigirev, A., Snigireva, I., Spanne, P., Souvorov, A., & Kohn, V. (1996) *Phase-contrast microtomography with coherent high-energy synchrotron X-rays*. Applied Physics Letters, 69, 1826-1828.

Raven, C. (1998) *Numerical removal of ring artifacts in microtomography*. Review of Scientific Instruments, 69, 2978-2980.

Renaudin, G., Russias, J., Leroux, F., Frizon, F. & Cau-dit-Coumes, C. (2009) *Structural characterization of C-S-H and C-A-S-H samples-Part I: long-range order investigated by Rietveld analyses*. Journal of Solid State Chemistry, 182, 3312-3319.

Richardson, I.G. (2008) *The calcium silicate hydrates*. Cement and Concrete Research, 38(2), 137-158.

Scrivener, K.L. & Nemati, K.M. (1996) *The percolation of pore space in the cement paste/aggregate interfacial zone of concrete*, Cement and Concrete Research, 26(1), 35-40.

Shane, J.D., Mason, T.O., Jennings, H.M., Garboczi, E.J. & Bentz, D.P. (2000) *Effects of the interfacial transition zone on the conductivity of Portland cement mortars*. Journal of the American Ceramic Society, 83, 1137-1144.

Shepp, L.A. & Vardi, Y. (1982) *Maximum likelihood reconstruction in positron emission tomography*. IEEE Transactions on Medical Imaging, 1(2), 113-122.

Sijbers, J. & Postnov, A. (2004) *Reduction of ring artifacts in high resolution micro-CT reconstructions*, Physics in Medicine and Biology, 49, N247-N253.

Simionovici, A., Chukalina, M., Drakopoulos, M., Snigireva, I., Snigirev, A., Schroer, C., Lengeler, B., Janssen, K. & Adams, F. (1999) *X-ray fluorescence microtomography: experiment and reconstruction*. In: Bonse, U. (Ed.), Developments in X-Ray Tomography II, Proceedings of SPIE, 3772, 304-310.

Snigirev, A., Snigireva, I., Kohn, V., Kuznetsov, S. & Schelokov, I. (1995) *On the possibilities of X-ray phase contrast microimaging by coherent high-energy synchrotron radiation*. Review of Scientific Instruments, 66, 5486-5492.

Somogyi, A., Tucoulou, R., Martinez-Criado, G., Homs, A., Cauzid, J., Bleuet, P., Bohic, S. & Simionovici, A. (2005) *ID22: a multitechnique hard X-ray microprobe beamline at the European Synchrotron Radiation Facility*, Journal of Synchrotron Radiation, 12(2), 208-215.

Taylor, H.F.W. (1990) *Cement chemistry*, Academic Press, London (UK).

Thurner, P., Müller, B., Sennhauser, U., Hubbell, J. & Müller, R. (2004) *Tomography studies of biological cells on polymer scaffolds*. Journal of Physics: Condensed Matter, 16, S3499-S3510.

U.S. EPA (2004) *Treatment technologies for site cleanup: annual status report* (11th edition). EPA-542-R-03-009.

Weitkamp, T., Haas, D., Wegrzynek & Rack, A. (2010) *ANKAphase: software for single-distance phase-retrieval from inline X-ray phase contrast radiographs*. Submitted to Journal of Synchrotron Radiation.

Wilkins, S.W., Gureyev, T.E., Gao, D., Pogany, A. & Stevenson, A.W. (1996) *Phase-contrast imaging using polychromatic hard X-rays*. Nature, 384, 335-338.

Xue, H. & Sigg, L. (1999) *Comparison of the complexation of Cu and Cd by humic or fulvic acids and by ligands observed in lake waters*. Aquatic Geochemistry, 5, 313-335.

Zingg, A. (2008) *Cement-superplasticizer interaction: link between macroscopic phenomena and microstructural data of the early cement hydration*. Ph.D thesis, diss. ETH No. 17645.

Zingg, A., Winnefeld, F., Holzer, L., Pakusch, J., Becker, S., Figi, R. & Gauckler, L. (2009) *Interaction of polycarboxylate-based superplasticizers with cements containing different C_3A amounts*. Cement and Concrete Composites, 31, 153-162.